Quantitative Measurement of the Cornea by OCT

Inaugural dissertation

to be awarded the degree of

Dr. sc. med.

presented at the Faculty of Medicine
of the University of Basel

by

Jörg Wagner
from Untersiggenthal AG

Basel, 2020

Approved by the Faculty of Medicine

On application of

Prof. Dr. Philippe C. Cattin

Prof. Dr. med. David Goldblum

Prof. Dr. Gábor Székely

Basel, June 22, 2020

Prof. Dr. Primo Schär
Dean of the Medical Faculty

Contents

Acknowledgments

First, I would like to express my gratitude to everyone that enabled this PhD project. Special thanks in this regard go to Prof. Dr. Philippe C. Cattin and Jörg Breitenstein. Further, I would like to thank everyone that guided me throughout my dissertation. I am especially grateful to Dr. Lucio Robledo, Dr. Simon Pezold and Prof. Dr. David Goldblum.

Last but not least, I would like to thank my work colleagues, friends and familiy for their company and support.

Summary

The cornea accounts for two thirds of the eye's refractive power. The accurate measurement of the corneal shape and refractive power is essential for diagnostics and the planning of surgeries. Keratometry and corneal topography are clinically established measures for the quantitative description of the corneal shape and refractive power. One major application is the planning of cataract surgeries, where the natural lens gets replaced by an intraocular lens (IOL). Typically, different measurement modalities are combined to acquire all measures needed for accurate IOL selection.

Optical coherence tomography (OCT) potentially enables the three-dimensional measurement of all optically relevant structures of the eye at once – including the cornea. However, the use of OCT for corneal topography and keratometry is still limited. One limitation is the sensitivity of beam-scanning to eye motion. This is especially true for beam-scanning OCT, that relies on the sequential gathering of one-dimensional depth profiles. This sensitivity can be decreased by reducing the measurement duration, in particular by increasing the scan speed. Nevertheless, there is a trade-off between axial resolution, scan range, scan speed, signal-to-noise ratio (SNR) and the cost of the system; higher speed implies lower SNR and higher axial resolution implies shorter scan range. To take full advantage of OCT – measuring the full depth of the eye at once – one has to make compromises regarding the resolution and speed of the system.

In our work, we present solutions for OCT-based keratometry and topography, using a system with limited axial resolution and speed which is, in return, able to measure the full depth of the eye. The limited axial resolution asks for more extensive measurements to compensate for the increased uncertainties. The need for more extensive measurements combined with the limited speed makes the OCT measurements more sensitive to motion and asks for new scanning and motion compensation techniques.

In this PhD thesis, new methods for scanning, segmentation, motion compensation and reconstruction are presented. We propose new scanning techniques with two-dimensional scan trajectories, enabling robust reconstruction and accurate motion compensation with high temporal resolution. The motion compensation features model-based motion compensation in three dimensions. Because current segmentation methods do not apply to these new scanning techniques, we present a novel method for model-based segmentation. Further, we present methods for robust reconstruction, topography and accurate simulated keratometry (SimK) from OCT measurements.

Zusammenfassung

Die Hornhaut ist verantwortlich für zwei Drittel der Brechkraft des Auges. Die exakte Bestimmung ihrer Form und Brechkraft ist entscheidend für die Diagnostik und die Planung von Operationen. Die Keratometrie und die Hornhauttopographie sind zwei klinisch etablierte Methoden zur Bestimmung der Form und Brechkraft der Hornhaut. Die Resultate werden werden beispielsweise verwedet in der Planung von Kataraktoperationen, in welchen die natürliche Linse durch eine Intraokularlinse (IOL) ersetzt wird. Typischerweise werden mehrere Messmodalitäten kombiniert zur Bestimmung aller relevanten Kenngrössen zur korrekten IOL-Selektion.

Die Optische Kohärenztomografie (englisch optical coherence tomography, OCT) ermöglicht potenziell die dreidimensionale Vermessung aller optisch relevanten Strukturen des Auges, inklusive der Hornhaut, mittels einer Messung. Trotzdem ist der Einsatz von OCT für die Hornhauttopographie und Keratometrie noch immer limitiert. Eine Limitierung ist die Anfälligkeit von OCT auf Augenbewegungen. Dies gilt insbesondere für die sequentielle OCT, bei welcher nacheinander eindimensionale Tiefenprofile erfasst werden. Die Anfälligkeit kann durch durch eine Reduktion der Messdauer, namentlich durch Erhöhung der Abtastgeschwindigkeit, vermindert werden. Es besteht jedoch eine Zielkonflikt zwischen Tiefenauflösung, Abtasttiefe, Abtastgeschwindigkeit, Signal-Rausch-Verhältnis und den Kosten des Systems; eine grössere Abtastgeschwindigkeit geht auf Kosten des Signal-Rausch-Verhältnisses und eine höhere Tiefenauflösung geht auf Kosten der Abtasttiefe. Um die vollen Vorteile der OCT auszunutzen, namentlich die Vermessung des Auges über seine gesamte Tiefe, müssen daher Kompromisse bezüglich der Tiefenauflösung und Geschwindigkeit eingegangen werden.

In unserer Arbeit präsentieren wir Lösungen für eine OCT basierte Keratometrie und Hornhauttopographie unter Verwendung eines Systems mit limitierter Tiefenauflösung und Geschwindigkeit, aber im Gegenzug die Vermessung des Auges in seiner gesamten Tiefe erlaubt. Die erhöhte Unsicherheit durch die limitierte Tiefenauflösung erfordert eine umfangreichere Messung. Die Erfordernis einer umfangreicheren Messung in Kombination mit der limitieren Geschwindigkeit macht die OCT Messung noch anfälliger auf Augenbewegung und erfordert neue Methoden zur Abtastung und Bewegungskompensation.

Unsere Lösungen beinhalten neue Methoden zur Abtastung, Segmentierung, Bewegungskompensation und Rekonstruktion. Die präsentierten Abtastmethoden verfügen über zweidimensionale Trajektorien und ermöglichen eine robuste Rekonstruktion und eine präzise Bewegungskompensation mit hoher zeitlicher Auflösung. Die Bewegungskompensation ermöglicht eine modellbasierte in drei Dimensionen. Weil sich derzeitige Segmentierungsmethoden nicht auf die neuen Abtastmethoden anwenden lassen, präsentieren wir eine neue Methode zur Segmentierung. Weiter präsentieren wir Methoden zur robusten Rekonstruktion, Hornhauttopographie und simulierter Keratometrie basierend auf OCT Messungen.

1 Introduction

The cornea alone accounts for two thirds of the eye's refractive power, and as such corneal deformations and diseases have a big impact on the patient's vision and quality of life. Ophthalmologists rely on the quantitative measurement of the corneal shape and refractive power for diagnostics and the planning of surgeries. One major application is the planning of cataract surgeries, where the natural lens gets replaced by an artificial intraocular lens (IOL). Cataract denotes the pathological clouding of the lens, leading to a decrease in vision that can result in blindness. Cataract is responsible for half of all cases of blindness worldwide. Ophthalmologists typically select the proper IOL based on keratometry, the assessment of the principal corneal refractive power and astigmatism, and one-dimensional measurements (A-values) including the eye length, anterior chamber depth and lens thickness. These parameters are typically acquired using a combination of different modalities. For example, the established biometer LENSTAR 900 (Haag-Streit AG, Köniz, Switzerland) combines camera-based keratometry with low coherence reflectometry to acquire all measures needed for IOL selection.

Another application relying on the quantitative measurement of the cornea is the detection of keratoconus at an early stage. Keratoconus denotes the pathological thinning and conical deformation of the cornea. Progressed keratoconus is associated with increased myopia (nearsightedness), astigmatism and loss of visual acuity due to surface irregularity which cannot be compensated with spectacles [1]. Keratoconus can be detected and monitored by corneal topography, the three-dimensional mapping of the cornea's shape and refractive power.

Optical coherence tomography (OCT) enables the acquisition of depth scans and cross-sectional images of the eye. This potentially enables the measurement of all relevant structures for IOL selection and detection of pathologies like keratoconus with a single modality. However, the use of OCT for keratometry and topography is still limited. To assess the central corneal shape by OCT, the cornea is scanned over its apical area. Sequential scanning takes time and makes the OCT measurement prone to eye movements. Possible solutions include the increase of scan speed or the use of a parallel or full field OCT instead of beam-scanning OCT. This thesis deals with the quantitative measurement of the cornea by beam-scanning OCT, using a system with limited axial resolution and speed, to enable OCT-based keratometry and topography.

1.1 Motivation

Usually, different measurement modalities are combined to acquire all relevant measures for diagnostics and surgery planning. Anterior corneal topography is commonly obtained by Placido ring reflection. Posterior corneal topography, for which Placido ring reflection is not applicable, is commonly obtained by Scheimpflug photography. Keratometry, the measurement of the corneal curvature, usually relies on the reflective nature of the cornea to assess the curvature based on curved mirror optics and imaging. The distances along the eye's visual axis (A-values), which are essential for the selection of the IOL in cataract surgery, can be determined by low coherence reflectometry or ultrasound.

OCT potentially allows the simultaneous, three-dimensional measurement of all relevant eye structures including the cornea. This enables the determination of all relevant measures from one measurement – namely keratometry, topography and the A-values. Due to the duration of the sequential scanning, beam-scanning OCT measurements take time and are susceptible to eye motion. The susceptibility to eye motion is a major limitation and has to be addressed to enable accurate topography and keratometry.

The axial scan range, scan rate and resolution are limited by the OCT system. Systems that enable the acquisition of the entire depth of the eye with reasonable resolution and scan rate are rare and rather expensive. Systems that enable the acquisition of the entire depth of the eye with high resolution and scan rate are still not commercially available. Available instruments either employ a low axial resolution or acquire data for the anterior segment and foveal region independently.

1.2 Contribution

In this PhD thesis, we present methods for the geometrically correct measurement of the cornea by OCT. The goal was to provide accurate corneal topography and keratometry using a system that enables the measurement of the eye over its full depth, accepting limitations regarding axial resolution, scan rate and scan speed.

To address these limitations, we present tailored methods for scanning, segmentation, motion compensation and reconstruction. For scanning, we propose a new spiral scan pattern that enables the removal of abrupt distortions from the measurement. For motion compensation, we introduce a method that relies on a continuous motion model to compensate for motion in three dimensions. The method is combined with yet another new scan pattern, optimised for motion compensation with high temporal resolution. Because current segmentation methods do not apply to two-dimensional scan patterns, we present a segmentation method with three-dimensional, model-based regularisation. For reconstruction, we introduce a regularised Zernike reconstruction for stable results in the curvature space, which is necessary for stable corneal topography. Furthermore, we present a method for OCT-based keratometry which accounts for the aspherical shape of the cornea.

1.3 Outline

In Chapter 2, we provide an introduction to optical coherence tomography and discuss the typical geometry of the eye, giving insight into corneal topography and keratometry. We further estimate the influence of limited axial resolution and scan accuracy on the determination of the corneal refractive power.

In chapters 3 to 5, we present our published or submitted methods for scanning, segmentation, motion compensation and reconstruction. In Chapter 3, we present our spiral scan pattern. In Chapter 4, we present our model-based segmentation method and Chapter 5 presents our motion compensation together with another two-dimensional scan pattern and the regularised Zernike reconstruction for corneal topography. In Chapter 6, we present our method for OCT-based keratometry, designed to be equivalent to reference keratometry. Lastly, in Chapter 7 we discuss the methods, taking into consideration the newest findings and adaptations of the methods and their limitations.

2 Background

In this chapter, we first provide an introduction to optical coherence tomography and discuss the typical geometry of the eye. Further, we give an insight into corneal topography and keratometry and discuss the variations in the shape of the human eye. We also discuss the expected eye motion and provide an estimation for the influence of limited axial resolution and scan accuracy on the determination of the corneal refractive power. Lastly, we discuss related work, including scientific publications, patents and existing commercial devices.

2.1 Optical Coherence Tomography

Since its beginning in 1991, optical coherence tomography (OCT) found its use in several clinical fields including ophthalmology [1]. OCT is a method for the investigation of optical scattering materials based on low coherence interferometry. OCT can be described as the electromagnetic analogue to sonography which measures echo time delay of sonic waves. Because the speed of electromagnetic waves is too high to measure echo time delays directly, OCT measures echo time delay indirectly by low coherence interferometry. Figure 2.1 shows an exemplary setup of a fibre-based interferometre, consisting of a light source, a reference arm and a sample arm. The light emitted by the source (LS) gets split by the fibre coupler (FB) into the reference arm and the measurement arm. In the reference arm, the light gets collimated by a lens (CL2) and reflected the same way back by the mirror (M3). In the measurement arm, it passes the scanner optics (after collimation by CL2) and gets reflected by the sample (S). The reflected light from both arms gets to the detector (D) via the fibre coupler (FB), where the two light waves superpose and form interferences. In low coherence interferometry, interferences only occur if the difference in optical distance between the

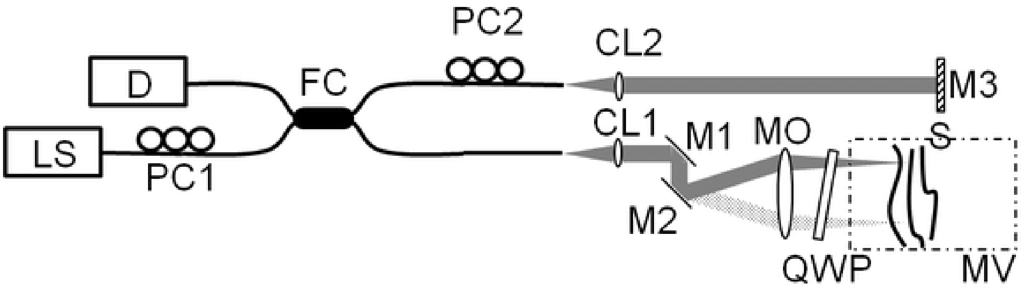

Figure 2.1. Exemplary fibre-based interferometer for SD-OCT. LS: Laser Source; PC1, PC2: Polarisation controller; FC: Fibre coupler; CL1, CL2: Collimating lens; M1, M2: Beam scanning mirrors; MO: Measurement objective; QWP: Quarter-wave plate; D: Detector; M3: Mirror; MV: Measurement volume; S: Sample.

measurement arm and the reference arm is in the range of the coherence length of the light source, which enables measuring the distance of scattering structures by changing the length of the reference arm. The optical distance is the product of the geometric length of the light path and the index of refraction of the medium through which it propagates. Therefore, parameters like the axial resolution or the measurement depth are often given "in air", indicating the optical distance, while the actual geometric distance depends on the sample medium.

One differentiates between time-domain OCT (TD-OCT) and spectral-domain OCT (SD-OCT). In time-domain OCT, depth profiles are acquired by changing the length of the reference arm with time. In spectral domain OCT, the length of the reference arm is fixed and the frequency spectrum of the interference is acquired instead, either by using a spectrometer as sensor (Fourier domain OCT or FD-OCT) or by changing the wavelength of a tunable laser source (swept-source OCT or SS-OCT). The spatial signal is then obtained by inverse Fourier-transformation on the interference spectrum. In general, SD-OCT has a better signal-to-noise-ratio than TD-OCT and therefore needs less light power for the same sensitivity [2]. This is a significant advantage in ophthalmology, where safety restrictions limit the maximal power on the eye. The higher sensitivity also enables performing OCT imaging at higher speed [3].

In traditional beam-scanning OCT, several one-dimensional scans (so-called axial scans or A-scans) are combined to obtain a two-dimensional image (B-scan) or a 3D volume (3D-OCT) by lateral shifting of the scan axis in one or two directions. Traditionally, a volume is generated by combining several parallel B-scans. The sequential gathering of A-scans is a limiting factor for acquisition speed and makes the measurement susceptible to movements. Typical A-scan rates range from 2000 Hz to MHz.

Other important parameters are the axial resolution, transversal resolution and the measurement depth. Whereas TD-OCT and FD-OCT both use broadband light sources, SS-OCT uses a laser source that is swept over a certain spectral range. The achievable axial resolution is limited by the spectral width of the light source, respectively the sweep range of the laser in SS-OCT. The transversal resolution is limited by the numerical aperture of the optics. In spectral-domain OCT, including swept-source OCT, the measurement depth is limited by the resolution of the spectral sampling [2]. In case of swept-source OCT, the spectral resolution and therefore the measurement depth is determined by the relation between the sampling rate and sweep rate.

In general, we want an OCT system with high resolution, high signal-to-noise ratio, high A-scan rate, high measurement depth and fast and accurate scanning. However, most of these demands cannot be fulfilled without a negative effect on one another. A higher A-scan rate is only possible at the expense of a lower signal-to-noise ratio. A high axial resolution conflicts with measurement depth. In swept-source OCT, the wavelength of the laser is swept over time. For a high A-scan rate, the sweep frequency has to be high. For a high spatial resolution, the sweep range has to be high as well. This is either possible by increasing the sweep speed or decreasing the sweep frequency. To achieve a wide spatial measurement range, the frequency spectrum has to be sampled with a high resolution – which is easier when the sweep speed is lower. The price of OCT systems and the amount of data to be processed within a patient examination increases with increased demands on A-scan rate, spatial resolution, signal-to-noise ratio and measurement depth.

2.2 Anatomy of the Human Eye and Vision

The eye forms an optical system that collects light of the environment and creates an image on the retina that can be processed by the brain. Figure 2.2a shows a simplified profile

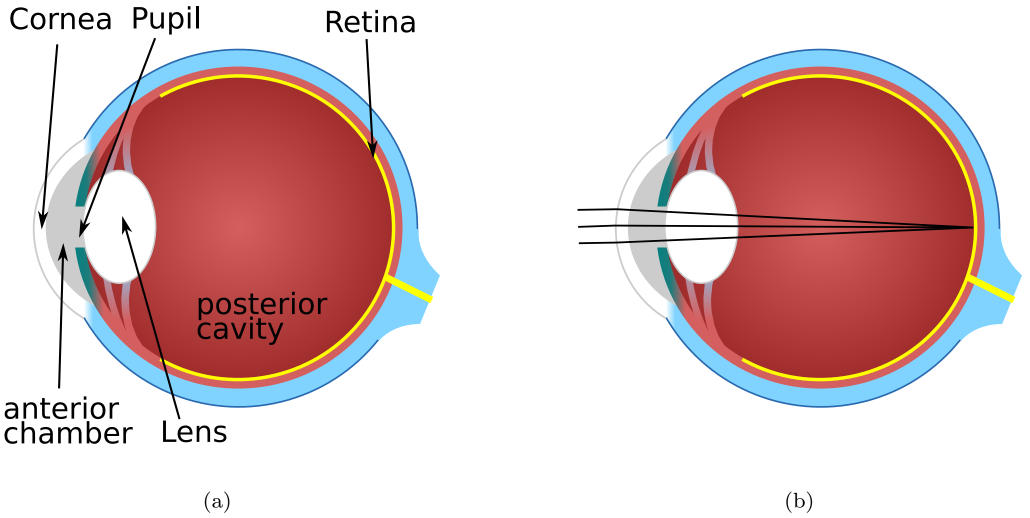

Figure 2.2. (a) Schematic representation of the eye with its main optical components. (b) Path of rays focused on the retina.

of the human eye with its main optical components: the cornea, pupil, lens and retina. The anterior chamber is filled with aqueous humour and the posterior cavity is filled with vitreous humour.

The incoming light is focused onto the retina by refraction at the different refractive interfaces of the eye (*cf.* Fig. 2.2b). Refractive interfaces originate between two media with different refractive indexes. In the eye, refraction primarily takes place at four interfaces: (1) the interface between air and the tear fluid at the anterior surface of the cornea, (2) the interface between the cornea and the aqueous humour at the posterior surface of the cornea, (3) the interface between aqueous humour and the lens at the anterior surface of the lens and (4) the interface between the lens and the vitreous humour at the posterior surface of the lens.

The refraction of the light rays at the interface between two media can be described by Snell's law:

$$\frac{\sin\theta_1}{\sin\theta_2} = \frac{n_2}{n_1}\,,$$

where n_1 and n_2 are the refractive indexes of the first and second medium, respectively, and θ_1 and θ_2 are the angles of the ray in the corresponding medium, relative to the interface normal.

In reality, the cornea and the lens are not homogeneous, forming weak refractive interfaces or gradients. However, the cornea and the lens are usually treated to have a uniform refractive index.

The amount of light on the retina is controlled by the aperture of the pupil, built by the iris of the eye.

The cornea alone accounts for two thirds of the eye's refractive power, where the refraction at the anterior surface is dominant because of the big difference in refractive index between air and cornea. Whereas the cornea's refractive power is fixed, the shape and therefore the refractive power of the lens can be changed. This allows focussing the vision to different distances ("accommodation").

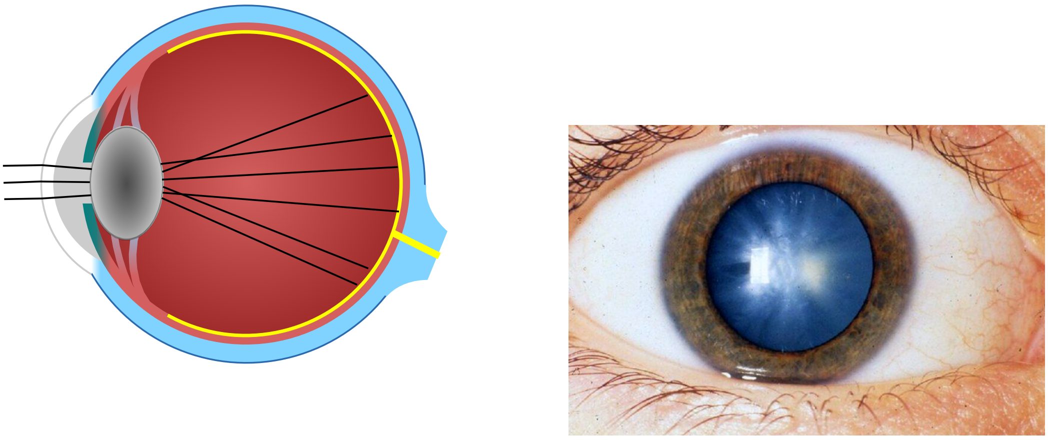

(a) (b)

Figure 2.3. (a) Schematic representation of a cataract (clouded lens) and the resulting scattering of the light. (b) Photograph of an eye with cataract. Photograph by National Eye Institute, National Institutes of Health under CC BY 2.0 licence.

2.2.1 Corneal Apex and Corneal Vertex

The corneal apex and the corneal vertex are two points on the cornea that are used as points of reference, *e.g.* to align two topography maps. The corneal vertex is the point of intersection between the line of sight and the anterior corneal surface, whereas the corneal apex is the point of maximum curvature on the cornea [4]. Usually, the corneal vertex and the corneal apex do not match in position, and are typically separated by a distance of around 0.6 mm [4].

2.2.2 Common Pathologies and Refractive Errors

Cataract, keratoconus and astigmatism are the pathologies and refractive errors that are most relevant for our work. The planning of cataract surgeries and the quantification of astigmatism are major applications of keratometry. The detection of keratoconus is a major application of corneal topography. Other refractive errors include near-sightedness, far-sightedness and presbyopia.

Cataract refers to the pathological clouding of the lens, occurring mainly in old age. The cloudy lens diffuses the light, resulting in blurred vision up to blindness (see Fig. 2.3). Worldwide, cataract is responsible for half of all cases of blindness. In cataract surgery, the natural lens is replaced by an artificial intraocular lens (IOL).

Keratoconus refers to a pathology which results in progressive thinning of the cornea and loss of structural integrity of the cornea, leading to blurry vision, near-sightedness and light sensitivity (see Fig. 2.4). The disease leads to a characteristic conical shape of the cornea. It usually emerges in early adulthood and stabilises after a few years. Although the effects of keratoconus on the vision can be corrected to some amount by glasses or contact lenses, there is no cure for this disease. In rare cases, scarring of the cornea occurs and corneal transplantation is required.

Astigmatism refers to a refractive error where the light is not focused evenly on the retina but dependent on the axis, which leads to blurred vision. Astigmatism is quantified

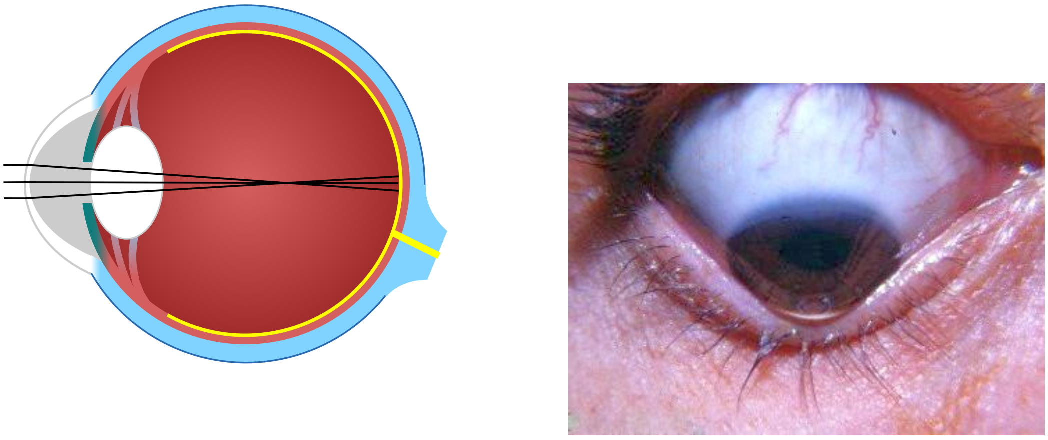

(a) (b)

Figure 2.4. (a) Schematic representation of a keratoconus (thinned, conical cornea) and the resulting path of rays characteristic for nearsightedness. (b) Photograph of an eye with keratoconus. Photograph by William Charles Caccamise, MD under CC BY SA 4.0. licence.

by the axes and refractive power of the meridian with the highest refractive power (steep meridian) and lowest refractive power (flat meridian). In regular astigmatism, the flat and steep meridian are perpendicular to each other by definition. In irregular astigmatism, they are not. Regular astigmatism is divided into three categories: with-the-rule astigmatism, against-the-rule astigmatism and oblique astigmatism. Most of the population have with-the-rule astigmatism where the meridian with the highest refractive power (steep meridian) is more or less vertical (*cf.* Sec. 2.5). Against-the-rule astigmatism refers to eyes where the steep meridian is more or less horizontal. In oblique astigmatism, the steep axis is somewhere in between.

2.3 Corneal Topography

Ophthalmologists rely on corneal topography to evaluate the shape and refractive power of the cornea. The devices that provide corneal topography are called topographers. Corneal topography in the narrow sense refers to the mapping of the curvature or refractive power of the cornea. In a wider sense, corneal topography also includes the mapping of the elevation (elevation maps) or thickness of the cornea (pachymetry maps). Topography can also be applied to the posterior corneal surface. When the anterior and posterior corneal surface can be measured, so-called *total corneal refractive power maps* can be generated as well.

In the following, we refer to corneal topography as mapping of the curvature or refractive power of the anterior corneal surface along its meridians. This mapping results in a circular map where the curvature or refractive power is usually colour coded. Normally, the curvature or refractive power is mapped for a circular area around the corneal vertex with an outer radius between 4 mm and 7 mm. For corneal topography according to the ISO topography norm [5], a minimum radius of 3.75 mm is required. According to the same norm, a valid topography value can only be given for positions on the cornea that are within a maximal distance of 0.5 mm to a sampling point, which yields a lower limit for the sampling density. The curvature is defined to be the reciprocal of the curvature radius. The refractive power

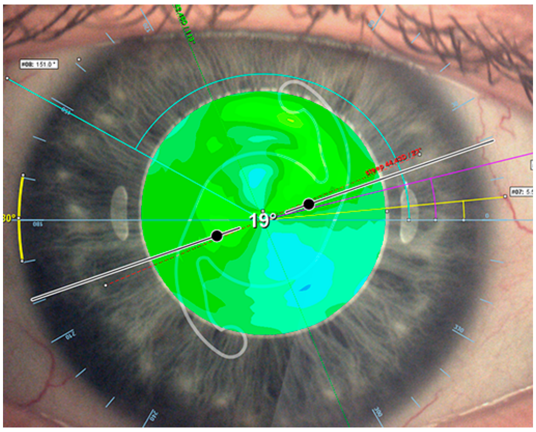

Figure 2.5. Topography map in a surgical planning tool shown as overlay on the cornea. The colour encodes the refractive power of the cornea at this point.

is usually expressed in Diopters. To determine the refractive power from the curvature, a refractive index of the cornea has to be employed. Different refractive constants are used in practice. The typically employed refractive index for the cornea is 1.3375 [6], which provides an estimation of the total corneal power based on the curvature of the anterior surface – incorporating the refractive power of the posterior surface. Figure 2.6 shows an example of a corneal topography map for an eye with slight astigmatism.

Usually, topography maps either map the so-called axial curvature, the meridional curvature, or the corresponding refractive power. The axial curvature is defined as $K_a = \frac{1}{r_a}$, where r_a is the axial radius of curvature. The axial radius of curvature is defined by the intersection distance of the meridional surface normal with the topographer axis, which is the axis parallel to the visual axis of the topographer going through the vertex of the cornea (see Section 2.2.1).

Alternatively, it can be calculated from the meridional curvature K_m by integration:

$$K_a = \frac{\int_0^r K_m(r)dr}{r_p}, \tag{2.1}$$

where r_p is the distance from the corneal vertex at which K_a is evaluated. K_m is the local surface curvature in the meridional plane.

2.3.1 Placido Disc-Based Topography

In Placido Disk-based topography, a series of concentric rings is projected onto the cornea. The tear film-air interface on the cornea acts as a convex mirror and the reflection of the rings is captured by camera (see Fig. 2.7). The slope of the cornea at the reflection points is derived from the radial distances of the rings. Because Placido Disc-based topography does not measure the elevation, the elevation has to be calculated from the curvature if needed, e.g. for the generation of elevation maps.

An example for an established Placido Disk-based topographer is the Atlas 9000 (Carl Zeiss Meditec, Jena, Germany).

2.3.2 Scanning-Slit and Scheimpflug Topography

In scanning-slit topography, a series of light slits is passed over the cornea at an angle of about 45°. The slit light is scattered by the cornea and captured by a camera, using the

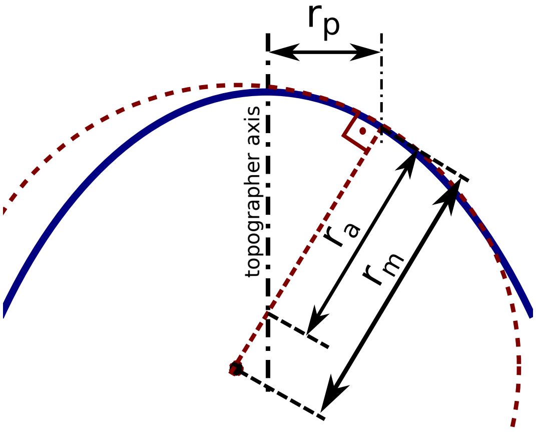

Figure 2.6. Illustration of axial curvature $K_a = \frac{1}{r_a}$ and the meridional curvature $K_m = \frac{1}{r_m}$.

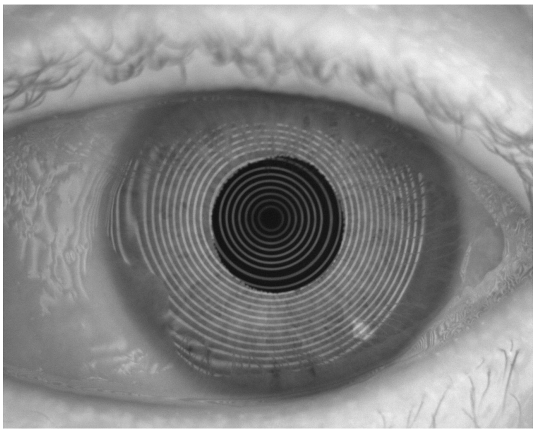

Figure 2.7. Placido Disc reflections.

same principle that slit lamps use to visualise the cornea. The position of the corneal surface is determined by triangulation.

In Scheimpflug topography, a high-resolution rotating Scheimpflug camera acquires a set of cross-sectional images of the cornea with a higher depth of focus compared to scanning-slit topography. In contrast to Placido Disc-based topographers, Scheimpflug topographers are able to provide a topography of the posterior corneal surface as well. Scheimpflug topographers directly measure the elevation of both the anterior and posterior cornea based on the Scheimpflug images. The curvature maps are derived from the elevation.

The Pentacam (Oculus, Wetzlar, Germany) is a device that combines slit illumination and a Scheimpflug camera to acquire sectional images of the anterior eye chamber, providing a three-dimensional model and corneal topography.

2.4 Keratometry

Keratometry assesses the mean curvature of the anterior corneal surface and quantifies the extent and axis of astigmatism. The so-called K-readings include the radius of curvature and angle of the steep (highest curvature) and flat (smallest curvature) meridian. The difference between the two curvatures defines the amount of regular astigmatism.

In classical keratometry, objects are placed in front of the cornea. The reflection on the anterior corneal surface generates a virtual image of the objects. Based on the size of the virtual image, the radius of curvature is determined by curved mirror optics . Keratometers typically provide values for the central area of the cornea with a diameter of about 3 mm [7].

The refractive power can be calculated from the radius of curvature when the refractive index of the cornea is known. Usually, a constant refractive index is assumed. This so-called keratometric index differs for different devices. Traditionally, only the curvature of the anterior corneal surface is determined by keratometry. Typically, a refractive index of 1.3375 is used that accounts for the characteristic refractive power of the posterior corneal surface [6, 7].

Keratometers assume that the cornea has a symmetric spherocylindrical shape with a major and minor axis separated by 90 degrees. Therefore, keratometers are only able to measure and quantify regular astigmatism.

Because the cornea accounts for most of the eye's refractive power (around 44 D), the K-readings are – besides the axial eye length – the most important measures to determine the power of the IOL for cataract surgery. An error in the keratometry translates nearly 1:1 to the refractive outcome of the surgery. The posterior corneal surface contributes approximately 0.4 D of against-the-rule astigmatism to the total corneal power.

As described above, topography and keratometry both describe the refractive power of the cornea. Whereas corneal topography provides maps of the refractive power, keratometry only provides mean power and the amount of regular astigmatism. Keratometry thus fails to describe irregular corneas, such as corneas with irregular astigmatism or keratoconus [8]. However, the values provided by keratometry enable the use of well-established formulas to determine the adequate IOL for implantation during cataract surgery. Corneal topography instruments therefore often generate a measure called simulated keratometry (SimK), which approximates the classic keratometry based on the topography.

2.5 Variations in the Shape of the Human Eye

We believe that the knowledge about the variations in the shape of the eye is essential in order to develop methods for the measurement of the eye. In this section, we show the distribution of the most relevant measures of the eye. The data is based on the measurement of 150 eyes from 77 subjects, performed at the Eye Clinic of the University Hospital of Basel. Figure 2.8 shows the age distribution. The data includes 105 phakic eyes (containing the natural lens) and 45 pseudophakic eyes, where the natural lens was replaced by an IOL. Each eye was measured twice.

Except for the shape measure p, the measures were determined by the LENSTAR 900 Biometer (Haag-Streit, Köniz, Switzerland). The shape measure p describes the shape of the

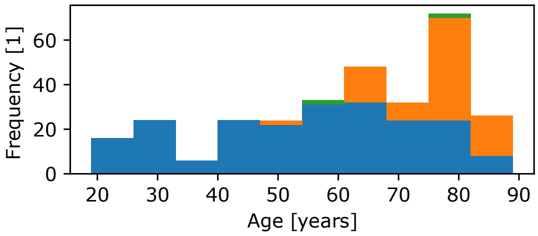

Figure 2.8. Histogram of the patient age for each eye (blue: phakic, orange: pseudophakic, green: failed measurement).

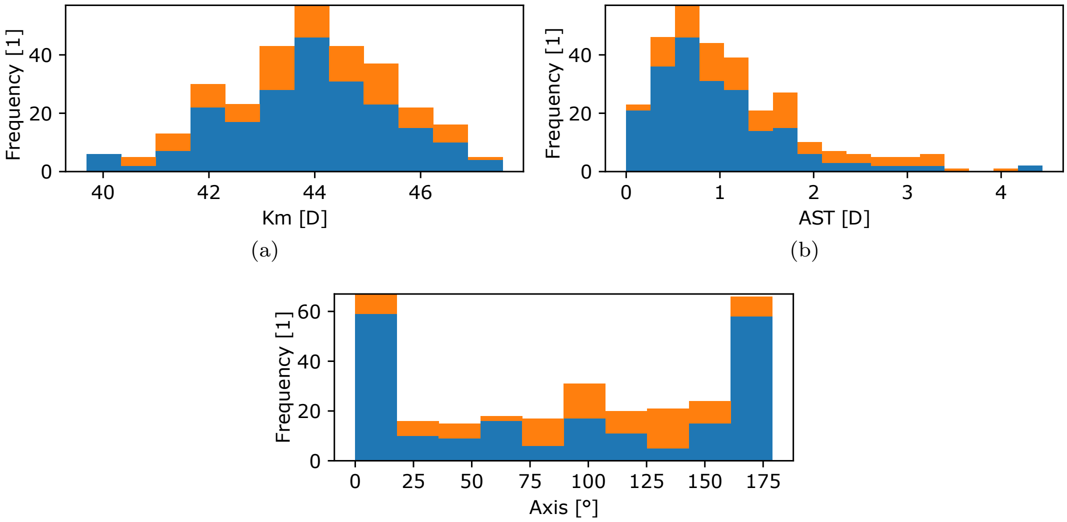

(a) (b)

(c)

Figure 2.9. Histogram of the K-values (blue: phakic, orange: pseudophakic; Device: LENSTAR 900) (a) Mean K (mean 43.90 D, median 43.93 D) (b) Astigmatism (Mean 1.11 D, Median 0.92 D) (c) Axis

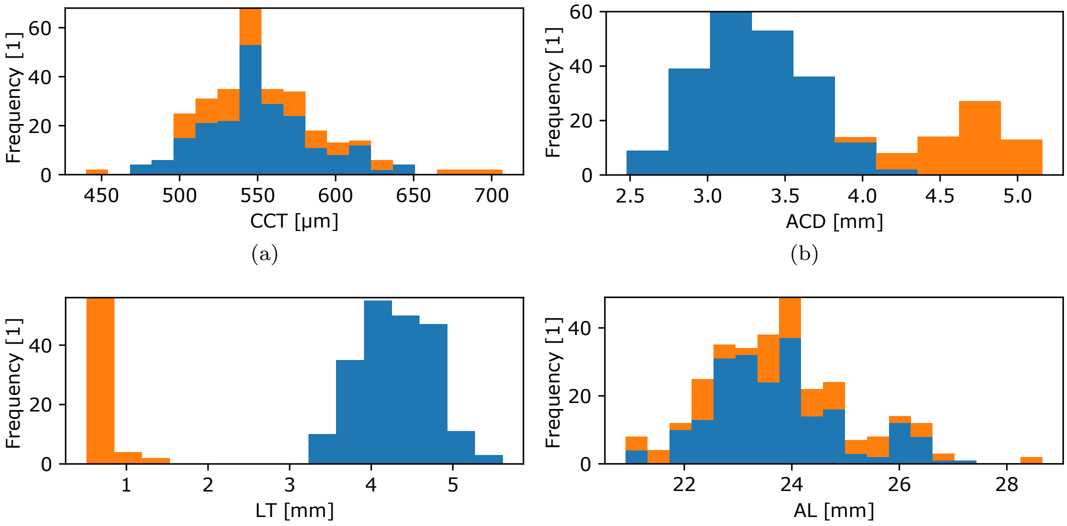

(a) (b)

(c) (d)

Figure 2.10. Histogram of the A-values (blue: phakic, orange: pseudophakic; Device: LENSTAR 900) (a) CCT (Mean 553.9 µm, Median 548 µm) (b) ACD (Mean 3.60 mm, Median 3.42 mm) (c) LT (Mean 3.48 mm, Median 4.13 mm) (d) AL (Mean 23.80 mm, Median 23.71 mm).

cornea, where a value of 1 refers to a spherical shape (see Sec. 6.2.1). The shape measure p was determined by the Pentacam (Oculus, Wetzlar, Germany) because the LENSTAR 900 does not provide a shape measure. For 14 of the pseudophakic eyes, the LENSTAR

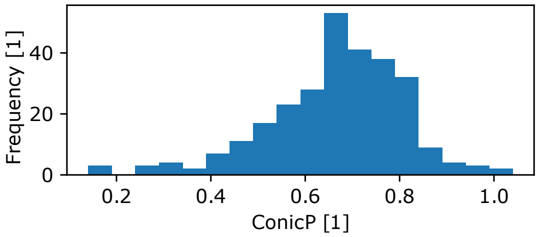

Figure 2.11. Histogram of the asphericity (blue: phakic/pseudophakic; Device: Pentacam) shape measure p (Mean 0.67, Median 0.68).

900 did not provide a value for the lens thickness (LT) and anterior chamber depth (ACD), presumably because it was not able to delineate the intraocular lens.

Figure 2.9 shows different measures provided by keratometry (*cf.* Section 2.4), including the mean refractive power (Km), the amount of astigmatism (AST) and the axis of astigmatism (Axis). As can be seen, The axis shows an accumulation around 0°, which corresponds to with-the-rule astigmatism (see Section 2.4).

Figure 2.10 shows the most essential A-values, including the central corneal thickness (CCT), anterior chamber depth (ACD), lens thickness (LT) and eye length (AL). As can be seen, the phakic and pseudophakic eyes are separated in their ACD and LT. Figure 2.11 shows the distribution of the shape measure p, the measure for the corneal asphericity, showing that the typical cornea has an aspherical shape and flattens out towards the periphery (see Chapter 6).

2.6 Eye Motion

As already mentioned, eye motion is a major problem for ophthalmic OCT-measurements. Eye motion can be caused by the movement of the eye itself or indirectly by movements of the head. For ophthalmic measurements, head movements are usually minimised by using headrests, and eye movements are minimised by asking the patient to fixate on a fixation target. However, these measures cannot prevent eye motion completely. Figure 5.5 shows the different movements of the eye. Head movement includes displacement as well as rotation. But because the line of sight is usually fixated on a target at infinity, head rotations are compensated by counter-rotation of the eye [9]. Thus, head movements primarily result in displacement of the eye. Kasparak *et al.* [10] investigated the head displacements that remain

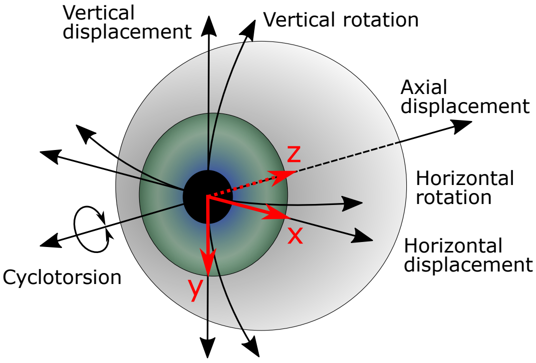

Figure 2.12. The movement of the eye and its axes.

when using a standard ophthalmic headrest. They observed amplitudes around 100 µm and frequencies of up to 3 Hz – correlating with heartbeat and respiration. These values are consistent with other investigations [11, 12] and our own experience.

Even when the patient is fixating on a target, small unintentional eye movements, so-called fixational eye movements (FEMs), occur. These small vertical and horizontal rotations include microsaccades, drifts and tremors. Investigations showed [13, 14] that FEMs are essential to prevent visual fading during fixation. According to Listing's law [9], the torsion, the rotation around the line of sight, is zero when the head is motionless - which we assume to be true in our case. Ko *et al.* [15] investigated intersaccadial eye movements, which includes drift and tremor. They observed amplitudes from 1.0 arcmin at 4.0 Hz down to 0.1 arcmin at 10 Hz. For corneal topography, we are primarily interested in corneal movements. Because the point of rotation is near the eye's centre, rotation around the lateral axes leads to combined rotation and linear displacement of the cornea. Assuming a distance of 2 cm to the rotation center, a rotation of 1.0 arcmin leads to a corneal translation of 5.8 µm in lateral and 0.85 nm in axial direction. This is an order of magnitude lower than the motion caused by head movements. Microsaccades sporadically occur at an average rate of 1 to 2 per second with durations around 10 ms [16]. In the literature, values for the amplitude vary strongly due to indefinite differentiation between voluntary saccades and involuntary microsaccades. Nevertheless, the majority of microsaccades observed in a variety of tasks has shown amplitudes smaller than 30 arcmin [17], which would result in corneal translation around 174 µm.

To summarise, we primarily expect continuous corneal displacements with amplitudes around 100 µm and frequencies up to 3 Hz. Additionally, sporadic microsaccades cause lateral displacements up to 174 µm with durations around 10 ms.

2.7 Demands on the Accuracy

In this section, we investigate the accuracy and number of samples needed for the measurement of the corneal shape by OCT. The central area of the anterior corneal surface is most relevant for vision and therefore also for IOL selection.

For this estimation, we assume a spherical shape of the cornea and only take into consideration the central 3 mm in diameter of the cornea. This is approximately the area that is characterised by common keratometers [7]. We further assume a system with an full width at half maximum axial resolution of 40 µm where the data is discretised to 12 µm axial image resolution, which corresponds to our system. To achieve an error below 0.5 D for a vast majority of the cases, we aim for a standard deviation of the curvature measurement of around 0.2 D.

Figure 2.13 illustrates the change in shape that corresponds to a change of 0.2 D around the typical radius of curvature of 7.8 mm. A radius of curvature of 7.8 mm corresponds to a refractive power of 43.27 D, assuming a corneal refractive index of 1.3375 The radius of curvature changes to 7.764 mm for an increase in refractive power of 0.2 D to 43.47 D. At a lateral distance of 1 mm, this results in an increase of 0.3 µm in axial distance with 64.67 µm compared to 64.37 µm. This shows that the determination based on a spatial measurement with a supposed axial resolution of 40 µm is challenging. Even at a lateral distance of 4 mm, the increase in axial distance of 6 µm is still well below the supposed axial resolution.

A sphere is uniquely determined by four points that are not coplanar. When sampling the cornea by OCT, the positions of the sampled points underlie an uncertainty that translates to an uncertainty of the fitted sphere parameters. If the error in position is independent between the sampling points, which we assume, a higher number of points decreases the uncertainty of the fitted sphere parameters. We want to estimate the needed number of

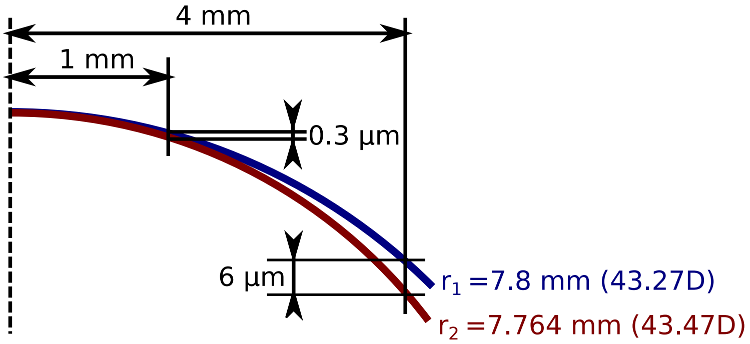

Figure 2.13. Two spherical refractive interfaces with a refractive power difference of 0.2 D, assuming a refractive index difference of 0.3375.

sampling points, assuming a certain uncertainty of the sampling points.

The uncertainty of the axial position depends on the axial resolution of the system, the image resolution and the signal-to-noise ratio. We define the signal-to-noise ratio as $\mathrm{SNR} = \frac{\mu_{\mathrm{sig}} - \mu_{\mathrm{bg}}}{\sigma_{\mathrm{bg}}}$, where μ_{sig} is the average signal value, σ_{bg} is the standard deviation of the background value and μ_{bg} the average background value. The axial resolution of the system defines the sharpness of the corneal surface feature in the signal. If the feature is less sharp, the feature is less well defined and the same amount of noise has more influence on the position of the maximal signal. Even without any noise, the discrete nature of the OCT image inhibits the exact localisation of the maximum, adding uncertainty to the axial position. Because the eye moves continuously, the position of the discretisation intervals relative to the corneal surface varies over the measurement time. We simulated the distribution of the position of the maximum assuming a Gaussian feature signal with a full width at half maximum of 40 µm and a regular sampling in the axial direction. If we assume that each A-scan is sampled with a random phase (due to the eye movement), this results in a uniform distribution, where the width is dependent on the axial image resolution (see Fig. 2.14 a). When adding noise to the sampled intensities, the distribution broadens and loses uniformity (see Fig. 2.14 b). A signal-to-noise ratio of 20 and an axial image resolution of 12 µm results in a standard deviation of the position of 3.6 µm.

Thus, the ratio between axial system resolution, image resolution and signal-to-noise ratio determines the number of measurement points needed to determine the radius with the desired accuracy. We simulated the effect of the axial uncertainties on the uncertainty of the sphere fit. Figure 2.15 shows the influence of the number of points on the uncertainty of the sphere fit, given a constant axial uncertainty. Again, the axial uncertainty is modelled with a signal-to-noise ratio of 20 and an axial image resolution of 12 µm.

The lateral positions are also subject to uncertainty, e.g. due to uncertainties in the scan positions. The effect of errors in the lateral positions is dependent on the slope of the sphere at this position. The effect at the centre of the sphere is minimal while peripheral errors have a greater impact. We simulated the effect of the lateral uncertainty on the uncertainty of the sphere fit. Figure 2.15 also shows the influence of the number of points on the uncertainty of the sphere fit when adding lateral Gaussian noise with a σ of 30 µm. We want to point out that the model of Gaussian lateral noise is not very realistic due to the limited dynamics of the scanner. An oscillation on the scanner might be a more realistic model, but its influence on the fit depends on the used scan pattern.

Nevertheless, based on the simulation, we estimate the needed number of points in the 3 mm diameter area to be well above 1000 to determine the refractive power with a standard deviation below 0.2 D.

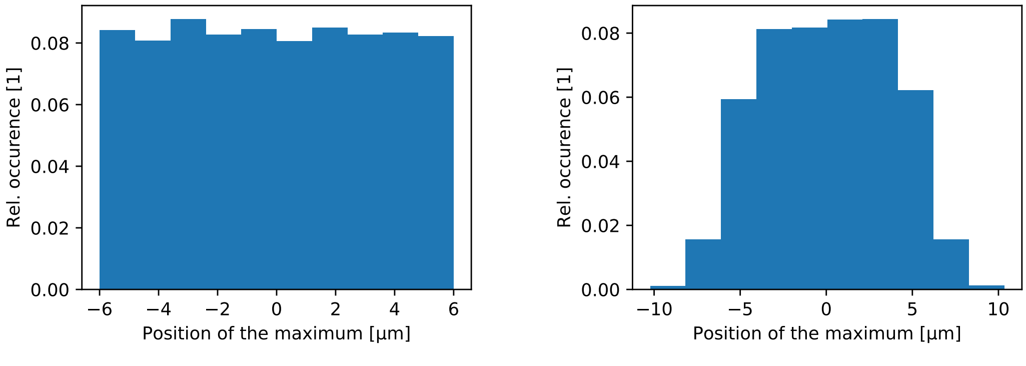

(a) (b)

Figure 2.14. (a) Influence of discretisation on the error in position of the maximum assuming an axial image resolution of 12 µm. (b) Combined influence of sampling and noise on the position of the maximum.

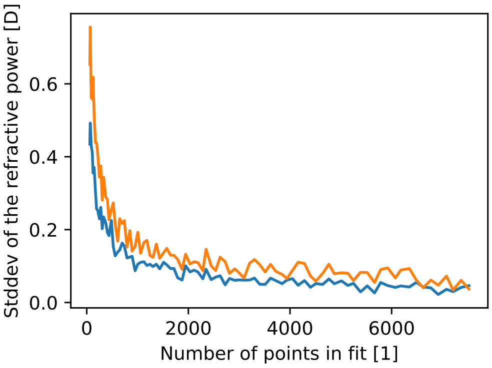

Figure 2.15. The uncertainty of the sphere fit in function of the number of points. Blue: only axial uncertainty of 3.6 µm SD, orange: with additional lateral uncertainty of 30 µm SD.

2.8 Related Work

In this section, we present the most relevant publications, patents and devices in the field of OCT-based corneal topography and keratometry. A more specific analysis of the state of the art is provided in the corresponding chapters.

2.8.1 Scientific Literature

In 2006, Li *et al.* demonstrated that OCT can be used to generate pachymetry maps. They mapped the corneal thickness before and after laser-assisted in situ keratomileusis (LASIK) with OCT and compared it to ultrasound pachymetry [18].

In 2010, Tang *et al.* determined the anterior and posterior power by curve fitting over the central 3.0 mm diameter area [19]. They used a commercially available Fourier-domain OCT system (RTVue, Optovue, Inc.) with a scan rate of 26000 A-scans/s and an axial resolution of 5 µm. In 2013, they used their OCT-based corneal power measurement for intraocular lens (IOL) power calculation following laser vision correction [20].

In 2011, Ortiz *et al.* presented a system and methods to generate corneal elevation maps from spectral domain OCT [21], including a method to minimise the impact of the motions of the eye. Their system featured an axial resolution around 6.9 µm in air, an axial range of 7 mm in depth and an effective acquisition scan rate of 25000 A-scans/s. The corneal surfaces were automatically detected for quantitative analysis of the corneal elevation maps – fitted by biconicoids and Zernike polynomials. In the following years, they demonstrated that their methods enable the characterisation of corneal elevation maps in keratoconus before and after implantation of intracorneal ring segments (ICRS) [22] and enable the quantification of the ocular biometry before and after cataract surgery [23].

In 2011, Karnowski *et al.* [24] demonstrated the applicability of high-speed swept-source OCT to quantitative evaluation of the corneal topography and refractive power. They used an OCT device with 108000 A-scans/s, enabling dense 3-D imaging of the anterior segment within a period of less than one-fourth of a second, minimising the influence of motion artefacts on final images and topographic analysis. Their system featured 20 µm of axial resolution in tissue and an imaging depth of 9 mm.

In 2012, McNabb *et al.* introduced a method based on a special radial scan pattern [25]. Their system featured an A-scan repetition rate of 20000 A-scans/s and an axial resolution of 6.2 µm in air and 4.5 µm in the cornea. With an imaging depth of 2.2 mm, only the anterior segment of the eye was measured. In the following years, they applied their so-called *Distributed scanning volumetric SDOCT* method to several clinical applications [26, 27, 28, 29].

2.8.2 Patents

Apart from the scientific publications, several patents describe the relevant state of the art.

Patent *US7365856B2*, *Method of motion correction in optical coherence tomography imaging* of *Carl Zeiss Meditec Inc* describes a method that uses a first set of A-scans to correct a second set of A-scans for motion. A first set of A-scans is acquired within a time short enough to avoid any significant motion of the sample. A second more extensive set of A-scans is acquired over an overlapping region on the sample.

Patent *EP2797493A1*, *Process for optical coherence tomography and apparatus for optical coherence tomography* of *WaveLight GmbH* describes a similar method for motion correction.

Patent *US8403481B2*, *Methods, systems and computer program products for distributed scanning for motion artefact reduction in optical coherence tomography* of *Duke University* describes the distributed scan pattern of McNabb *et al.* (McNabb is one of the inventors).

Patent *US9101294B2*, *Systems and methods for enhanced accuracy in OCT imaging of the cornea* of *Carl Zeiss Meditec Inc* describes a set of methods, involving new scan patterns, an eye-tracking mechanism for transverse motion feedback, and advanced motion correction algorithms The patent describes the use of a motion correction method that is similar to the method in *US7365856B2* to generate a model of the cornea, from which pachymetry maps, keratometric values, and corneal power information can be generated. In addition, methods are presented for determining simulated keratometry values from optical coherence tomography data.

2.8.3 Products

Furthermore, different companies presented relevant devices during recent years.

Heidelberg Engineering presented the Anterion, a multimodal cataract and refractive imaging platform. They claim that all the measurements are based on high-resolution swept-source OCT images – including topography, tomography, anterior chamber biometry and eye length measurement.

Zeiss introduced the IOLMaster 700, their “next-generation biometry device”. The device enables OCT imaging across the entire length of the eye and provides all necessary measures for the determination of IOLs. The swept-source frequency-domain OCT enables 44 mm scan depth with 22 µm resolution in tissue [30]. It uses telecentric keratometry for corneal power measurements [31].

Tomey introduced the Casia2, a 3-D swept-source OCT device that provides both OCT-based keratometry and topography. It features a scan rate of 50000 A-scans/s and an axial resolution of 10 µm. For corneal topography, it acquires 16 radial scans of 800 A-scans each in 0.3 s over a range of 16 mm. Currently, the Casia2 is limited to the anterior segment of the eye and is not capable of measuring the eye length, which is a crucial parameter for the planning of cataract surgeries.

References

[1] Sebastian Marschall et al. “Optical coherence tomography—current technology and applications in clinical and biomedical research”. In: *Analytical and bioanalytical chemistry* 400.9 (2011), pp. 2699–2720.

[2] Johannes F De Boer, Rainer Leitgeb, and Maciej Wojtkowski. “Twenty-five years of optical coherence tomography: the paradigm shift in sensitivity and speed provided by Fourier domain OCT”. In: *Biomedical optics express* 8.7 (2017), pp. 3248–3280.

[3] Zahid Yaqoob, Jigang Wu, and Changhuei Yang. “Spectral domain optical coherence tomography: a better OCT imaging strategy”. In: *Biotechniques* 39.6 (2005), S6–S13.

[4] Rafael Navarro, Luis González, and José L Hernández. “Optics of the average normal cornea from general and canonical representations of its surface topography”. In: *JOSA A* 23.2 (2006), pp. 219–232.

[5] ISO-19980:2012. *Ophthalmic instruments - Corneal topographers.* Tech. rep. International Organization for Standardization, 2012.

[6] Pier Giorgio Gobbi, Francesco Carones, and Rosario Brancato. “Keratometric index, videokeratography, and refractive surgery”. In: *Journal of Cataract & Refractive Surgery* 24.2 (1998), pp. 202–211.

[7] Thomas Olsen. “Calculation of intraocular lens power: a review”. In: *Acta Ophthalmologica Scandinavica* 85.5 (2007), pp. 472–485.

[8] Donald R Sanders, James P Gills, and Robert G Martin. “When keratometric measurements do not accurately reflect corneal topography”. In: *Journal of Cataract & Refractive Surgery* 19 (1993), pp. 131–135.

[9] JD Crawford and T Vilis. “Axes of eye rotation and Listing’s law during rotations of the head”. In: *Journal of neurophysiology* 65.3 (1991), pp. 407–423.

[10] Henryk T Kasprzak and D Robert Iskander. “Ultrasonic measurement of fine head movements in a standard ophthalmic headrest”. In: *IEEE Transactions on Instrumentation and Measurement* 59.1 (2010), pp. 164–170.

[11] Michael Pircher et al. “Simultaneous SLO/OCT imaging of the human retina with axial eye motion correction”. In: *Optics express* 15.25 (2007), pp. 16922–16932.

[12] D Robert Iskander and Henryk T Kasprzak. “Dynamics in longitudinal eye movements and corneal shape”. In: *Ophthalmic and Physiological Optics* 26.6 (2006), pp. 572–579.

[13] Susana Martinez-Conde, Stephen L Macknik, and David H Hubel. “The role of fixational eye movements in visual perception”. In: *Nature Reviews Neuroscience* 5.3 (2004), pp. 229–240.

[14] Michael B McCamy, Stephen L Macknik, and Susana Martinez-Conde. “Different fixational eye movements mediate the prevention and the reversal of visual fading”. In: *The Journal of physiology* 592.19 (2014), pp. 4381–4394.

[15] Hee-kyoung Ko, D Max Snodderly, and Martina Poletti. “Eye movements between saccades: Measuring ocular drift and tremor”. In: *Vision research* 122 (2016), pp. 93–104.

[16] Jorge Otero-Millan et al. “Saccades and microsaccades during visual fixation, exploration, and search: foundations for a common saccadic generator”. In: *Journal of vision* 8.14 (2008), pp. 21–21.

[17] Martin Rolfs. “Microsaccades: small steps on a long way”. In: *Vision research* 49.20 (2009), pp. 2415–2441.

[18] Yan Li, Raj Shekhar, and David Huang. “Corneal pachymetry mapping with high-speed optical coherence tomography”. In: *Ophthalmology* 113.5 (2006), pp. 792–799.

[19] Maolong Tang et al. “Corneal power measurement with Fourier-domain optical coherence tomography”. In: *Journal of Cataract & Refractive Surgery* 36.12 (2010), pp. 2115–2122.

[20] David Huang et al. “Optical coherence tomography–based corneal power measurement and intraocular lens power calculation following laser vision correction (an American Ophthalmological Society thesis)”. In: *Transactions of the American Ophthalmological Society* 111 (2013), pp. 34–45.

[21] Sergio Ortiz et al. “Corneal topography from spectral optical coherence tomography (sOCT)”. In: *Biomedical optics express* 2.12 (2011), pp. 3232–3247.

[22] Sergio Ortiz et al. “Quantitative OCT-based corneal topography in keratoconus with intracorneal ring segments”. In: *Biomedical optics express* 3.5 (2012), pp. 814–824.

[23] Sergio Ortiz et al. “Full OCT anterior segment biometry: an application in cataract surgery”. In: *Biomedical optics express* 4.3 (2013), pp. 387–396.

[24] Karol Karnowski et al. “Corneal topography with high-speed swept source OCT in clinical examination”. In: *Biomedical optics express* 2.9 (2011), pp. 2709–2720.

[25] Ryan P McNabb et al. “Distributed scanning volumetric SDOCT for motion corrected corneal biometry”. In: *Biomedical Optics Express* 3.9 (2012), pp. 2050–2065.

[26] Anthony N Kuo et al. “Corneal biometry from volumetric SDOCT and comparison with existing clinical modalities”. In: *Biomedical optics express* 3.6 (2012), pp. 1279–1290.

[27] Ryan P McNabb, Anthony N Kuo, and Joseph A Izatt. “Quantitative single and multi-surface clinical corneal topography utilizing optical coherence tomography”. In: *Optics letters* 38.8 (2013), pp. 1212–1214.

[28] Ryan P McNabb, Anthony N Kuo, and Joseph A Izatt. “Expanding OCT: Quanitifying the Cornea’s Optical Performance”. In: *Optics and Photonics News* 25.4 (2014), pp. 34–41.

[29] Ryan P McNabb et al. “Optical coherence tomography accurately measures corneal power change from laser refractive surgery”. In: *Ophthalmology* 122.4 (2015), pp. 677–686.

[30] Kathleen S Kunert et al. “Repeatability and agreement in optical biometry of a new swept-source optical coherence tomography–based biometer versus partial coherence interferometry and optical low-coherence reflectometry”. In: *Journal of Cataract & Refractive Surgery* 42.1 (2016), pp. 76–83.

[31] Leyla Asena et al. “Comparison of Keratometry Obtained by a Swept Source OCT-Based Biometer with a Standard Optical Biometer and Scheimpflug Imaging”. In: *Current eye research* (2018), pp. 1–7.

3 Publication: Golden Angle Based Scanning for Robust Corneal Topography with OCT

Our first publication addresses a problem limiting the use of OCT in a specific clinical application, namely the problem of patient induced abrupt distortions such as eye motion or blinking during corneal topography. The standard straight-forward solution is to reduce the measurement time by using expensive high-speed OCT systems. We follow an alternative, less hardware demanding approach to reduce the susceptibility to this form of distortions. We introduce a tailored sampling method that combines the beneficial properties of spiral scanning and the golden angle. The combination of spiral scanning with a continuous golden angle rotation leads to well-balanced and self-refining sampling. The improved performance is backed up by thorough numerical analysis and is demonstrated experimentally.

The results show that with the presented method, the reliability of the corneal topography is increasing with measurement time and that distorted parts of a measurement can be removed without corrupting the reliability. This enables corneal topography from distorted measurements by excluding the distortions and reduces the need for repeated measurements. Our method represents a superior trade-off between sampling density and resistance to distortions which cannot be achieved by conventional scanning methods. Because the presented method eases the common trade-off between sampling density and resistance to distortions, it is also relevant for researchers from other fields where distortions can occur while scanning a structure.

Publication The paper was published in the issue ”25 Year Anniversary of Optical Coherence Tomography” of the *Biomedical Optics Express* of the *Optical Society of America* on 1 February 2017 [1].

We present the work as published, with minor changes in the layout. We refer to Section 7 for the discussion of the methods considering the latest findings. We incorporated the major principles of this publication into a patent (see Appendix).

Reference

[1] Joerg Wagner, David Goldblum, and Philippe C Cattin. “Golden angle based scanning for robust corneal topography with OCT”. In: *Biomedical Optics Express* 8.2 (2017), pp. 475–483.

Abstract

Corneal topography allows the assessment of the cornea's refractive power which is crucial for diagnostics and surgical planning. The use of Optical Coherence Tomography (OCT) for corneal topography is still limited. One limitation is the susceptibility to disturbances like blinking of the eye. This can result in partially corrupted scans that cannot be evaluated using common methods. We present a new scanning method for reliable corneal topography from partial scans. Based on the golden angle, the method features a balanced scan point distribution which refines over measurement time and remains balanced when part of the scan is removed. The performance of the method is assessed numerically and by measurements of test surfaces. The results confirm that the method enables numerically well-conditioned and reliable corneal topography from partially corrupted scans and reduces the need for repeated measurements in case of abrupt disturbances.

3.1 Introduction

Precise measurement of the cornea's refractive power is crucial for the reliable planning of refractive and cataract surgeries, since the cornea accounts for most of the eye's refractive power. Corneal topography provides two-dimensional maps of the cornea's curvature, which enables the assessment of its refractive power and aberrations. Therefore, the accuracy of the corneal topography has direct influence on the reliability of diagnoses and surgical outcomes. An accurate determination of the corneal shape allows to detect pathological deformations, such as keratoconus, at an early stage [1]. Corneal topography also enables geometrically correct measurement of sub-surface structures.

Placido disc reflection, scanning slit and Scheimpflug photography are established methods for corneal topography and represent the current clinical standard. Optical Coherence Tomography (OCT) is commonly used for cross-sectional or volumetric imaging, while its use for corneal topography is still limited. While the traditional photography-based principles enable the acquisition of 2D or 3D geometrical information of the cornea at once, OCT relies on the sequential gathering of one-dimensional axial depth profiles (A-scans) to assemble two-dimensional scans (B-scans) or volumetric scans. This increases the measurement duration and hence increases the susceptibility to disturbances like blinking of the eyelid or abrupt eye movements. These disturbances can result in distorted or incomplete scans that require repetition of the measurement. Repetition increases the examination duration and results in stress for the patients. The probability of a distortion-free measurement can be low, especially for patients suffering from tremors.

For corneal topography by OCT, the central area of the cornea is scanned at discrete locations distributed over the area, and at each location the distance to the anterior corneal surface is obtained by image segmentation. Topography maps can then be generated from a parametric representation of the reconstructed surface. Although there is no consensus about the ability of Zernike polynomials to represent all visually significant aberrations [2], they are state of the art for the description of optical aberrations and the reconstruction of optical surfaces. Due to the fact that Zernike polynomials lose their orthogonality in the discrete case [3], the used scan pattern has a direct influence on the problem's numerical condition. To achieve an accurate Zernike reconstruction, the scan pattern has to account for the radial and tangential oscillations of the Zernike polynomials. With increasing Zernike orders, the radial and tangential frequencies of the Zernike polynomials increase and require finer radial and tangential sampling. Finer sampling improves the numerical condition and potentially enables higher order reconstruction. The practicality and duration of a scan pattern are limited by the A-scan rate and scanner dynamics of the used OCT system.

To date, no scan pattern is reported to feature a balanced scan point distribution, refine over measurement time and enable reliable corneal topography from partial scans. Classic raster scanning is mainly used for volumetric imaging but also for the measurement of the cornea with subsequent Zernike reconstruction [4]. Although complete raster scans usually feature a balanced scan point distribution, missing parts lead to a patchy scan coverage and unreliable reconstruction. Recently, so-called orthogonal scan patterns [5] were used to acquire motion corrected retinal OCT volumes. These scan patterns consist of sequentially acquired raster scans with alternated fast axis. Because the B-scans acquired along the fast axis are almost motion free, the A-scans of the volumes can be registered and realigned retrospectively, resulting in a motion corrected volume. Although some kind of refinement can be achieved by the realignment of the A-scans, this type of scan pattern is not refining per se.

Another commonly used type of scan pattern consists of several meridional B-scans centered around a common point, which is usually aligned to the apex of the cornea. An advantage of these patterns is the simplification of axial motion correction, because all meridional scans share the apex as a common point. A variety of these so called radial scan patterns were used for different geometrical measurements of the cornea [6, 7, 8]. McNabb *et al.* [9] presented a special radial scan pattern for their Distributed Scanning OCT method. The scan pattern consists of 20 radial B-scans with 500 A-scans each. Spatially adjacent A-scans are not gathered sequentially, but distributed over five sub-sampled passages. This method enables finer axial motion correction compared to classic radial patterns. The method was used for the reconstruction of the cornea with 5^{th}-order Zernike polynomials and has proven its applicability for corneal topography of astigmatism [10]. Although the distributed scan pattern refines over time, this refining is limited to the radial direction. The radial scan patterns, including the distributed scan pattern, feature a concentrated central point density. The resulting unbalanced sampling potentially leads to bad numerical conditioning and reliability of Zernike reconstruction.

In this paper we introduce a new scanning method for OCT based corneal topography. The method features a balanced scan point distribution which refines over measurement time and remains balanced, even when part of the scan is missing. This enables reliable Zernike reconstruction from short or fractional scans and reduces the need for repeating measurements due to distortions i.e. blinking or abrupt movement of the patient.

3.2 Methods

3.2.1 Scan Pattern

In this paper we introduce a novel scan pattern which is based on Fermat's spiral and implements two new properties: repetition and golden angle refinement. The use of Fermat's spiral is advantageous since it combines fast coverage of a circularly shaped area while featuring a balanced scan point distribution. The Fermat spiral was proposed by Navarro *et al.* [3] for their invertible discrete Zernike transform – providing non-redundant sampling and completeness of the resulting Zernike expansion.

The basic Fermat spiral is defined by the equation $r = \pm\theta^{1/2}$, where r is the radius and θ the angle of the polar coordinates. To implement repetition, the spiral was adapted for a radius that repetitively sweeps linearly from zero to a maximal radius (of typically 3.75 mm) and back, resulting in a spiral that sweeps out and in. One cycle of the resulting pattern consists of two adjacent sweeps: one from the center to the circumference and one back. The first cycle of the scan pattern is shown in Fig. 3.1(a).

For refinement, a continuous rotation was added to each cycle, such that two subsequent cycles are rotated by an angle θ_r with respect to each other. To obtain a well balanced

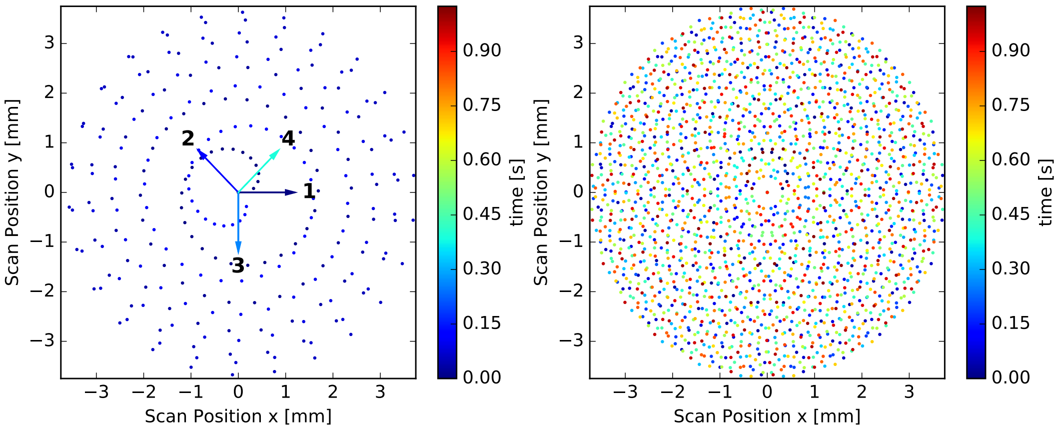

(a)

(b)

Figure 3.1. The refining scan pattern with a sampling rate of 2 kHz. (a) Scan points of the first cycle and the initial orientations of the first four cycles. Each successive cycle is rotated with respect to the previous one by an approximation of golden angle. (b) Scan points of the complete pattern consisting of eight cycles.

sampling for any subsection of the scan pattern we used the golden angle $\theta_g = 0.381966 \times 2\pi$ as basis for the refinement (see next section). We approximated the golden angle by $0.375 \times 2\pi$ to obtain a finite scan pattern. As shown in Fig. 3.1(b), this approximation of the golden angle leads to a repetition after eight cycles, while preserving the advantageous property of balanced refining.

Due to this particular choice of spiral trajectory, the sampling density continuously refines in tangential as well as in radial direction. We defined 256 scan points per cycle by regular sampling in θ which results in $8 \times 256 = 2\,048$ points in total. For a sampling rate of 2 kHz this leads to a duration of 1.024 s.

Golden Angle Refinement

Our technique uses a continuous rotation of the scan pattern to achieve a refinement of the scanning with time. By using the golden angle as basis, our method uses a property of the golden ratio that is also used by nature. Growing plants position their new leaves with as little overlap with previously grown leaves as possible in order to avoid unwanted shadowing of previous leaves. Some flowers leave an angle between succeeding leaves of around 137.508° to minimize the overlap [11]. This angle is also known as golden angle and is the smaller angle created by sectioning a circle (360°) according to the golden ratio. The golden angle in radians is given by

$$\theta_g = \frac{1}{1+\Phi} 2\pi \approx 0.381966 \times 2\pi\,, \tag{3.1}$$

where Φ is the golden ratio ($\Phi \approx 1.618034$).

The golden angle is already used for iterative image reconstruction in computed tomography (CT) [12]. To achieve good iterative image reconstruction, each projection has to contain information about the object which is as independent from the information contained by the previously taken projections as possible. Because this optimisation problem is quite similar to the one of the plants, the golden angle was beneficially used as angle shift between subsequent projections.

For our refinement, we used an approximation of the golden angle. Because the golden ratio is an irrational number, subsequent rotation around the golden angle would cause infinite refinement of the scan pattern and would continuously fill the gaps in the angular sampling.

3.2.2 Evaluation

We evaluate the performance of the method numerically and by measurements with the proposed scanning scheme. To minimise the experimental uncertainties, we rely on glass test surface measurements for the verification of the method. The use of test surfaces is also proposed in technical standards for the assessment of corneal topographers [13]. The practical applicability is shown separately by means of an *in vivo* use case. The radii of the two used glass surfaces were chosen to match the curvature of two typical corneas with and without astigmatism. A toric surface with radii of 7.585 mm and 7.987 mm was used to represent a cornea with astigmatism. A spherical surface with a radius of 7.805 mm was used to represent an astigmatism-free cornea. The test surfaces were manufactured by Spectros (Ettingen, Switzerland) and kindly provided by Haag-Streit (Köniz, Switzerland). We performed two scans on both of the two glass surfaces. To receive the points for the subsequent reconstruction, the front surface was segmented in the acquired scans.

We employ three measures for the verification of the proposed scanning method. First, the *condition number* assesses the theoretical bound for the accuracy of the Zernike reconstruction. Second, the *standard error of the coefficients* assesses the confidence in the reconstructed Zernike polynomials. Furthermore, the *root mean square (RMS) of the Zernike coefficients' difference* yields a measure for the difference between two Zernike reconstructions.

For the *in vivo* use case, we used measurements of a healthy patient acquired over the course of a clinical data acquisition. This data was acquired at the Eye Clinic of the University Hospital Basel with approval of the local ethics committee. The device was aligned to the apex of the eye by using a live view generated from two orthogonal B-scans.

Scan System

We used a custom swept-source OCT system at 1060 nm featuring telecentric scanning and a sweep rate of 30 kHz. A corresponding optical schematic can be found in Fig. 1(b) of the publication of Sarunic *et al.* [14]. We oversampled the presented scan pattern 15 times to receive a robust segmentation value for the scan pattern points (see next section). This leads to an actual sampling rate of 2 kHz.

The bandwidth-limited full-width at half maximum axial resolution of the system is 40 µm, and the −6 dB distance is larger than 20 mm. Image segmentation is based on data interpolated to 12 µm axial pixel dimension and an A-scan length of 10 mm in air. The power on the sample is 940 µW and the OCT sensitivity is 103 dB.

The scan pattern was calibrated based on scans of a test surface with known physical dimensions. The mean absolute deviation between the calibrated points and the specified points was 37 µm with a maximum of 73 µm. The uncertainty of the calibrated points due to scan-to-scan variations and uncertainties of the calibration method was below 30 µm.

Segmentation

We used a graph-based segmentation method, similar to the one used by LaRocca *et al.* [15], to derive the points for the following reconstruction. The segmentation was used to identify the position of the front surface in axial direction. To enhance the robustness of the segmentation, the method was adapted to use edges spanning several adjacent A-scans. As a result, one segmentation value was provided for every 15th A-scan. One segmentation value therefore is based on several adjacent A-scans.

Discrete Zernike Reconstruction

Given the x- and y-coordinates defined by the scan pattern and the z-coordinates from the segmentation, the cornea front was fitted with Zernike polynomials by linear least squares. The least squares estimation for the highly overdetermined system $\mathbf{X}\boldsymbol{\beta} = \mathbf{z}$ was found by solving

$$(\mathbf{X}^{\mathrm{T}}\mathbf{X})\hat{\boldsymbol{\beta}} = \mathbf{X}^{\mathrm{T}}\mathbf{z}\,, \tag{3.2}$$

where $\mathbf{z}$ is the vector with the z-coordinates. The variables $\boldsymbol{\beta}$ and $\hat{\boldsymbol{\beta}}$ are the Zernike coefficients and their least squares fit, respectively . The columns of matrix $\mathbf{X}$ are given by the sampled Zernike polynomials. We used polynomials up to the 6^{th} order for the reconstruction. This results in a 2048×28 matrix $\mathbf{X}$ for the complete scan pattern. The least squares reconstruction was implemented in Python/NumPy (64 bit) by means of a QR factorisation and took around 80 ms on the computer used (Intel i7-3770 CPU @ 3.4GHz, 16GB of Memory).

Condition Number

The condition number is a measure for the sensitivity of the solution to errors in the input. For a linear equation of the form $\mathbf{X}\boldsymbol{\beta} = \mathbf{z}$, the condition number is a property of the problem matrix and is defined by $\kappa(\mathbf{X}) = \left\|\mathbf{X}^{-1}\right\| \times \|\mathbf{X}\|$, or rather by $\kappa(\mathbf{X}) = \|\mathbf{X}^{+}\| \times \|\mathbf{X}\|$ for our overdetermined system, where $\mathbf{X}^{+}$ is the Moore-Penrose pseudo inverse of the non-square problem matrix. When using the euclidean norm, the condition number is given by the ratio of minimal and maximal singular values

$$\kappa(\mathbf{X}) = \frac{\sigma_{\max}(\mathbf{X})}{\sigma_{\min}(\mathbf{X})}\,. \tag{3.3}$$

From this equation one can see that $\kappa(\mathbf{X}) \geq 1$. A condition number of one indicates that the error in the input data is not amplified.

Coefficients Standard Error

The coefficients standard error is strongly related to the confidence bound for the fitted Zernike coefficients [16]. The confidence bound vector is calculated by $\mathbf{c} = \mathbf{b} \pm t\,\mathbf{s}$ where $\mathbf{b}$ is the vector with the fitted coefficients and $\mathbf{s}$ is the coefficients standard error vector. The factor t can be derived from the t-distribution and the desired confidence level. Because we have a highly overdetermined system, the distribution was assumed to be constant and the coefficients standard error was used as the measure for the confidence. The coefficients standard error vector $\mathbf{s}$ is given by the diagonal of the covariance matrix of the coefficients Σ

$$\mathbf{s} = \sqrt{\operatorname{diag}(\Sigma)}\,. \tag{3.4}$$

The estimated covariance matrix of the coefficients is given by

$$\Sigma = (\mathbf{X}^{T}\mathbf{X})^{-1}\,s^{2}\,, \tag{3.5}$$

where s is the mean squared error of the fit and $\mathbf{X}$ is the matrix of the Zernike fit. So the coefficients standard error depends on the problem matrix (which is defined by the scan pattern and the Zernike polynomials) and the fit error. Low coefficients standard errors indicate a high confidence level and reliability.

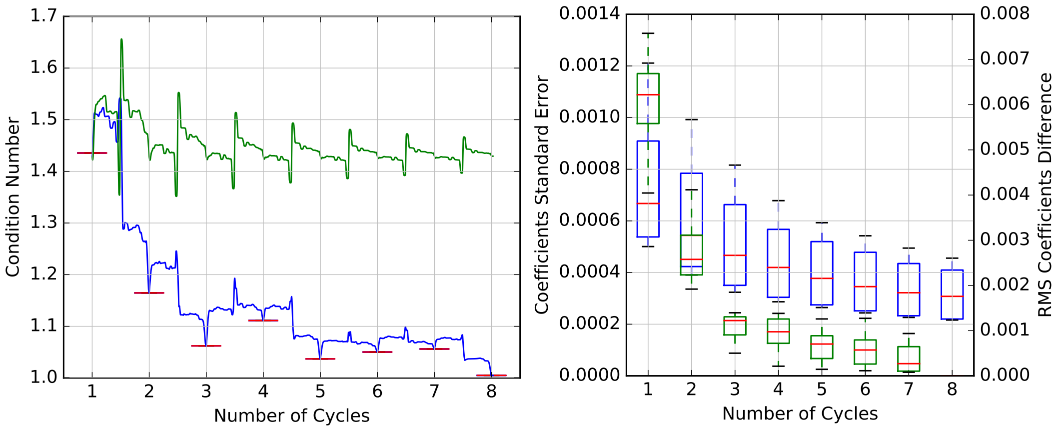

(a) (b)

Figure 3.2. (a) Condition number of the Zernike reconstruction depending on the number of adjacent cycles included for the proposed refining pattern (blue) and repeated first cycle (green). (b) Coefficients standard error (blue) and the convergence of the Zernike coefficients (green) for the four test surface reconstructions depending on the number of adjacent cycles included.

3.3 Results

3.3.1 Validation

Figure 3.2(a) shows the condition number's dependency on the number of cycles (256 points each) used for Zernike reconstruction. The curves show the course of the condition number for a certain number of points starting at the beginning of the scan. Box plots are produced from the eight sections of the scan with a particular number of adjacent cycles (the last and the first cycles are considered adjacent). As expected, the box plots show very low variance and are therefore only visible as horizontal lines. This means that the numerical condition is only dependant on the number of adjacent cycles and not the specific cycles that are used for reconstruction. The condition of the refining scan pattern steadily decreases and converges to one (blue line) while simple repetition of one cycle does not improve the numerical condition (green line). As a comparison, a radial scan pattern with 20 meridional scans with 500 points each yields a condition number of 2.5. This is worse than the condition of a single cycle of the proposed scan pattern and can not be improved by longer measurement.

Analogously, Fig. 3.2(b) shows the mean coefficients standard error for the four test surface reconstructions and the convergence of the reconstruction result measured by the root mean square of the Zernike coefficients' difference. The differences are calculated between the Zernike reconstruction, with the points of a given number of adjacent cycles, and the reconstruction of the complete scan. The characteristics are consistent with the course of the numerical condition. The convergence of the reconstruction confirms that cycles can be removed from the measurement with minimal negative impact on the reconstruction reliability. As stated in the introduction, reliable reconstruction is a prerequisite for reliable topography.

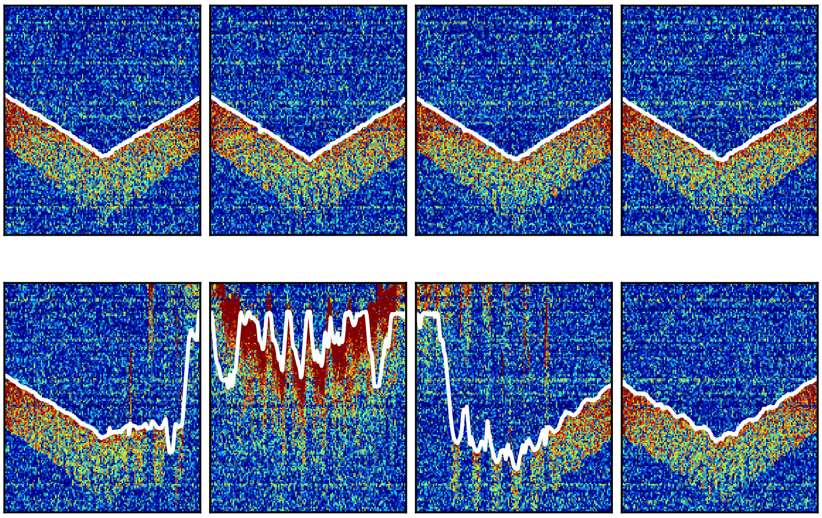

Figure 3.3. The eight individual cycles of a scan with a blinking artifact in the lower row. The segmentation of the anterior cornea is shown in white.

3.3.2 Use Case: Corneal Topography from a Partial Scan

Figure 3.3 shows a segmented *in vivo* scan from a healthy eye with a gross disturbance due to blinking of the patient. The part with the disturbance was manually excluded from the reconstruction. As seen by the small oscillations of the segmented surface, the part after the disturbance is slightly misaligned. To compensate for the misalignment between the parts, we aligned the segmented points of the two parts by means of two separate low order Zernike reconstructions. The shift between the two reconstructions was determined from the Zernike coefficients as described in [17].

Figure 3.4(a) shows the included scan points and the resulting topography map. After the overall reconstruction with 6^{th}-order Zernike polynomials, the curvature map was calculated for the central 4 mm disc as described by McNabb *et al.* [18]. For comparison, Fig. 3.4(b) shows the curvature map calculated from the reconstruction of a disturbance-free second scan of the same eye. On the used standard scale for corneal topography, both essentially look the same.

3.4 Discussion

The results of the validation show that the scanning method enables well-conditioned reconstruction from fractional scans. As shown, distorted parts of scans can be excluded from reconstruction to enable reliable corneal topography from distorted measurements. With this approach, the need for repeated measurements can be reduced. Because of the repeated coverage of the same area, distortions can easily be detected – either manually or automatically. Although our work is focused on the anterior corneal topography, the advantageous properties also apply to posterior corneal topography or the generation of pachymetry maps.

One could argue, that reconstruction from fractional scans can also be achieved by simple repetition of a basic scan pattern without refinement. However, as we have shown above, repetition does not enhance the numerical condition. Thus without the golden angle refinement, the numerical condition is limited by the basic scan pattern. With the refinement,

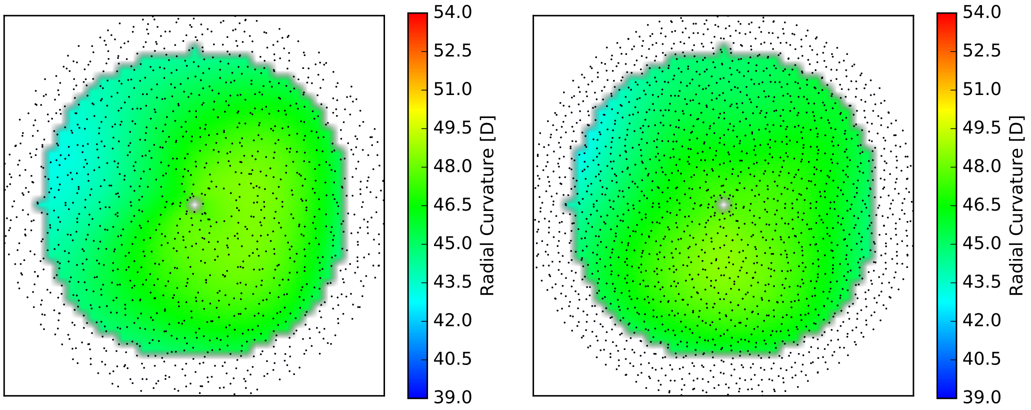

(a)

(b)

Figure 3.4. Generated corneal topography maps in diopters and the scan points used for Zernike reconstruction. (a) Topography map from a scan with blinking artifact. (b) Topography map from a disturbance free rescan.

longer measurement does not only enhance the reliability by increasing the number of points but also by improving the numerical condition. To achieve a similar performance with repetition of a scan pattern, one would have to find a scan pattern that has the same number of points as one cycle of the refining scan pattern while achieving the same numerical condition as several cycles. This is hard to achieve as one cycle of the refining scan pattern is already optimised for good numerical condition itself. Our method therefore eases the trade off between fast coverage and good numerical condition. We want to emphasise that the spiral scanning scheme itself already enables smaller measurement durations than raster scanning and enables higher Zernike orders compared to radial scanning schemes.

The critical reader might pose the question whether subsequent rotation around a fraction of a circle would not boil down to similar capabilities as rotation around the golden angle. This is not the case. Although this approach would also lead to a refinement of the scanning, the conditioning and reliability of partial reconstruction would be limited because of unbalanced sampling. Figure 3.5(b) illustrates the suboptimal sampling achieved by subsequent rotation around one eighth of a circle scan compared to the golden angle sampling in Fig. 3.5(a).

By using a different approximation of the golden angle, the number of cycles, the measurement duration and the overall point density can be adapted. For instance, an increased point density can be required if higher Zernike orders are desired. However, the optimal point density is limited by the expected amplitude of lateral motion.

The main intent of the work was to overcome the corruption of measurements by abrupt disturbances. As we have shown, the presented scanning method yields a solution for this problem. Apart from this, the main characteristics of the scanning method – it enables reconstruction from small fractions of the scan while continuously optimising the overall sampling – also is attractive for other applications. Apart from abrupt disturbances, so called fixational eye motion is another limiting factor. With the presented method, motion could be detected and compensated by cycle-wise or even half-cycle-wise reconstruction and alignment – assuming that motion during one cycle can be neglected.

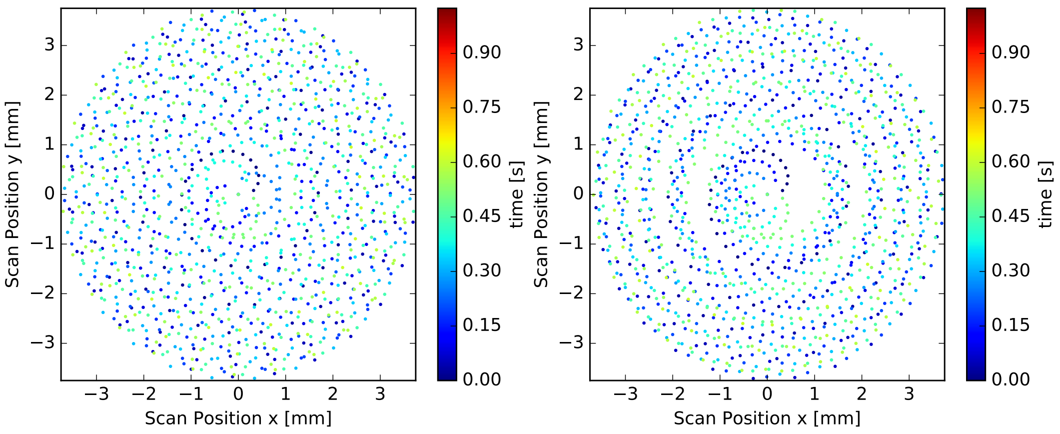

(a)

(b)

Figure 3.5. The first four cycles from the proposed refining scan pattern (a) with golden angle rotation and an alternative refining scan pattern (b) with an angle shift of $\frac{1}{8} \times 2\pi$ radians.

References

[1] Leo J Maguire and William M Bourne. “Corneal topography of early keratoconus”. In: *American Journal of Ophthalmology* 108.2 (1989), pp. 107–112.

[2] Michael K Smolek and Stephen D Klyce. “Goodness-of-prediction of Zernike polynomial fitting to corneal surfaces”. In: *Journal of Cataract & Refractive Surgery* 31.12 (2005), pp. 2350–2355.

[3] Rafael Navarro, Justo Arines, and Ricardo Rivera. “Direct and inverse discrete Zernike transform”. In: *Optics express* 17.26 (2009), pp. 24269–24281.

[4] Robert J Zawadzki et al. “Three-dimensional ophthalmic optical coherence tomography with a refraction correction algorithm”. In: *European Conference on Biomedical Optics*. Optical Society of America. 2003, 5140_20.

[5] Martin F Kraus et al. “Motion correction in optical coherence tomography volumes on a per A-scan basis using orthogonal scan patterns”. In: *Biomedical optics express* 3.6 (2012), pp. 1182–1199.

[6] Maolong Tang et al. “Corneal power measurement with Fourier-domain optical coherence tomography”. In: *Journal of Cataract & Refractive Surgery* 36.12 (2010), pp. 2115–2122.

[7] Mingtao Zhao, Anthony N Kuo, and Joseph A Izatt. “3D refraction correction and extraction of clinical parameters from spectral domain optical coherence tomography of the cornea”. In: *Optics express* 18.9 (2010), pp. 8923–8936.

[8] Sergio Ortiz et al. “Quantitative OCT-based corneal topography in keratoconus with intracorneal ring segments”. In: *Biomedical optics express* 3.5 (2012), pp. 814–824.

[9] Ryan P McNabb et al. “Distributed scanning volumetric SDOCT for motion corrected corneal biometry”. In: *Biomedical Optics Express* 3.9 (2012), pp. 2050–2065.

[10] Ryan P McNabb et al. “Optical coherence tomography accurately measures corneal power change from laser refractive surgery”. In: *Ophthalmology* 122.4 (2015), pp. 677–686.

[11] Przemyslaw Prusinkiewicz and Aristid Lindenmayer. *The algorithmic beauty of plants.* Springer Science & Business Media, 2012.

[12] Thomas Köhler. "A projection access scheme for iterative reconstruction based on the golden section". In: *Nuclear Science Symposium Conference Record.* Vol. 6. 2004, pp. 3961–3965.

[13] ANSI-Z80.23-2008. *Corneal Topography Systems - Standard Terminology, Requirements.* Tech. rep. American National Standards Institute, 2008.

[14] Marinko Sarunic et al. "Instantaneous complex conjugate resolved spectral domain and swept-source OCT using 3x3 fiber couplers". In: *Optics Express* 13.3 (2005), pp. 957–967.

[15] Francesco LaRocca et al. "Robust automatic segmentation of corneal layer boundaries in SDOCT images using graph theory and dynamic programming". In: *Biomedical Optics Express* 2.6 (2011), pp. 1524–1538.

[16] Jeff A Jones and Niels G Waller. "Computing confidence intervals for standardized regression coefficients." In: *Psychological methods* 18.4 (2013), pp. 435–453.

[17] Boy Braaf et al. "Calculating angle lambda (λ) using zernike tilt measurements in specular reflection corneal topography". In: *Journal of Optometry* 2.4 (2009), pp. 207–214.

[18] Ryan P. McNabb, Anthony N. Kuo, and Joseph A. Izatt. "Quantitative single and multi-surface clinical corneal topography utilizing optical coherence tomography". In: *Opt. Lett.* 38.8 (2013), pp. 1212–1214. DOI: `10.1364/OL.38.001212`.

4 Publication: Model-Driven 3-D Regularisation for Robust Segmentation of the Refractive Corneal Surfaces in Spiral OCT Scans

Proper segmentation of the cornea in OCT scans is a prerequisite for robust and accurate keratometry and topography by OCT. Common methods are limited to the segmentation of B-scans. We present a method for the model-based segmentation of the cornea, enabling the segmentation of scans that are acquired by two-dimensional scan patterns like spirals.

Publication We presented our work at the *4th MICCAI Workshop on Ophthalmic Medical Image Analysis (OMIA4)* in conjunction with the *20th International Conference on Medical Image Computing and Computer-Assisted Intervention (MICCAI)*, September 2017, in Quebec City, Quebec, Canada. It was published as part of the workshop proceedings [1].

We present the work as published, with minor changes in the layout. We refer to Section 7 for the discussion of the methods considering the latest findings.

Reference

[1] Joerg Wagner, Simon Pezold, and Philippe C Cattin. "Model-Driven 3-D Regularisation for Robust Segmentation of the Refractive Corneal Surfaces in Spiral OCT Scans". In: *4th MICCAI Workshop on Ophthalmic Medical Image Analysis* (2017).

Abstract

Measuring the cornea's anterior and posterior refractive surface is essential for corneal topography, used for diagnostics and the planning of surgeries. Corneal topography by Optical Coherence Tomography (OCT) relies on proper segmentation. Common segmentation methods are limited to specific, B-scan-based scan patterns and fail when applied to data acquired by recently proposed spiral scan trajectories. We propose a novel method for the segmentation of the anterior and posterior refractive surface in scans acquired by 2-D scan trajectories – including but not limited to spirals. Key feature is a model-driven, three-dimensional regularisation of the region of interest, slope and curvature. The regularisation is integrated into a graph-based segmentation with feature-directed smoothing and incremental segmentation. We parameterise the segmentation based on test surface measurements and evaluate its performance by means of 18 *in vivo* measurements acquired by spiral and radial scanning. The comparison with expert segmentations shows successful segmentation of the refractive corneal surfaces.

4.1 Introduction

Optical Coherence Tomography (OCT) is an emerging modality in ophthalmology – including measurement of the cornea. Although the cornea consists of multiple layers, refraction mainly occurs at the anterior and posterior surface. Correct three-dimensional delineation of the anterior and posterior corneal surfaces is therefore crucial for determining the corneal refractive power and the generation of corneal topography maps, used for diagnostics and surgical planning. For corneal measurement by OCT, the cornea is usually scanned by scan patterns consisting of multiple straight scans (B-scans). Raster patterns consist of parallel B-scans. Radial scan patterns consist of meridional B-scans rotated around the apex of the eye and are commonly used for corneal topography [1]. Recently, Wagner *et al.* [2] proposed a spiral scan pattern for corneal topography with reduced susceptibility to disturbances caused by eye blinking or abrupt movements. However, the appearance of the cornea in spiral scans is different and more variable (*cf.* Fig. 4.1), e.g. it varies with the relative position of the eye. This asks for new, more versatile segmentation and regularisation methods.

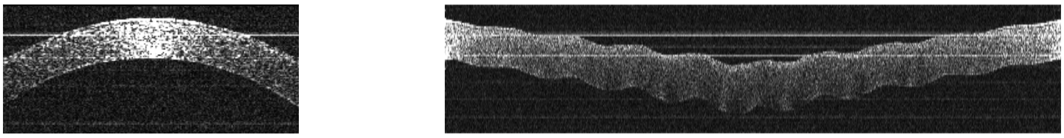
(a) (b)

Figure 4.1. (a) A typical radial B-scan. (b) One eighth (one cycle) of a spiral scan where the center of the scan pattern is aligned to the apex of the eye.

Common methods are optimised for the segmentation of classical B-scans – using active contours or graph theory. To overcome the typically low signal-to-noise ratio (SNR) of OCT images, 2-D regularisation schemes are applied. Yazdanpanah *et al.* [3] add 2-D shape and smoothness terms to their active contour approach. Williams *et al.* [4] use graph cut with 2-D curvature and shape terms. LaRocca *et al.* [5] use a two step process for segmenting corneal layers in radial B-scans. They restrict the search region by parabolic extrapolation from the central high SNR area into the lateral low SNR areas. Recently, Williams *et al.* [6] added a 2-D shape prior to their shortest path method, resulting in more accurate segmentation compared to level set and graph cut methods. Fu *et al.* [7] used graph-search to find markers for a later segmentation by a fourth order.

These methods are by design inappropriate for the segmentation of images obtained by spiral scan patterns. We present a model-driven 3-D regularisation for robust graph-based segmentation of the anterior and posterior refractive surface in scans from 2-D scan trajectories – including but not limited to spirals. Apart from the novel regularisation, the graph-based segmentation features intrinsic, feature directed smoothing for enhanced robustness to noise. Further, we developed an incremental segmentation scheme that enables the processing of long scans (as obtained by spiral scanning) on systems with limited memory.

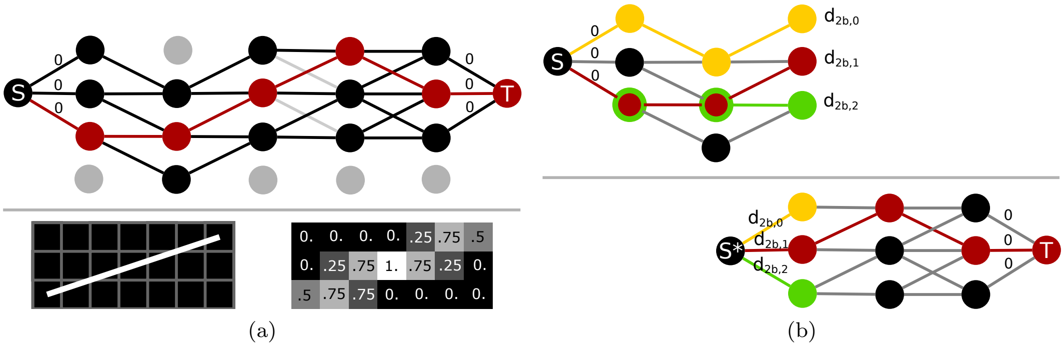

0.	0.	0.	0.	.25	.75	.5
0.	.25	.75	1.	.75	.25	0.
.5	.75	.75	0.	0.	0.	0.

(a) (b)

Figure 4.2. (a) The graph structure (top) with source (S) and target (T) nodes and the shortest path (red), while gray colour indicates nodes and edges outside the ROI or slope limits. An ideal edge (bottom, left) and the resulting kernel for edge weight calculation (bottom, right). (b) Piecewise segmentation scheme. The shortest distances ($d_{2b,i}$) to the last nodal A-scan of the first frame graph (top) are used as weight to connect the start node (S*) for the next frame (bottom).

4.2 Methods

4.2.1 Graph-Based Segmentation

Although the regularisation is our main contribution, we first describe the basic segmentation method. Because graph-search methods performed best in recent work [6], we convert the segmentation into a shortest path problem on a weighted directed graph. The nodes represent individual image pixels. Contrary to the state of the art, we only assign nodes to every b^{th} A-scan and introduce edges that span the A-scans lying in between, where edge length b is an integer greater than one. We will refer to A-scans with assigned nodes as *nodal A-scans*. The edge weights are calculated from the intensities of pixels lying on a straight line between their start and end pixel, which is done by means of kernel convolution (see Fig. 4.2a). This leads to a piecewise linear segmentation with averaging in edge direction. The averaging results in feature-directed smoothing and enhances the robustness to noise. Because the intensity of a nodal pixel is used twice – for incoming and outgoing edge weights – these pixels are weighted half. To ensure an unrestricted start and end, we connect a source and a target node by zero weight edges with all the nodes from the first and last nodal A-scan, respectively.

Incremental Segmentation

We developed an incremental scheme to solve the global graph search problem. With this scheme, neither the complete scan nor the complete graph has to be in memory at once. We divide the scan image into frames containing $a\,b+1$ A-scans, where b is the edge length and a an integer greater than one. Therefore, each frame starts and ends with a nodal A-scan. Because the last A-scan of a frame is the first A-scan of the following frame, the frames overlap by one A-scan. Thus, the first frame contains the A-scan indices 0 up to $a\,b$ and the second frame contains $a\,b$ to $2\,a\,b$. The procedure consists of the following steps (*cf.* Fig. 4.2b): (1) Generate the graph for the first frame, (2) determine the shortest path $d_{ab,j}$ to all nodes in the last A-scan, (3) generate the graph for the next frame using the path distances $d_{ab,j}$ to connect the new start node, (4) repeat steps (2) and (3). The shortest path to the target is then put together from the shortest paths determined in step (2). To save memory, the single frames are read in and preprocessed on demand for steps (2) and (3).

Preprocessing

After applying the fast Fourier transform to the spectral OCT scans, subtracting the background scan and taking the logarithm (of base 10), a specific preprocessing is performed for each feature to segment (see Sec. 4.2.2). The given filter widths are specific for the used scan system (see Sec. 4.2.3). For the *stroma*, Gaussian smoothing (σ=7 px) and box filtering (width=28 px) in scan direction and 2D sub-scaling by the factor 7 is performed. For the *anterior surface* and *posterior surface*, filtering in scan direction with the negative and positive first derivative of a Gaussian (σ=4 px) is performed, respectively.

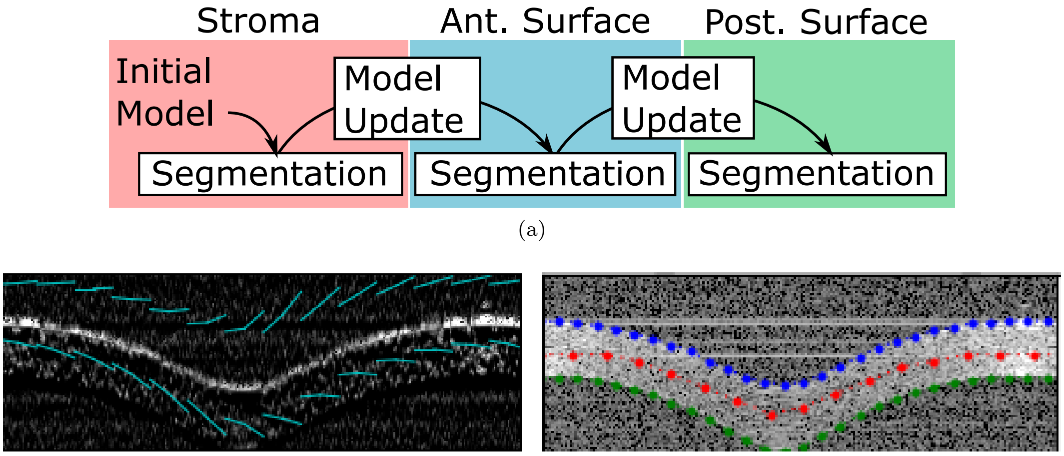

(a)

(b)

(c)

Figure 4.3. (a) Segmentation procedure. (b) Section of a scan, preprocessed for the segmentation of the anterior surface, with the regularisation limits for ROI, slope and curvature (cyan). (c) Original scan section with the resulting segmentations.

4.2.2 Regularisation

Based on a three-dimensional model, the region of interest (ROI), slope and curvature are selectively limited. To increase robustness, we perform a stroma segmentation prior to the segmentation of the anterior and posterior corneal surfaces (see Fig. 5.4). The regularisation model is updated between the segmentations. Figure 5.8 shows the positive effect of this regularisation scheme, especially for segmentation of the posterior corneal surface.

Regularisation Model

We used Zernike polynomials as the basis for our regularisation model because they are state of the art for the description of optical surfaces [2]. Our model consists of a 6^{th}-order Zernike surface, defined by its radius and coefficients $c_{n,m}$, and tolerances $t_{n,m}$ assigned to the coefficients (all in millimeters), where n and m indicate the radial and azimuthal degree of the Zernike polynomials Z_n^m, respectively. For the initial model, we constructed a Zernike surface that approximates a sphere with radius of 7.8 mm – the shape and size of a typical cornea. A relative coefficients tolerance $t_{n,m} = 0.2 \cdot c_{n,m}$ was applied, except for the offset tolerance which was set to $t_{0,0} = 0.5$. Thus, the operator has to adjust the distance between OCT system and subject in advance with an accuracy of ± 0.5 mm. For the model updates, the Zernike surfaces are constructed based on the previous segmentation as described in [2]. We use the coefficients' standard errors $s_{n,m}$, measures for the confidence in the reconstruction [2], to calculate the tolerances of the coefficients by $t_{n,m} = 4 \cdot s_{n,m}$.

The reconstructed surface is shifted by redefining the offset coefficient $c_{0,0} := c_{0,0} + dz$, where dz is the estimated distance from the previous surface. The corresponding coefficient tolerance is modified as $t_{0,0} := t_{0,0} + \Delta dz$, where Δdz is the tolerance of the surface position. Assuming a corneal thickness of 0.8 ± 0.5 mm and a corneal refractive index of $n_c = 1.38$, we use a distance shift for the anterior surface of $dz_{sa} = 0.4 \cdot 1.38$ with a tolerance of $\Delta dz_{sa} = 0.25 \cdot 1.38$ and a shift for the posterior surface of $dz_{ap} = 0.8 \cdot 1.38$ with a tolerance of $\Delta dz_{ap} = 0.5 \cdot 1.38$.

Implementation

To restrict the ROI, nodes are generated only for pixels lying in an estimation band for the depth $z_E(i) \pm z_M(i)$. The depth $z_E(i)$ is estimated by sampling the model surface at the scan position i. The margin $z_M(i)$ is determined based on the coefficients tolerances $t_{n,m}$. Because the Zernike polynomials Z_n^m are orthogonal, the margin from the individual tolerance Zernike polynomials $z_M^{n,m}(i) = \text{abs}(t_{n,m} \cdot Z_n^m(x_i, y_i))$ are added to obtain the total margin $z_M(i) = \sum z_M^{n,m}$. To restrict the slope, two nodes at scan positions i_1 and i_2 are only connected when the slope $\Delta z(i_1, i_2)$ is in the slope estimation band $\Delta z_E(i_1, i_2) \pm \Delta z_M(i_1, i_2)$. The slope $\Delta z_E(i_1, i_2)$ is estimated by sampling the model surface at the scan positions and calculating the depth difference $\Delta z_E(i_1, i_2) = Z(x_{i2}, y_{i2}) - Z(x_{i1}, y_{i1})$. For calculating $\Delta z_M(i_1, i_2)$, the slope margins of the tolerance polynomials are determined and added analogously. The curvature is restricted while solving the shortest path problem with an adapted version of Dijkstra's algorithm: The curvature is restricted by considering only the nodes that result in a discrete curvature that is in the allowed range. The curvature at a certain scan point i is defined by $c_i = z(i-1) - 2\,z(i) + z(i+1)$. The estimated curvature is calculated from the model surface by $c_E = z_E(i-1) - 2\,z_E(i) + z_E(i-1)$. The margin c_M is determined in analogy with the position and slope margin.

4.2.3 Evaluation

Scan Patterns and Setup

For the evaluation of the method, we used two scan patterns with different 2-D scan trajectories: a spiral scan pattern (Fig. 4.4a) with 32768 points and a radial scan pattern 5920 points (Fig. 4.4b) that includes turning loops between B-scans. We implemented the segmentation in Python 2.7, using Numpy and NetworkX, and used a custom swept-source OCT system at 1060 nm featuring telecentric scanning and a sweep rate of 30 kHz. Bandwidth-limited full-width at half maximum axial resolution of the system is 40 µm. Segmentation is based on data interpolated to 12 µm axial pixel dimension.

Parameter Optimisation

Edge length b is a crucial parameter. A short edge results in low averaging and high susceptibility to noise. On the other hand, a long edge is expected to bias the segmentation because the piecewise linear approximation is not adequate anymore. Thus, we optimised the edge length by means of test surface measurements with both scan patterns. We used three test surfaces with different shapes: a sphere with a radius of 6.4 mm, a sphere with a radius of 8.8 mm, and a torus with radii of 7.6 mm and 8.0 mm. We performed a torus fit on the points obtained by the individual segmentations and used the RMS of the fit error to find the trade-off between high robustness to noise and accuracy.

In Vivo Evaluation

For the *in vivo* evaluation, we used an edge length of 20 for the segmentation of the corneal surfaces and an edge length of 10 for the sub-scaled stroma segmentation. We used a edge length at the lower end of the optimal range (see parameter optimisation results) because the test surfaces only represent normal eyes and idealized astigmatism. The method was evaluated by comparing to expert segmentations. Nine different eyes from nine healthy volunteers were measured with both scan patterns. The expert manually marked the pixel-position of the anterior and posterior cornea surface in 10 randomly selected A-scans (*cf.* Fig. 5.8). This procedure was done a second time for the same A-scans, by the same expert. For each of the 180 A-scans, we calculated the differences between the piece-wise linear interpolated automatic segmentation z_S and the expert segmentation z_{E1} by $dz_{SE1} = z_S - z_{E1}$ as well as the differences between the two expert segmentations $dz_{E12} = z_{E1} - z_{E2}$.

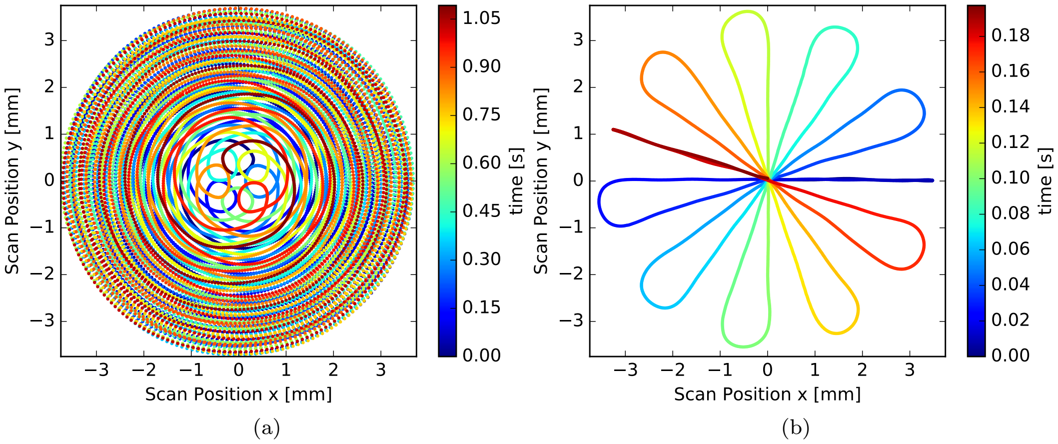

(a) (b)

Figure 4.4. (a) The spiral scan pattern and (b) the radial scan pattern.

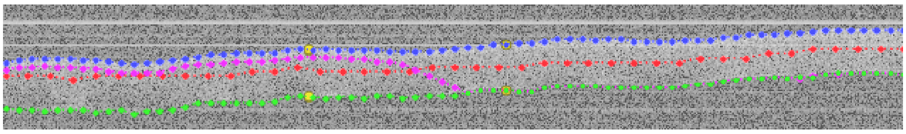

Figure 4.5. Section of a spiral *in vivo* scan. The segmented cornea anterior (blue) and posterior (green) corneal surface. The stroma segmentation is shown in red. As comparison, the unregularised segmentation of the posterior surface is shown in magenta. Expert segmentations are shown in yellow.

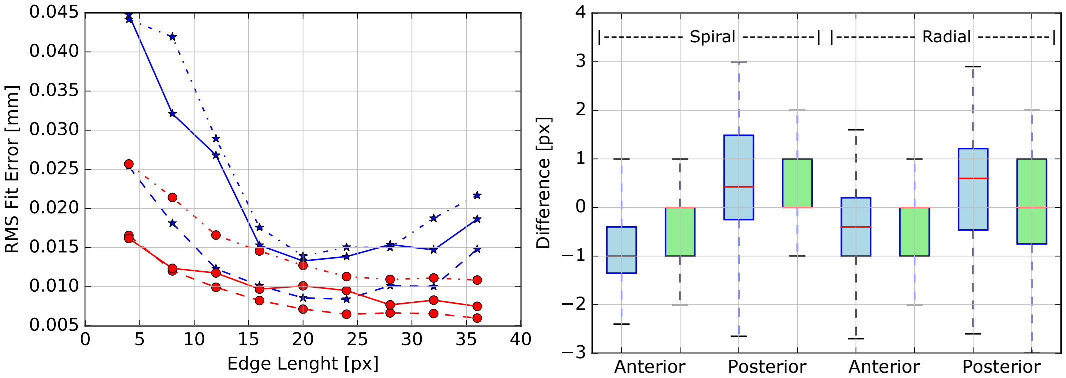

(a)

(b)

Figure 4.6. (a) Optimisation curve of the edge width for the scan patterns (spiral: red, radial: blue) and test surfaces (small sphere: dashed, big sphere: dash-dot, torus: solid). (b) *In vivo* differences between automatic segmentation and expert segmentation d_{SE1} (blue) and between the expert segmentations d_{E12} (green).

4.3 Results

Parameter Optimisation

The test surface measurements confirm the positive effect of the feature-directed smoothing introduced by the A-scan-spanning edges. Figure 4.6a shows minimal fitting error for an edge width between 16 and 28 for the radial scan pattern. For the spiral scan pattern, the error still seems to decrease when increasing the edge length above 24, albeit being close to convergence. This can be explained by the fact that the radial pattern scans along the maximal surface gradient whereas the spiral pattern scans nearly along the minimal surface gradient.

In-Vivo Evaluation

Figure 4.6b shows the comparison with expert segmentations. For the difference to the expert segmentation dz_{SE1} we removed two outliers (-72 px and -66 px), caused by exceptionally low SNR in one radial scan. This results in a mean difference $\bar{dz}_{SE1}$ of -0.73 ± 1.06 px (mean ± SD) for the anterior surface and -0.13 ± 2.91 px for the posterior surface, over both scan patterns. The mean difference between expert segmentations $\bar{dz}_{E12}$ is -0.31 ± 0.87 px for the anterior surface and -0.35 ± 2.85 px for the posterior surface.

4.4 Discussion

Motivated by the recently proposed spiral scan pattern and the limitations of current segmentation methods, we introduce a novel 3-D regularised segmentation for the anterior and posterior corneal surface in scans acquired by 2-D scan trajectories like spirals. The *in vivo* comparison with expert segmentations shows successful segmentation of the anterior and posterior corneal surfaces. Both differences, between our method and expert segmentations and between the expert segmentations, are within ±3 px. With the pixel resolution of 12 µm, this corresponds to a spatial range of ±36 µm, which is less than the full-width at half maximum axial resolution (40 µm) of the OCT system. This indicates segmentation of the accurate surfaces. Because our method works for two contrary 2-D scan trajectories, one scanning along the maximal surface gradient and one scanning along the minimal surface gradient, we suppose that the method is suited for various 2-D scan trajectories – assuming continuous scanning.

We want to point out that comparison with common methods is not possible or would be unfair because they are not able to segment scans from 2-D scan trajectories by design. The limited system resolution, the variable angle of the incident laser beam relative to the interface and noise lead to a diffuse interface signal which makes the exact identification of the interface imprecise – even for an expert. Due to this lack of a quantitative gold standard, quantitative comparison below the level of system resolution is inappropriate. However, we believe that expert segmentation is gold standard to show successful segmentation of the surfaces in a qualitative manner. We did this by showing that the segmentation difference is below the axial resolution the OCT system. Regarding our future work, we believe that quantitative verification of the segmentation is only possible in the course of a comprehensive validation that involves the whole pipeline for OCT-based corneal topography and comparison with established topographers on normal and pathologic eyes.

We want to emphasise that the key of the method lies in the novel model-driven 3-D regularisation that guides the graph-based segmentation. This 3-D regularisation enables robust segmentation of scans from 2-D scan trajectories. By using hard restriction margins for ROI, slope and curvature, we aim to minimise regularisation bias. Others [3, 4] use continuous penalty which potentially introduces bias by pulling the solution towards a prior, *e.g.* by adding curvature and shape terms to an energy minimisation. In contrast to established methods, the presented regularisation can be easily adapted, *e.g.* unreliable lateral-horizontal eye alignment can be addressed by adapting the initial regularisation model – in this case by increasing the tolerances of the tilt coefficient $t_{1,1}$ [8].

References

[1] Ryan P McNabb et al. “Distributed scanning volumetric SDOCT for motion corrected corneal biometry”. In: *Biomedical Optics Express* 3.9 (2012), pp. 2050–2065.

[2] Joerg Wagner, David Goldblum, and Philippe C Cattin. “Golden angle based scanning for robust corneal topography with OCT”. In: *Biomedical Optics Express* 8.2 (2017), pp. 475–483.

[3] Azadeh Yazdanpanah et al. “Segmentation of intra-retinal layers from optical coherence tomography images using an active contour approach”. In: *IEEE Transactions on Medical Imaging* 30.2 (2011), pp. 484–496.

[4] Dominic Williams et al. “Fast segmentation of anterior segment optical coherence tomography images using graph cut”. In: *Eye and Vision* 2.1 (2015).

[5] Francesco LaRocca et al. “Robust automatic segmentation of corneal layer boundaries in SDOCT images using graph theory and dynamic programming”. In: *Biomedical Optics Express* 2.6 (2011), pp. 1524–1538.

[6] Dominic Williams et al. “Reconstruction of 3D surface maps from anterior segment optical coherence tomography images using graph theory and genetic algorithms”. In: *Biomedical Signal Processing and Control* 25 (2016), pp. 91–98.

[7] Huazhu Fu et al. “Segmentation and Quantification for Angle-Closure Glaucoma Assessment in Anterior Segment OCT”. In: *IEEE Transactions on Medical Imaging* (2017).

[8] Boy Braaf et al. “Calculating angle lambda (λ) using zernike tilt measurements in specular reflection corneal topography”. In: *Journal of Optometry* 2.4 (2009), pp. 207–214.

Appendix

Used Graph-Search Algorithm

Algorithm 1 was used to find a path that fulfills the curvature restrictions. Although the algorithm does not provide the optimal solution in every case, it provided good results (see manuscript).

Algorithm 1 Dijkstra's algorithm with curvature restriction

```
function Dijkstra(Graph, source)
    create node set $Q$
    for each node $v$ in Graph do
        distances[$v$] $\leftarrow$ INFINITY
        previous[$v$] $\leftarrow$ UNDEFINED
        add $v$ to $Q$
    dist[$source$] $\leftarrow 0$
    while $Q$ is not empty do
        $u \leftarrow$ node in $Q$ with min distances[$u$]
        $t \leftarrow$ previous[$u$]
        remove $u$ from $Q$
        for each neighbor $v$ of $u$ do
            if curvature($t$,$u$,$v$) in range then
                $alt \leftarrow$ distances[$u$] + length($u, v$)
                if $alt <$ distances[$v$] then
                    distances[$v$] $\leftarrow alt$
                    previous[$v$] $\leftarrow u$
    return distances[], previous[]
```

Alternative Graph-Search Algorithm

Algorithms 2 and 3 potentially provide the optimal solution for the shortest path problem with restricted curvature (the optimality of this algorithm is still to proof). This algorithm is considerable slower than the non-optimal algorithm above.

Algorithm 2 Alternative Dijkstra's algorithm with curvature restriction

```
function DIJKSTRA(Graph, source)
    create node set $Q$
    for each node $v$ in Graph do
        distances[$v$] $\leftarrow$ INFINITY
        previous[$v$] $\leftarrow$ UNDEFINED
        alternativePrevious[$v$] $\leftarrow$ []
        prePrevious[$v$] $\leftarrow$ UNDEFINED
        add $v$ to $Q$
    dist[$source$] $\leftarrow 0$
    while $Q$ is not empty do
        $u \leftarrow$ node in $Q$ with min distances[$u$]
        remove $u$ from $Q$
        for each neighbor $v$ of $u$ if $u$ in alternativePrevious[v] or is previous[v] do
            $alt \leftarrow$ distances[$u$] + length($u, v$)
            if $alt$ >< distances then
                distances[$v$] $\leftarrow alt$
                previous[$v$] $\leftarrow u$
            for each neigbor w of v if curvature($t$,$u$,$v$) in range do
                $alt2 \leftarrow alt$ + length($v, w$)
                if $alt2 <$ distances[$w$] then
                    distances[$w$] $\leftarrow alt2$[]
                    alternativePrevious[$w$]+ = [previous[$w$]]
                    previous[$v$] $\leftarrow v$
                    prePrevious[$v$] $\leftarrow u$
                else
                    alternativePrevious[$w$]+ = [$v$]
    return distances[], previous[], prePrevious[]
```

Algorithm 3 Path Generation for Alternative Dijkstra's algorithm

```
function GETPATH(previous[], preprevious[], endNode)
    negPath $\leftarrow$ [endNode]
    node $\leftarrow$ endNode
    repeat
        if previous[previous[node]] equals prePrevious[node] then
            node $\leftarrow$ previous[node]
            negPath+ = [node]
        else
            node $\leftarrow$ prePrevious[node]
            negPath+ = [previous[node], prePrevious[node]]
    until previous[node] is not defined
    return reverse of negPath
```

5 Publication: Model-Based Motion Compensation for Corneal Topography by Optical Coherence Tomography (OCT)

In our first publication, we introduced a scan pattern addressing the problem of patient induced abrupt distortions. In this paper, we address yet another, more crucial limitation of OCT-based corneal topography – so-called fixational eye motion during measurement. We present, to our knowledge, the first continuous 3-D motion compensation of ocular motion for OCT measurements of the anterior chamber. Further, we introduce novel methods for scanning and reconstruction, resulting in a complete pipeline for corneal topography by OCT. We present a thorough *in vivo* comparison of the OCT-based corneal topography with established Placido Disc (Atlas, Carl Zeiss Meditec) and Scheimpflug (Pentacam, Oculus) topographers. The results underline the necessity and efficiency of our motion compensation. The comparison of the radial curvature with the reference topographers shows similar performance in terms of repeatability and equivalence.

Publication The paper was published in the *OSA Continuum* of the *Optical Society of America* on July 15, 2020 [1].

We present the work as published, with minor changes in the layout. We refer to Section 7 for the discussion of the methods considering the latest findings. We incorporated the major principles of this publication into a patent application (EP 3 662 812 A1, see Appendix).

Reference

[1] Joerg Wagner et al. "Model-based motion compensation for corneal topography by optical coherence tomography". In: *OSA Continuum* 3.7 (2020), pp. 1967–1987.

Abstract

Corneal topography is an essential tool in ophthalmology, in particular for surgical planning and diagnostics. Optical Coherence Tomography (OCT) enables cross-sectional or volumetric imaging with high resolution. It is, however, not widely used for corneal topography. A major reason for this is that conventional beam-scanning OCT is susceptible to eye motion compared to established modalities, that measure corneal shape in a single shot. To overcome this limitation, we propose a novel pipeline for motion-compensated OCT-based corneal topography. The pipeline includes three main features: (1) continuous, two-dimensional scanning, (2) the three-dimensional continuous motion compensation in postprocessing and (3) regularised Zernike reconstruction.

First, we evaluated our method on an eye phantom that is moved to mimic typical eye motion. The proposed motion compensation was able to determine and correct the movements of the phantom. Second, we performed an *in vivo* study on 48 eyes, measuring each eye twice with our OCT-based topography, Placido disc topography (Atlas 9000, Carl Zeiss Meditec), and Scheimpflug (Pentacam, Oculus) topography. We then compared the performance of the OCT-based topography to the reference topographies in terms of repeatability and equivalence. The results confirm the necessity and efficiency of the presented motion compensation and validate the proposed methods for scanning and reconstruction.

5.1 Introduction

Ophthalmologists rely on accurate corneal topography for surgical planning and diagnostics, *e.g.* to detect pathological deformations, such as keratoconus, at an early stage. Corneal topography provides two-dimensional maps of the cornea's curvature and refractive power. Placido disc reflection, scanning slit and Scheimpflug photography are established modalities for corneal topography. While Optical Coherence Tomography (OCT) is commonly used for cross-sectional or volumetric imaging with high resolution, its use for corneal topography is still limited. In contrast to conventional modalities, OCT potentially enables a simultaneous measurement of all optically relevant structures of the eye, including, but not limited to, corneal topography. Whereas traditional photography-based principles enable acquisition of 2-D or 3-D geometrical information of the cornea in an instant, beam-scanning OCT relies on the sequential gathering of one-dimensional axial depth profiles (A-scans) to obtain two-dimensional scans (B-scans) or volumetric scans. For OCT-based corneal topography, the cornea is scanned at discrete positions around the corneal vertex. This sequential scanning takes time and makes the measurement susceptible to eye motion. The acquisition time could be minimised by using high-speed OCT systems, yet these systems are costly and the high acquisition rate sacrifices signal quality. The need for lateral scanning could be entirely removed by using parallel OCT instead of beam-scanning OCT, but these systems have other disadvantages, such as the need for mechanical depth scanning or more complex optical setups [1, 2]. Real-time tracking of the corneal position during acquisition is another rather hardware-demanding and expensive approach. Therefore, common approaches rely on tailored scanning schemes and algorithms to enable motion compensation after the acquisition.

The feasibility of motion compensation is strongly linked to the used scan pattern. Recently, Wagner *et al.* [3] proposed golden angle based spiral scanning for robust corneal tomography. This scanning scheme enables the elimination of abrupt and large movement from the measurement without sacrificing the reliability of the reconstruction. However, the problem of continuous motion during scanning was not addressed. Scan patterns more commonly used for corneal topography consist of several meridional B-scans centred around a common central point which is usually aligned to the apex of the cornea [4, 5, 6, 7]. These so-called radial scan patterns simplify axial motion compensation because all meridional scans share the apex as a common point, allowing an alignment of the individual B-scans. McNabb *et al.* [8, 9] use a special radial scan pattern for their Distributed Scanning OCT method, consisting of 20 meridional B-scans with 500 A-scans each. Spatially adjacent A-scans are not gathered sequentially in time but distributed over five sub-sampled passages. Thus, the scan pattern consists of five connected scans with 20 radial B-scans containing 100 A-scans. Each B-scan takes 10 ms and is assumed to be free of motion. Motion-compensated meridional B-scans are then reconstructed from the five sub-sampled B-scans along the given meridian. Raster scanning is another, more traditional scanning type. Although raster scanning is not commonly used for corneal topography, motion compensation methods are applied to generate distortion-free volumes of the retina or anterior segment. In classical raster scanning, several parallel B-scans are gathered, covering a rectangular area. This results in a fast and a slow scan axis, one perpendicular to the other. While B-scans along the fast scan axis are considered motion free [10], B-scans along the slow axis are prone to motion. Although visually appealing volumes can be created by aligning the fast-axis B-scans to each other, geometrical information along the slow scan axis will be lost. To overcome this problem, Kraus *et al.* [11] gathered additional B-scans along the slow scan axis to align the fast-axis B-scans to these additional B-scans. Recently, Chen *et al.* [12] presented a Lissajous scan pattern for three-dimensional imaging of the retina. Because the scan pattern frequently overlaps with itself, they were able to compensate motion in three dimensions.

We present a novel pipeline for motion-compensated corneal topography by OCT, including the following steps (see Fig. 5.1): (1) Scanning of the cornea with a tailored scan pattern, (2) chunk-wise segmentation of the anterior corneal interface, (3) continuous motion compensation in three dimensions, (4) outlier removal, (5) regularised Zernike reconstruction and (6) generation of the axial curvature map. Our scan pattern provides fast coverage and a high number of intersections to aid motion compensation. The motion compensation features continuous, model-based motion detection in three dimensions with high temporal resolution. In contrast to common methods [8, 11, 12], no part of the scan is assumed to be motion-free. Instead, our method features continuous motion compensation in three dimensions. We model the motion by a piecewise polynomial spline and formulate an optimisation problem to determine the motion parameters together with a parametric description of the anterior corneal surface. The regularisation of the reconstruction addresses instabilities in the curvature space of standard Zernike reconstruction.

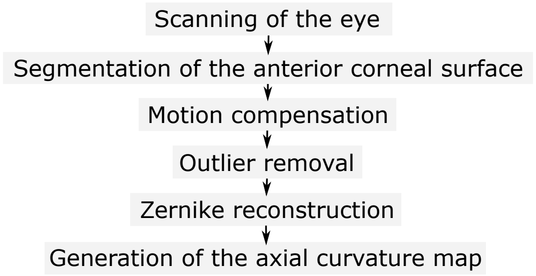

Figure 5.1. The different steps in our pipeline.

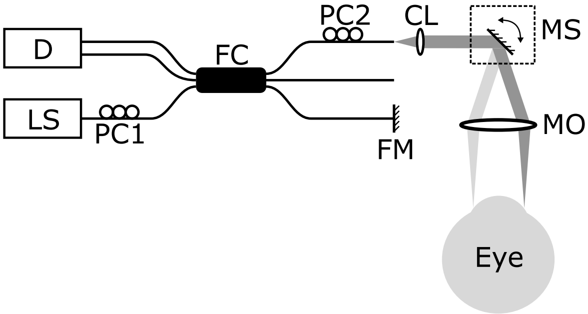

Figure 5.2. Schematic of the swept-source OCT system with its components. LS: Laser Source; PC1, PC2: Polarisation controllers; FC: Fibre coupler; CL: Collimating lens; MS: 2-D MEMS beam scanner; MO: Measurement objective; D: Detector; FM: Fibre mirror.

5.2 Methods

5.2.1 Scan system

We use a prototype swept-source OCT system optimised for simultaneous OCT imaging of the anterior eye segment and measurement of axial eye length in a single scan range. Figure 5.2 shows a schematic of the system with its main components. The system employs a telecentric scan geometry. To achieve sufficient collection efficiency over the entire eye length, we use a small numerical aperture of approximately NA ≈ 0.015. The focal plane is 5 mm behind the corneal vertex (neglecting the refractive effect of the eye). As a result, the lateral resolution at the anterior cornea is approximately 80 µm (full width at half maximum).

The laser source (LC, Axsun Technologies) sweep is centred at 1060 nm with a sweep range of 30 nm and a sweep rate of 30 kHz. The coherence length of the laser is 75 mm.

We comply with the requirements specified in ISO 15004-2:2007 (Group 2) [13] to limit the optical power. With a sample arm power of 1.9 mW, the OCT system has a sensitivity of 104.4 dB at the focal plane, 10 mm from zero delay. The total axial measurement range is 50 mm in air, and the axial resolution is 40 µm in air (full width at half maximum). We employ a 2D MEMS scanner (MS, Hamamatsu Photonics) for lateral scanning. Scan patterns with reduced bandwidth are used to avoid excitation of MEMS resonances around 500 Hz and 1 kHz. Since the scanner is operated in open-loop (without position encoders), careful calibration of the scanner control signal and characterisation of the resulting scan positions are required, as described in the following sections.

5.2.2 Scan pattern

As we mentioned in the introduction, it is common to use intersecting scan patterns to enable motion compensation: Additional B-scans along the slow axis of raster scans are used to align the B-scans to match at the intersections. Radial scan patterns facilitate motion compensation because the individual B-scans intersect at the vertex. The distributed scan pattern of McNabb *et al.* increases temporal and spatial linkage by gathering spatially adjacent scans distributed over five sub-sampled passages – also to enable motion compensation. The same principle applies to the Lissajous scan pattern used by Chen *et al.* [12].

We developed a new scan pattern that combines fast coverage with a high number of intersections while keeping the demands on the dynamics of the scanner low. The high number of intersections results in high temporal and spatial linkage in the scan. Because of this linkage, motion leads to apparent inconsistencies in the measurement, which enables assessment of the motion. The scan pattern trajectory is defined as

$$P_{\mathrm{SP}}(t) = \begin{pmatrix} x_{\mathrm{SP}}(t) \\ y_{\mathrm{SP}}(t) \end{pmatrix} = R_{\mathrm{SP}} \sin(a\,\omega\,t) \begin{pmatrix} \sin(b\,\omega\,t) \\ \cos(b\,\omega\,t) \end{pmatrix} , \tag{5.1}$$

where $R_{\mathrm{SP}} = 4\,\mathrm{mm}$ is the radius of the scan pattern and $\omega = 2\,\pi/T$ is the angular base frequency with $T = 0.546\,\mathrm{s}$. Scalars $a = 16$ and $b = 33$ define the ratio between the frequencies. This parametrisation results in a trajectory that repeats every 0.546 s, with a spectrum consisting of only two frequencies $f_{1,2} = (b \pm a)/T = 66.4\,\mathrm{Hz} \pm 29.3\,\mathrm{Hz}$. Sampling with 30 kHz results in a scan pattern of 16384 scan points. Figure 5.3 shows the scan pattern with the corresponding projections on the scanner axes. As can be seen from Fig. 5.3a, the scan point distribution is not uniform. As stated by Wagner *et al.* [3], a non-uniform scan point distribution lowers the numerical condition of Zernike reconstruction. At this point, we accept this drawback in favour of simple scanner control function with only two frequencies and fast coverage. The simple and smooth scanner control signal lowers the demands on the scanner dynamics, which is crucial for systems with limited bandwidth. The fast coverage potentially enables motion compensation with high temporal resolution. For each measurement, we acquire four consecutive frames, resulting in a scan of 65536 A-scans with a duration of 2.184 s.

We calibrated and characterised the scan pattern based on scans of a flat mirror as described in Section 5.2.3. The mirror is placed at a scan depth of 5 mm, which corresponds to the depth of the corneal vertex when scanning the cornea. The mean absolute deviation between the calibrated scan points and the specified scan points was 37 µm with a maximum of 73 µm. The deviation between specified scan points and calibrated scan points are mainly due to distortions caused by scan optics. However, the calibration method fully characterises the distorted pattern. The uncertainty of the calibrated scan points due to scan-to-scan variations and uncertainties of the calibration method is around 5 µm.

5.2.3 Calibration and characterisation of the scan pattern

For the applicability of the presented motion correction and reconstruction methods, the calibration method is not crucial, and other approaches can be used instead [14, 5]. However,

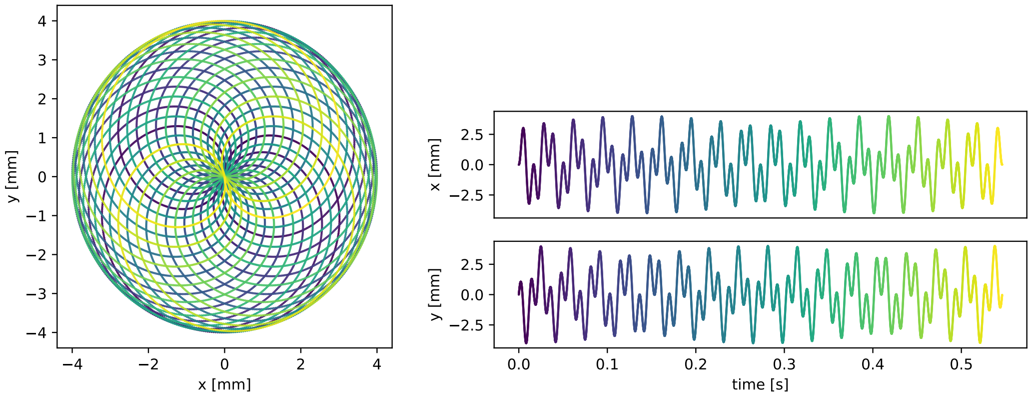

(a) (b)

Figure 5.3. (a) One frame of our scan pattern and (b) its projections onto the x and y axis. The color coding of the scan points indicate the point in time and is consistent between both subfigures.

since the accuracy of lateral beam positioning can limit the accuracy of corneal curvature measurement by OCT, the calibration and characterisation of the scan pattern require special attention, in particular in an open-loop scan system as used in this work. Since to our knowledge, the method applied here has not been discussed in literature before, we provide a brief outline. The method is based on a measurement of scan point coordinates by the OCT system itself ("interferometric scan position measurement") and consists of three steps: (1) Characterisation of the two-dimensional MEMS transfer function, (2) calculation of the scanner control signal for the scan pattern, (3) characterisation of the resulting scan positions.

Interferometric scan position measurement

We place a flat mirror on a gimbal mount in front of the system, centered with respect to the scan range of the beam scanner. To determine the lateral positions of a scan point, we measure the distance $z_{1,2,3,4}$ to the surface at that scan point by OCT, at four different tilt angles of the surface normal with respect to the beam axis, $(\Theta_x, \Theta_y)_{1,2,3,4} = (+\alpha, 0), (-\alpha, 0), (0, +\alpha), (0, -\alpha)$. The z-axis is parallel to the beam axis, and x and y are orthogonal to the beam axis and with respect to each other. The lateral position of the scan point is then given by $x = (z_2 - z_1)/(2\tan\alpha)$, and $y = (z_4 - z_3)/(2\tan\alpha)$. The axial offset of the scan point is given by $z_{\mathrm{ofs}} = (z_2 + z_1)/2$, or $z_{\mathrm{ofs}} = (z_4 + z_3)/2$. To take the frequency dependence of the scanner deflection into account, we measure a complete period of the scan pattern (points $i = 1 \ldots N$) for each mirror orientation and calculate the resulting trajectories for $x_{1\ldots N}$, $y_{1\ldots N}$, and $z_{\mathrm{ofs},1\ldots\mathrm{N}}$, based on the $4N$ distances $(z_{1,2,3,4})_{1\ldots N}$. The necessary precision of the distance measurement is achieved by Gaussian peak fitting to each A-scan.

Characterisation of the two-dimensional MEMS transfer function

For each scanner axis individually, we measure the beam trajectory resulting from a small amplitude sinusoidal input function using the method described in Section 5.2.3, yielding the response amplitudes in x and y-axis. This way, we can build a 2×2 matrix mapping a control signal $(c_1,\, c_2)$ to a beam position $(x,\, y)$ in the frequency domain. We repeat this for a set of frequencies between 25 and 300 Hz, and fit each matrix element by a third-order polynomial of the frequency, yielding the two-dimensional MEMS transfer function.

Calculation of the scanner control signal

We convert the scan pattern into the frequency domain using a Fourier transformation (the scan pattern is periodic). We then apply the inverted two-dimensional MEMS transfer function and convert the resulting control signal back into the time domain using an inverse Fourier transformation.

Characterisation of the resulting scan positions

We apply the control signal obtained according to Section 5.2.3 to the scanner, and characterise the resulting scan point coordinates according to Section 5.2.3. For the OCT system discussed in this work, the standard deviation of repeated characterisations of the scan pattern per point is typically 5 µm (averaged over all scan points). The mean absolute deviation between the characterised and specified scan point coordinates was 37 µm with a maximum of 73 µm. This deviation is mainly due to distortions caused by scan optics. It can be properly taken into account when evaluating corneal curvatures by using the characterised coordinates instead of the originally specified coordinates so that it does not harm the accuracy of the corneal topography measurement.

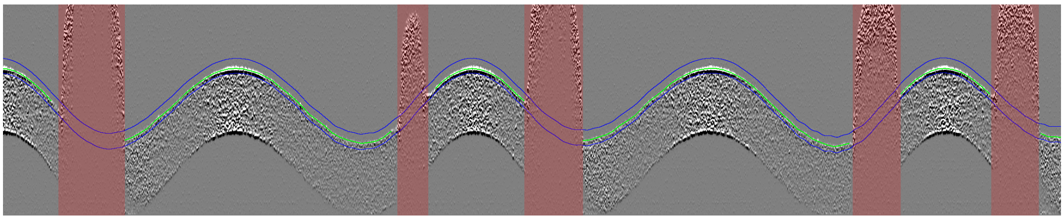

Figure 5.4. Section of the oversampled gradient image with masked out eye lid (reddish overlay), the ROI (blue) and the fine segmentation of the anterior corneal surface (green).

5.2.4 Segmentation

We use a graph-based segmentation, similar to the one described by Wagner *et al.* [15], to segment the anterior corneal surface in the scans. The key feature is a model-driven, three-dimensional regularisation of the region of interest (ROI), slope and curvature. For the segmentation, we divide each frame of 16384 A-scans into two chunks. Hence, we split the complete scan of four frames into eight chunks of 8192 A-scans each. For each chunk, the A-scans containing eyelid are identified and excluded from the segmentation (*cf.* Fig. 5.4). The automatic eyelid classification uses the centre of mass of the A-scan intensities (first moment of the A-scan vector divided by the sum of the A-scan vector) as the main classification feature. The anterior corneal surface is then segmented chunk-wise by using a regularisation model that is continuously updated between the chunks.

In general, we use the segmentation of each chunk to update the regularisation model for the segmentation of the next chunk. For the first chunk, we initially segment the corneal stroma using an initial model of the cornea for regularisation. Based on the stroma segmentation, the model for the segmentation of the anterior surface is generated. Wagner *et al.* [15] described the initial model, the preprocessing and the segmentation procedure in more detail. Each segmentation consists of a coarse and a fine segmentation. The coarse segmentation is used to create a refined model for the fine segmentation. It relies on the downsampled (by a factor of 4) gradient image, whereas the fine segmentation uses an oversampled (by a factor of 2) gradient image, providing a segmentation value for every 8th A-scan.

After the segmentation of the anterior corneal surface in a chunk, the segmentation is checked for plausibility. Implausible segmentation can be caused by blinking of the patient, saccades during the chunk or extensive motion. For the plausibility check, a 5th-order Zernike reconstruction is performed on the segmented points of the chunk, and the *mean coefficients standard error* [15] is used for classification. The threshold for classification was set to $2.5 \times 10^{-6}\,\mathrm{m}$. Please note that this threshold is only valid for the given chunk size and the expected number of segmented points. If classified as implausible, the segmentation of this chunk is dumped, and the regularisation model is not updated. In this case, the old regularisation model is used for the segmentation of the next chunk.

Although we did not explicitly implement detection of big saccades or extensive motion, the combination of the model-based ROI and exclusion of implausible chunks results in removal of chunks affected by big saccaded or extensive motion: If big saccades or extensive motion are present in a chunk, the cornea will be outside the ROI. This leads to segmentation in the noise, which further results in a high *mean coefficients standard error* and exclusion of the chunk. Chunks containing distortions not resulting in failed segmentation but with a negative effect on the reconstruction are removed during outlier removal (see Sec. 5.2.6).

Because the signal of the phantom is different from the signal of the cornea, we use a modified segmentation scheme for phantoms: First, no initial stroma segmentation is

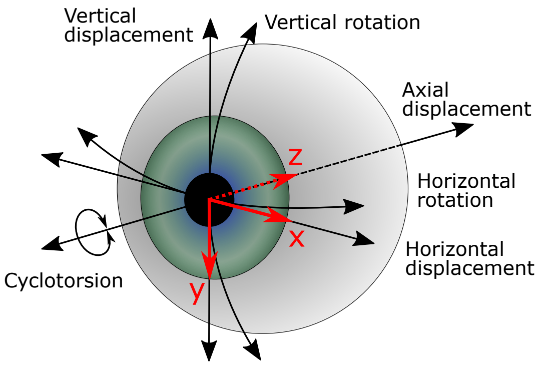

Figure 5.5. The movement of the eye and its axes.

performed. Instead, the phantom surface is segmented directly using the initial model. Second, the segmentation does not rely on a gradient image. Instead, we rely on the same preprocessing that was used for phantoms by Wagner *et al.* [15].

5.2.5 Motion compensation

Our motion compensation uses the segmented points to estimate and compensate motion-induced displacement in all three axes (see Fig. 5.5) simultaneously, while we assume the rotations to be negligible. We employ a continuous optimisation scheme to reproduce the position of the segmented points by Zernike polynomials and three-dimensional piecewise polynomial displacement. The optimisation, therefore, yields a polynomial description of the displacement in each chunk. The displacement is forced to be continuous and continuous in its first derivative between adjacent chunks by applying the corresponding regularisation.

Optimisation problem

The point cloud from the segmented anterior corneal surface is the input of the optimisation. For each segmented point, we have the coordinate $P_n = \begin{pmatrix} x_n & y_n & z_n \end{pmatrix}^T$ and the time t_n for $n = 0, 1, \ldots, N^t - 1$, where N^t is the total number of points. As for the segmentation, we split the measurement into $Z = 8$ intervals of equal duration, which results in 8 point chunks. Because the segmentation can have gaps due to removed eyelids, the number of points in the chunks varies. Empty point chunks, caused by implausible segmentation (*cf.* 5.2.4), are excluded from the following steps, resulting in $Z^* \leq Z$ valid point chunks. The piecewise polynomial displacement is defined by

$$f(t) = \begin{pmatrix} f_x(t) \\ f_y(t) \\ f_z(t) \end{pmatrix} = \sum_{i=0}^{Z^*-1} \mathrm{boxcar}_i(t) \begin{pmatrix} \alpha^x_{i\,0}\,1 + \alpha^x_{i\,1}\,(t - t_i^m)^1 + \ldots + \alpha^x_{i\,O_x}\,(t - t_i^m)^{O_x} \\ \alpha^y_{i\,0}\,1 + \alpha^y_{i\,1}\,(t - t_i^m)^1 + \ldots + \alpha^y_{i\,O_y}\,(t - t_i^m)^{O_y} \\ \alpha^z_{i\,0}\,1 + \alpha^z_{i\,1}\,(t - t_i^m)^1 + \ldots + \alpha^z_{i\,O_z}\,(t - t_i^m)^{O_z} \end{pmatrix}, \tag{5.2}$$

where t_i^m denotes the mean time of the points in chunk i, and α are the coefficients of the individual polynomials. The boxcar function $\mathrm{boxcar}_i(t)$ is 1 if t is inside the chunk interval i and 0 otherwise. $O_x = 6$, $O_y = 6$ and $O_z = 8$ are the degrees of the displacement polynomials in the corresponding axis. These degrees were determined empirically and offer a trade-off between their capability to model fast motion and the numerical stability of the motion compensation.

We determine the coefficients of the displacement polynomials by solving the linear least-squares problem

$$\min_{\beta,\,\alpha} \quad \left\| \begin{pmatrix} \mathbf{Z} & \mathbf{M} \\ \mathbf{0} & \mathbf{C} \end{pmatrix} \begin{pmatrix} \boldsymbol{\beta} \\ \boldsymbol{\alpha} \end{pmatrix} - \begin{pmatrix} \mathbf{z} \\ \mathbf{0} \end{pmatrix} \right\|_2^2 , \tag{5.3}$$

where $\boldsymbol{\beta}$ is a column vector with the Zernike coefficients and $\boldsymbol{\alpha}$ a column vector with the coefficients of the piecewise polynomial displacement. The columns of the matrix $\mathbf{Z}$ hold the Zernike polynomials sampled at the x,y-coordinates of the segmented points, while $\mathbf{z}$ represents the z-coordinates of the segmented points. Matrix $\mathbf{M}$ holds the polynomial basis functions for the displacement in each chunk and $\boldsymbol{\alpha}$ the corresponding coefficients:

$$\mathbf{M} = \begin{pmatrix} \mathbf{M}_0 & \mathbf{0} & \iddots & \mathbf{0} \\ \mathbf{0} & \mathbf{M}_1 & \iddots & \mathbf{0} \\ \ddots & \ddots & \ddots & \ddots \\ \mathbf{0} & \mathbf{0} & \iddots & \mathbf{M}_{Z^*-1} \end{pmatrix} , \tag{5.4}$$

$$\boldsymbol{\alpha} = \begin{pmatrix} \boldsymbol{\alpha}_0 & \boldsymbol{\alpha}_1 & \dots & \boldsymbol{\alpha}_{Z^*-1} \end{pmatrix}^T . \tag{5.5}$$

$\mathbf{M}_i$ includes the displacement basis functions in all three axes and $\boldsymbol{\alpha}_i$ the coefficients of the displacement polynomial in all three axes for the specific chunk i:

$$\mathbf{M}_i = \begin{pmatrix} \mathbf{M}_i^x & \mathbf{M}_i^y & \mathbf{M}_i^z \end{pmatrix} , \tag{5.6}$$

$$\boldsymbol{\alpha}_i = \begin{pmatrix} \boldsymbol{\alpha}_i^x & \boldsymbol{\alpha}_i^y & \boldsymbol{\alpha}_i^z \end{pmatrix}^T = \begin{pmatrix} \alpha^x_{i\,0} & \dots & \alpha^x_{i\,O_x} & \alpha^y_{i\,0} & \dots & \alpha^y_{i\,O_y} & \alpha^z_{i\,0} & \dots & \alpha^z_{i\,O_z} \end{pmatrix}^T . \tag{5.7}$$

The columns of $\mathbf{M}_i^x$, $\mathbf{M}_i^y$ and $\mathbf{M}_i^z$ represent the displacement basis functions in the corresponding direction. The displacement basis functions for the x- and y-direction are estimated based on an initial 6^{th}-order Zernike fit on the segmented point cloud. Each entry is determined by the partial derivative of the Zernike surface at the x,y-coordinate of the corresponding point n and order m:

$$\mathbf{M}^x_{i\,n,m} = \frac{d}{dx} Z(x_n, y_n) \times (t_n - T_i)^m , \tag{5.8}$$

$$\mathbf{M}^y_{i\,n,m} = \frac{d}{dy} Z(x_n, y_n) \times (t_n - T_i)^m . \tag{5.9}$$

For the z-direction this simplifies to

$$\mathbf{M}^z_{i\,n,m} = (t_n - T_i)^m . \tag{5.10}$$

We introduce the regularisation matrix $\mathbf{C}$ to penalise discontinuities in the displacement and its first derivative and to regularise the offset of the displacement. Discontinuities are only penalised between adjacent chunks. Consecutive chunks are considered to be adjacent if there was no empty chunk removed in between.

$$\mathbf{C} = s_{\text{reg}} \begin{pmatrix} \mathbf{R}(t_0^c - t_0^m) & -\mathbf{R}(t_0^c - t_1^m) & \mathbf{0} & \ddots & \mathbf{0} & \mathbf{0} \\ \mathbf{0} & \mathbf{R}(t_1^c - t_1^m) & -\mathbf{R}(t_1^c - t_2^m) & \ddots & \mathbf{0} & \mathbf{0} \\ \ddots & \ddots & \ddots & \ddots & \ddots & \ddots \\ \mathbf{0} & \mathbf{0} & \mathbf{0} & \ddots & -\mathbf{R}(t_{Z^*-3}^c - t_{Z^*-2}^m) & \mathbf{0} \\ \mathbf{0} & \mathbf{0} & \mathbf{0} & \ddots & \mathbf{R}(t_{Z^*-2}^c - t_{Z^*-2}^m) & -\mathbf{R}(t_{Z^*-2}^c - t_{Z^*-1}^m) \\ \mathbf{S} & \mathbf{0} & \mathbf{0} & \dots & \mathbf{0} & \mathbf{0} \end{pmatrix} . \tag{5.11}$$

Variables t_0^c to $t_{Z^*-2}^c$ represent the times of the intersections between adjacent chunks. The $\mathbf{R}$ matrices hold the displacement basis functions and their first derivative sampled at the intersections between adjacent chunks for each direction:

$$\mathbf{R}(t) = \begin{pmatrix} \mathbf{R}^x(t) & \mathbf{0} & \mathbf{0} \\ \mathbf{0} & \mathbf{R}^y(t) & \mathbf{0} \\ \mathbf{0} & \mathbf{0} & \mathbf{R}^z(t) \end{pmatrix} , \tag{5.12}$$

$$\mathbf{R}^x(t) = \begin{pmatrix} 1 & t & t^2 & \dots & t_x^O \\ 0 & 1 & 2\,t & \dots & O_x\, t^{O_x-1} \end{pmatrix} , \tag{5.13}$$

$$\mathbf{R}^y(t) = \begin{pmatrix} 1 & t & t^2 & \dots & t_y^O \\ 0 & 1 & 2\,t & \dots & O_y\, t^{O_y-1} \end{pmatrix} , \tag{5.14}$$

$$\mathbf{R}^z(t) = \begin{pmatrix} 1 & t & t^2 & \dots & t_z^O \\ 0 & 1 & 2\,t & \dots & O_z\, t^{O_z-1} \end{pmatrix} . \tag{5.15}$$

Without regularisation, the problem would be ill-posed and the whole point cloud could be shifted without influence on the fitting error. Matrix $\mathbf{S}$ forces the offsets of the first chunk $\alpha_{0\,0}^x$, $\alpha_{0\,0}^y$ and $\alpha_{0\,0}^z$ to zero and therefore prevents displacement of the complete surface:

$$\mathbf{S} = \begin{pmatrix} 1 & 0 & 0 & 0 & \dots & 0 \\ 0 & 1 & 0 & 0 & \dots & 0 \\ 0 & 0 & 1 & 0 & \dots & 0 \end{pmatrix} . \tag{5.16}$$

Scalar s_{reg} defines the strength of the regularisation. For our experiments we used a regularisation strength of $s_{\text{reg}} = 10000$. After solving the least squares problem, the segmented points are corrected by subtracting the determined displacement from the point coordinates:

$$P_n^* = P_n - f(t_n) \quad \text{for } n = 0, 1, \dots, N^t - 1\,. \tag{5.17}$$

The entire motion compensation took 350 ms on an Intel Core i7-7700 CPU at 3.60GHz within a single thread.

5.2.6 Outlier Removal

In addition to the removal of implausible chunks during segmentation, we remove outlying chunks in a step between motion compensation and reconstruction. The outlier-removal targets chunks that suffer from saccades or other distortions that were not compensated well enough by the motion compensation and are too small to be detected by the plausibility check during segmentation. Because microsaccades occur at an average rate of 1 to 2 per second, we expect microsaccades in 2 to 4 chunks of the 8 chunks.

The algorithm iteratively removes chunks that increase the *coefficients standard error*[15] of the overall Zernike reconstruction. Given a base set of N segmented and motion-compensated chunks, N different subsets containing $N-1$ chunks are generated by excluding single chunks. The *coefficients standard error* of the 7th-order Zernike reconstruction is determined for each subset. If the smallest *coefficients standard error* is smaller than the *coefficients standard error* of the overall reconstruction, the procedure is repeated with the corresponding subset as the new base set. If not, no outlier is present, and the base set is passed to the reconstruction.

5.2.7 Reconstruction

We use Zernike polynomials to reconstruct the anterior corneal surface from the motion-compensated points and to determine the radial curvature of the surface at points relative to the topographers axis – which is typically aligned to the visual axis. The Zernike polynomials are defined by

$$Z_n^m(\rho,\varphi) = R_n^m(\rho) \begin{cases} \cos(m\,\varphi) & \text{if } m \text{ is positive} \\ \sin(m\,\varphi) & \text{if } m \text{ is negative} \end{cases} , \tag{5.18}$$

where ρ is the normalised radial distance $0 < \rho \leq 1$ and φ is the azimuthal angle. The nonnegative integer n indicates the radial order. Integer m indicates the azimuthal order, where $n - m$ has to be even. The radial polynomials R_n^m are defined by

$$R_n^m(\rho) = \sum_{k=0}^{\frac{n-m}{2}} \frac{(-1)^k\,(n-k)!}{k!\,\left(\frac{n+m}{2}-k\right)!\,\left(\frac{n-m}{2}-k\right)!}\,\rho^{n-2\,k} \,. \tag{5.19}$$

Using the standard ANSI single-index [16], the individual polynomials can be addressed by a single index. The standard ANSI single-index is defined by $j = (n(n+1)+m)/2$. We use Zernike polynomials up to the 10th radial order for the reconstruction, which results in a total of 110 polynomials. The sum of these polynomials represents our Zernike model $Z = \sum_{(n,m)\in O_{10}} Z_n^m$, where O_{10} denotes the set of indices up to the 10th radial order.

We sampled Z at the individual scan positions x_i, y_i and plot the resulting reconstructed axial distances $Z_i = Z(x_i, y_i)$ in the scan (see Fig. 5.6, yellow line). As the A-scans in the scan are displayed as recorded, without any motion correction, the reconstructed axial distances do not coincide with the scanned anterior corneal surface. To illustrate the accuracy of our reconstruction, the compensated motion f has to be incorporated by

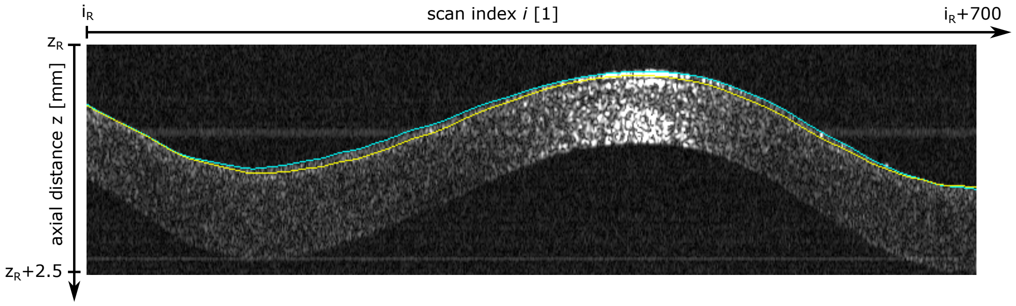

Figure 5.6. Section of a corneal scan as acquired (no motion correction applied). The reconstruction of the anterior corneal surface is delineated by sampling the reconstructed corneal model Z at the scan positions x_i, y_i. Yellow: Sampling of the static model, representing the axial distances to the virtual motion-free anterior corneal surface (Z_i). Cyan: Sampling of the model incorporating the motion profile f determined during motion compensation, recreating the axial distances, as acquired (Z_i^*).

$Z_i^* = Z\left(x_i + f_x(t_i), y_i + f_y(t_i)\right) + f_z(i)$ (cyan line). The match of the cyan line with the scanned anterior corneal surface indicates accurate motion compensation and reconstruction. The difference between the yellow and cyan line illustrates the compensated motion.

The axial curvature K_a, defined by the ISO norm for corneal topographers [17], is the reciprocal of the distance from a point on the surface to the corneal topographer axis along the corneal meridian normal. It is defined by

$$K_\mathrm{a} = \frac{\int\limits_0^{r_\mathrm{p}} K_\mathrm{m}(r)\, dr}{r_\mathrm{p}} \,, \tag{5.20}$$

where K_m indicates the so-called tangential curvature and r_p the perpendicular distance from the corneal topographer axis. The determination of K_m involves the first and second derivatives in radial direction:

$$K_\mathrm{m} = \frac{\frac{\partial^2 M(r)}{\partial r^2}}{\left(1 + \left(\frac{\partial M(r)}{\partial r}\right)^2\right)^{\frac{3}{2}}} \,, \tag{5.21}$$

where $M(r)$ is a function giving the elevation of the meridian at any perpendicular distance, r, from the corneal topographer axis. Using the Zernike representation for the elevation, those derivatives can be calculated from the derivatives of the Zernike polynomials. The derivatives of the Zernike polynomials can be calculated in closed form. In our case, where the corneal vertex is in the centre of the Zernike surface, the derivative of a radial polynomial is given by

$$\frac{\partial R_n^m(r)}{\partial r} = \frac{1}{R}\frac{\partial R_n^m(\rho)}{\partial \rho} = \frac{1}{R} \sum_{k=0}^{\frac{n-m}{2}} \frac{(-1)^k\,(n-k)!}{k!\,\left(\frac{n+m}{2}-k\right)!\,\left(\frac{n-m}{2}-k\right)!}\,(n-2\,k)\,\rho^{n-2\,k-1} \,, \tag{5.22}$$

where r is the radius and R is the radius of the base area. As can be seen from the formula, the influence of the coefficients on the derivative is dependent on the radial order n and azimuthal order m. Thus, even when the reconstruction is stable in the spatial domain and the errors are well-balanced between the coefficients, errors are amplified in the curvature domain depending on the axial and azimuthal order. We identified the instability of the reconstruction in the curvature domain as a major downside of the Zernike reconstruction. Therefore, we implemented a Zernike reconstruction with order-dependent regularisation to achieve more stable curvature maps. Based on a biconic reference fit [18], the Zernike polynomials are regularised relative to their axial and azimuthal order. We determine the Zernike coefficients by the linear least squares problem

$$\hat{\boldsymbol{\beta}} = \arg\min_{\boldsymbol{\beta}} \left\|\mathbf{z} - \mathbf{Z}\boldsymbol{\beta}\right\|^2 + \lambda\, N \left\|\boldsymbol{w} \odot (\boldsymbol{\beta} - \boldsymbol{\beta}_\mathrm{ref})\right\|^2 \,, \tag{5.23}$$

where $\mathbf{z}$ is the vector with the z-coordinates of the points. The variables $\boldsymbol{\beta}$ and $\hat{\boldsymbol{\beta}}$ are the Zernike coefficients and their least-squares fit, respectively. Vector $\boldsymbol{\beta}_\mathrm{ref}$ contains the reference Zernike coefficients for regularisation. The columns of matrix $\mathbf{Z}$ are given by the sampled Zernike polynomials. N is the total number of points to fit. Scalar λ is the global regularisation weight and $\boldsymbol{w}$ is a weighting vector derived from the derivation of the Zernike polynomials. The operator $\odot$ performs element-wise multiplication. The entries of weighting vector $\boldsymbol{w}$ are defined by

$$w_j = \sum_{k=0}^{\frac{n-m}{2}} \frac{(-1)^k\,(n-k)!}{k!\,\left(\frac{n+m}{2}-k\right)!\,\left(\frac{n-m}{2}-k\right)!}\,(n-2\,k)\,, \tag{5.24}$$

where j is the standard ANSI single-index [16]. We determined the global regularisation weight λ based on the *in vivo* measurements (see Chapter 5.3). We restate the problem as

$$\hat{\boldsymbol{\beta}} = \underset{\boldsymbol{\beta}}{\arg\min} \, \|\mathbf{y} - \mathbf{X}\boldsymbol{\beta}\|^2 \tag{5.25}$$

with

$$\mathbf{X} = \begin{pmatrix} \mathbf{Z} \\ \sqrt{\lambda N}\,\mathbf{I}\boldsymbol{w} \end{pmatrix}, \; \mathbf{y} = \begin{pmatrix} \mathbf{z} \\ \sqrt{\lambda N}\,\boldsymbol{\beta}_{\text{ref}} \end{pmatrix}, \tag{5.26}$$

and find the solution by solving

$$(\mathbf{X}^{\mathrm{T}}\mathbf{X})\hat{\boldsymbol{\beta}} = \mathbf{X}^{\mathrm{T}}\mathbf{y}\,. \tag{5.27}$$

5.2.8 Validation

Phantom validation

We used a toric acrylic glass (PMMA) phantom with a steep (flat) radius of 7.8 mm (8.0 mm) to evaluate the performance of the motion compensation. The phantom was manufactured by Sumipro B.V., Netherlands. The shape of the phantom represents a typical eye with astigmatism. The preprocessing for the segmentation was adapted for the segmentation of the phantom surface (see Sec. 5.2.4). We applied motion, simulating typical eye displacements to the phantom by using a piezoelectric translation stage. It consists of axial (along the z axis, which corresponds to the topographer axis) and lateral motion trajectories (in the x,y plane). The applied axial motion was extracted from a prior *in vivo* measurement with our system where we scanned the corneal vertex over 1.75 seconds using a static scan pattern. Because we aligned the scanning to the corneal vertex and the corneal slope is minimal around the vertex, we assumed the change of the corneal position in the scan to be caused by axial eye movement only. The motion applied in the x,y plane represents drift and microsaccades. The drift was parameterised with amplitudes between 3 µm and 30 µm and velocities between 5 µm and 30 µm per second. Saccades were simulated in intervals between $\frac{1}{3}$ and 1 s. The saccades were parameterised with amplitudes between 9 µm and 150 µm and velocities between 1.4 mm and 14 mm per second.

We acquired 10 measurements from the moving phantom and 5 measurements from the same phantom without any movement.

In-vivo validation

We evaluated the *in vivo* repeatability and equivalence of our topography by measurements of 48 healthy eyes. The topography for both eyes of 24 subjects was determined by our method and by two reference topographers, a Scheimpflug imaging tomographer (Pentacam HR, Oculus) and a Placido Disk topographer (Atlas 9000, Carl Zeiss Meditec). Each subject was measured twice with each device, where the subject setup was repeated before each measurement. Thus, 48 eyes were measured twice with three devices, resulting in a total of 288 acquired topographies.

We excluded three subjects entirely from the evaluation. For these subjects, the Atlas indicated low measurement quality and our segmentation showed a deviation caused by an unusual corneal signal. We additionally excluded one subject from the Pentacam measurements and three measurements from the Atlas measurements because the particular device indicated a low measurement quality.

Based on the remaining topographies, we evaluated the repeatability of each device and the mutual equivalence between the devices, as explained in the following sections.

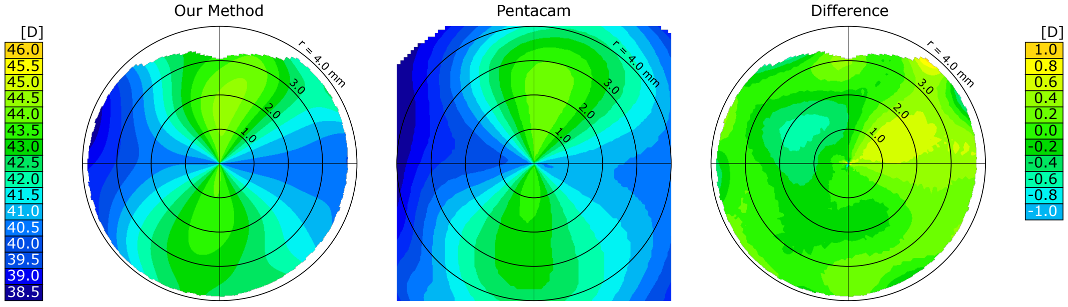

(a) (b) (c) (d) (e)

Figure 5.7. (b) Axial curvature map of our OCT-based topography. (c) Axial curvature map of the Pentacam. (d) The mapped differences between the two topographies. The axial curvature maps are color-coded with increments of 0.5 D between the shades of color (a). The difference map is color-coded with increments of 0.2 D between the shades of color (e). The pentacam map is cropped to a square area with 8 mm lateral extent.

The measurements were conducted by the Eye Clinic of the University Hospital Basel with approval of the local ethics committee. Following the tenets of the Declaration of Helsinki, the measurements were performed with the full understanding and written consent of the volunteers.

Calculation of the difference between topographies

For the calculation of the difference between two topographies, we first ensure that the vertices of the topographies are aligned. As the maps provided by the Pentacam and the Atlas are already aligned to the vertex, we only had to align our map. The position of the vertex was determined from the Zernike coefficients as described in [19]. Figure 5.7 shows two aligned topography maps and the mapped differences. The ISO norm for Corneal topographers [17] defines two measures for the difference between two topographies: the *difference mean* and the *standard deviation of the differences.* To compare two topographies i and j, both topography maps are sampled at a defined set of positions k and the weighted differences for these positions are calculated by

$$\Delta D_{ijk} = w_k(D_{ik} - D_{jk})\,, \tag{5.28}$$

where D indicates the curvature. The area weighting value w_k for each data point depends on the sampling point distribution. Its purpose is to ensure that the specific sampling distribution is equivalent to uniform sampling. Because we use a polar coordinate distribution, the weight is calculated according to the norm by

$$w_k = \frac{n r_k}{\sum\limits_{k=1}^{n} r_k}\,, \tag{5.29}$$

where n is the number of measurements in the zone and r_k is the radial position of measurement k. The norm divides the topography maps into three zones: a central zone from radius 0.5 mm to 1.5 mm, a middle zone from 1.5 mm to 3 mm and an outer zone from 3 mm up (to 4 mm in our case). For each zone, the *difference mean* M_{ij} and a the *standard deviation of the differences* s^*_{ij} are calculated by

$$M_{ij} = \frac{1}{n}\sum_{k=1}^{n} \Delta D_{ijk}\,, \tag{5.30}$$

$$s^*_{ij} = \sqrt{\frac{\sum\limits_{k=1}^{n} (\Delta D_{ijk} - M_{ij})^2}{n-1}} \tag{5.31}$$

$$= \sqrt{\frac{\sum\limits_{k=1}^{n} (w_k(D_{ik} - D_{jk}) - M_{ij})^2}{n-1}}\,. \tag{5.32}$$

Assuming two topographies with a constant non-zero difference m_{ij}, the *difference mean* is $M_{ij} = m_{ij}$ and *standard deviation of the differences* simplifies to

$$s^*_{ij} = \sqrt{\frac{\sum\limits_{k=1}^{n} (w_k\, m_{ij} - m_{ij})^2}{n-1}} = \sqrt{\frac{m^2_{ij} \sum\limits_{k=1}^{n} (w_k - 1)^2}{n-1}}\,. \tag{5.33}$$

If the sampling distribution is uniform, all weights w_k would be one and the s^*_{ij} would be zero. If the sampling distribution is not uniform like in our case, s^*_{ij} is not zero and dependent on the variance of the weights and the difference mean. However, we expect the *standard deviation of the differences* to be zero in case of a constant difference between two maps. Thus, we adapted the definition to eliminate the weight-dependent influence of the difference mean by

$$s_{ij} = \sqrt{\frac{\sum\limits_{k=1}^{n} (w_k\,(D_{ik} - D_{jk} - M_{ij}))^2}{n-1}}\,. \tag{5.34}$$

We interpret the *standard deviation of the differences* as a measure for the difference of the aberrations in two topographies. In total, the calculation of the difference between two topographies yields six numbers: the *difference mean* and *standard deviation of the differences* for three zones.

Calculation of the repeatability and equivalence

***In vivo* repeatability** For the assessment of *in vivo* repeatability, we calculated the difference between the first and second topography of each eye and device. Each difference includes the *difference mean* and *standard deviation of the differences* for the three zones.

Based on these differences (per eye), we calculate two measures for the repeatability of each zone (per ensemble): (1) the standard deviation of the *difference mean* as a measure for the *repeatability of the mean*, and (2) the mean of the *standard deviation of the differences* as a measure for the *repeatability of the aberrations*. We use the mean as a measure for the *repeatability of the aberrations* because the *standard deviation of the differences* is always positive.

Phantom repeatability To assess the repeatability of the topography from the 10 measurements of the moving phantom, 10 pairs were generated, and the topography difference was calculated for each pair. Given the 10 topographies T_i with $i = 0 \ldots 9$, the differences $T_j - T_{j+1}$ for $j = 0 \ldots 8$ and $T_9 - T_0$ were determined. The measures for the *repeatability of* *the mean* and the *repeatability of the aberrations* were calculated analogously to the *in vivo* repeatability. The same procedure was applied to the assessment of the repeatability of the 5 topographies of the static phantom.

***In vivo* equivalence** For the assessment of the equivalence of two devices, we calculated two differences for each eye: the difference between the first topography of each device and the difference between the second topography of each device. Each difference includes the *difference mean* and *standard deviation of the differences* for the three zones.

Based on these differences (per eye), we calculate two measures for the equivalence of each zone (per ensemble): (1) The mean of the *difference mean* as a first measure for the *equivalence of the mean*, (2) the standard deviation of the *difference mean* as a second measure for the *equivalence of the mean*, and (3) the mean of the *standard deviation of the differences* as a measure for the *equivalence of the aberrations*.

Adjustment of the topography for equivalence of the mean

We observed systematic differences between the OCT-based delineation of the anterior corneal surface and the Placido disc reflection. These differences were expected in advance due to the different measurement modalities. Thus, we performed a simple adjustment of our topography to the topography provided by the Atlas. The adjustment parameters were determined based on additional *in vivo* measurements, acquired analogously to the measurements for *in vivo* validation. The adjustment was applied to z-coordinates of the segmented point by a conic correction. For the correction, we first fit a conic section of revolution to the motion-compensated point cloud [18]. The parameters r and p of the conic section of revolution are adjusted by $R^* = R + \Delta R$ and $p^* = p + \Delta p$, resulting in an adjusted conic section of revolution. The difference between the z-position of the adjusted and the original conic section of revolution is determined at the lateral position of each point and added to the z-coordinate of the point. The reported results are based on an adjustment of $\Delta R = 0.166 \times 10^{-3}$m and $\Delta p = 0.19$,

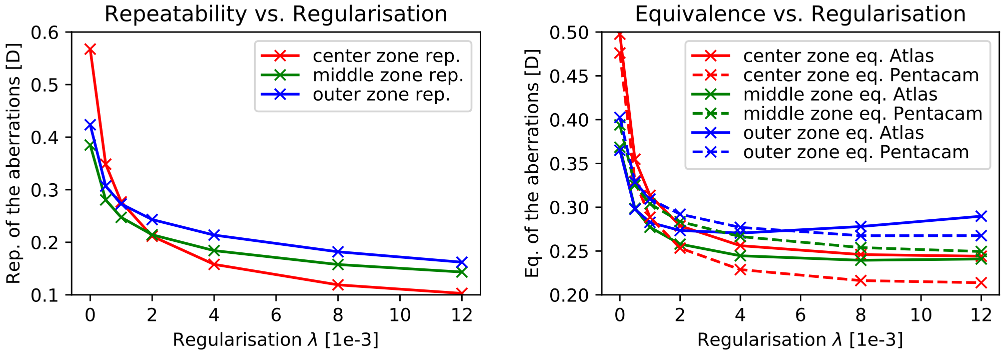

(a) (b)

Figure 5.8. Influence of the regularisation on (a) the repeatability of the aberrations and (b) the equivalence of the aberrations with Atlas (solid) and Pentacam (dashed), for the central zone (red), middle zone (green) and outer zone (blue).

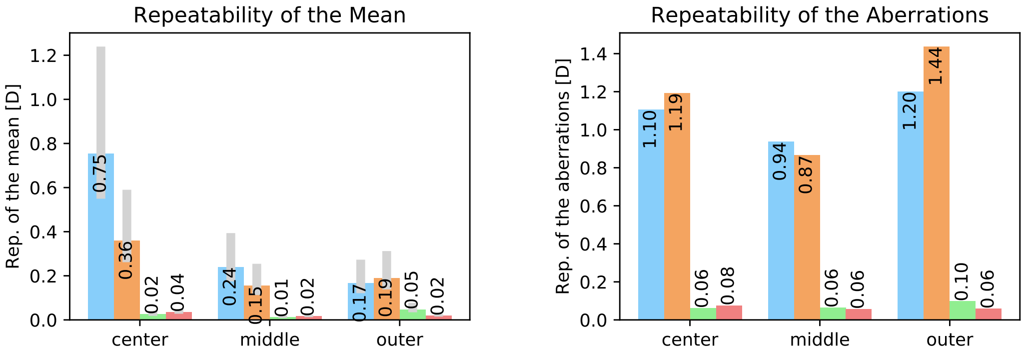

(a) (b)

Figure 5.9. Repeatability of the topographies from phantom measurements: (a) The *repeatability of the mean* and (b) the *repeatability of the aberrations*. The repeatability for the moved phantom is given without motion compensation and without outlier removal (blue), without motion correction but with outlier removal (orange) and with motion compensation and outlier removal (green). The repeatability for the static phantom is shown in red. The 95 % confidence interval for the *repeatability of the mean* is indicated by the gray bars.

Table 5.1. Effect of the motion compensation on the difference to the theoretical topography for the measurement of the moved phantom shown in Figure 5.11.

	without motion compensation			with motion compensation		
Measure	central	middle	outer	central	middle	outer
Difference mean M [D]	0.578	0.056	-0.152	-0.034	0.04	-0.098
Standard deviation of the differences s [D]	1.328	1.077	1.474	0.041	0.065	0.112

5.3 Results

Effect of the regularisation Figure 5.8 illustrates the effect of the global regularisation weight on the *in vivo* repeatability of our OCT-based topography and the equivalence with the reference topographers. While the repeatability steadily improves with increasing regularisation, the equivalence with the Altas in the central zone becomes worse after an initial improvement. Based on these characteristics, we have chosen a regularisation weight of $\lambda = 0.004$ for the following evaluation.

Phantom repeatability and equivalence Figure 5.9 illustrates the effect of the motion compensation on the repeatability of the moved phantom topography, in comparison with the repeatability of the static phantom topography. As can be seen, the motion compensation improves the repeatability by orders of magnitude and brings it to the level of the repeatability of static phantom topography. Figure 5.10 provides an example for the detected and compensated motion in one of the measurements, showing good correlation. We zoomed in a typical response of the motion compensation to a simulated saccade. Although the motion compensation is able to correct the shift induced by the saccade, the speed of the motion compensation response is limited to around 0.1 s, which corresponds to a maximal frequency of the lateral motion compensation of around 10 Hz. Figure 5.11 illustrates the difference between the theoretical topography of the phantom, the topography of the moved

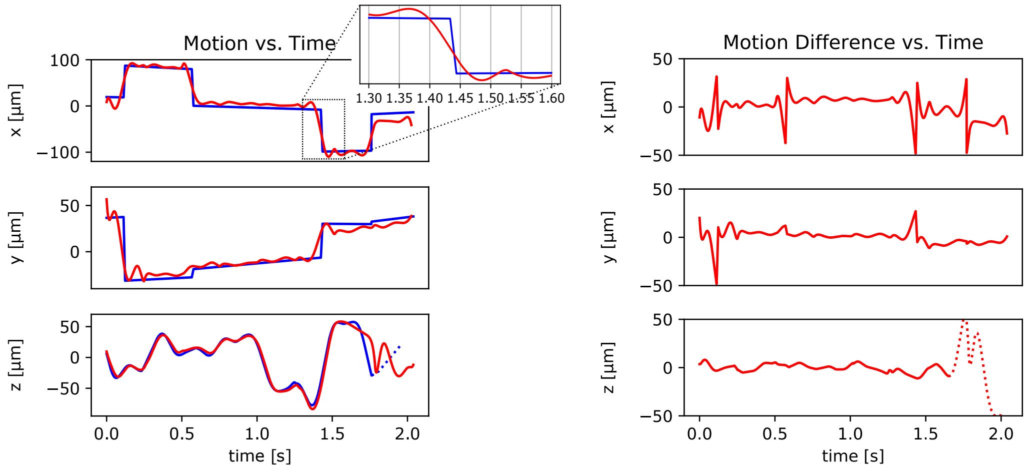

(a) (b)

Figure 5.10. (a) The compensated motion (red) and the motion applied to the phantom (blue) for a measurement of the moved phantom. The axial motion obtained by prior *in vivo* measurements (solid blue) was complemented by an unnatural linear part to obtain periodic motion (dotted blue). (b) The difference between the compensated motion and the applied motion.

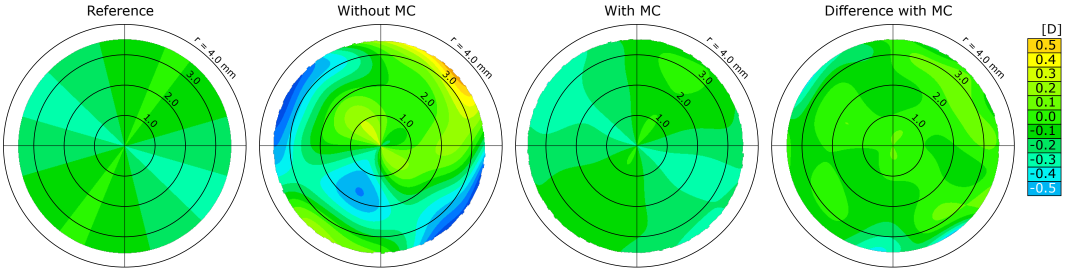

(a) (b) (c) (d) (e)

Figure 5.11. Effect of the motion compensation on the topography for a measurement of the moved phantom. (a) Theoretical axial curvature map. (b) Axial curvature map without motion compensation. (c) Axial curvature map with motion compensation. (d) The mapped differences between the curvature map with motion compensation and the theoretical axial curvature map. The axial curvature maps are color-coded with increments of 0.5 D (Fig. 5.7a). The difference map is color-coded with increments of 0.1 D (e). The corresponding difference measures can be found in Table 5.1.

phantom with and without motion compensation, and the deviation between the motion-compensated topography and the theoretical topography. Table 5.1 lists the corresponding difference measures (see Sec. 5.2.8). As can be seen, the *difference mean* in the middle and outer zones is low for the topography without motion compensation although the topography map is quite different. This confirms that the measure *standard deviation of the differences* is needed to quantify the difference between topographies as the other measure, *difference mean*, is blind for irregular differences (aberrations).

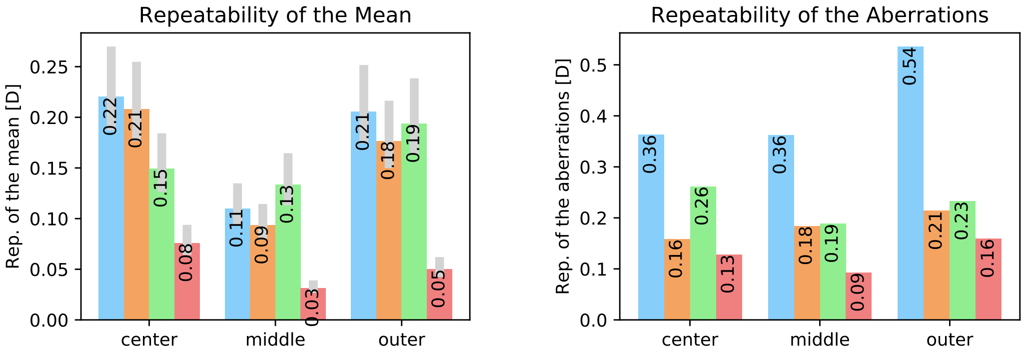

(a) (b)

Figure 5.12. Repeatability of the topographies from *in vivo* measurements: (a) *repeatability of the mean* and (b) *repeatability of the aberrations* without motion compensation (blue), with motion compensation (orange), for the Atlas (green) and for the Pentacam (red).

Table 5.2. Mean and the standard deviation (SD) of the zone differences between our method, Atlas and Pentacam. The p-value for the mean of the *difference mean* is calculated using the one sample t-test for the null hypothesis of zero mean difference.

	Our Method *vs.* Atlas	Our Method *vs.* Pentacam	Atlas *vs.* Pentacam
	difference mean [D]		
zone	mean (SD)	mean (SD)	mean (SD)
central	0.07* (0.37)	0.24* (0.38)	-0.17* (0.15)
middle	-0.06* (0.18)	0.01 (0.19)	-0.07* (0.14)
outer	-0.09* (0.18)	-0.11* (0.19)	0.05* (0.17)
	* statistically significant (p-value < 0.05)		
	standard deviation of the differences [D]		
zone	mean	mean	mean
central	0.26	0.23	0.26
middle	0.24	0.27	0.22
outer	0.27	0.28	0.33

***In vivo* repeatability** Figure 5.12 shows the *in vivo* repeatability of our OCT-based topography with and without motion compensation, together with the repeatabilities of the reference topographies. For the mean of the central zone, our method shows inferior repeatability than both reference topographies. For the other zones, the motion compensation enhances the repeatability to a level that is between the repeatabilities of the Atlas and the Pentacam.

***In vivo* equivalence** Figure 5.13 shows the difference between our OCT-based topography, the Atlas topography and the Pentacam topography for the individual eyes, using the *difference mean* and *standard deviation of the differences* described in Section 5.2.8. Figure 5.13a shows the *difference mean* over the mean of the *mean map*. The *mean map* is generated by averaging our topography and the Atlas topography. Figure 5.13b shows the

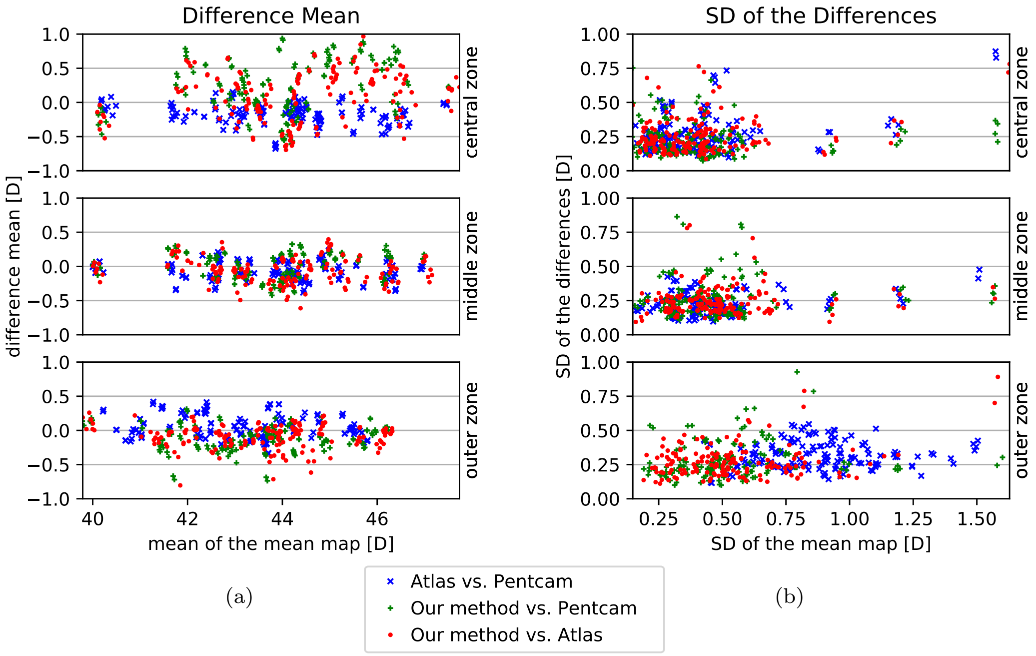

(a)

(b)

Figure 5.13. *Difference mean* (a) and *standard deviation of the differences* (b) between the devices for the different zones. The mean and standard deviation of the *difference mean* as well as the mean of the *standard deviation of the differences* are listed in Table 5.2.

standard deviation of the differences over the standard deviation of the *mean map*.

Table 5.2 summarises the measures of equivalence (see Section 5.2.8) between the topographies. Although the comparison shows some statistically significant differences, we judge the equivalence from a clinical point of view. To judge the clinical equivalence of our OCT-based topography, we use the difference between the Atlas and the Pentacam as primary baseline as they both are clinically approved topographers. As an additional baseline, eyes are commonly classified as ametropic if their absolute refractive error is above 0.5 D [20]. Further, vision corrections are typically available in 0.25 D steps [21]. This indicates that refractive errors below 0.25 D do not have high clinical relevance.

The mean of the *difference mean* between our method and the reference topographies is consistent with the difference between the reference topographies. The reference devices show a difference in the central zone, which we did not expect on this order of magnitude, but is still below 0.25 D.

The standard deviation of the *difference mean* is lower between the reference topographies than between our method and both of the reference topographies, especially for the central zone.

The mean of the *standard deviation of the differences*, the measure for the *equivalence of the aberrations*, is on a similar level for all zones.

Comparison with McNabb *et al.* A direct comparison with the results of McNabb *et al.* [22] is not possible because they did not evaluate the mean curvature and aberrations for the different zones. Instead, they calculated a spherical equivalent power, combining the anterior and posterior corneal curvature. Because we did not evaluate the posterior corneal surface, we are not able to provide a similar measure. However, McNabb *et al.* reported the repeatability of the mean anterior radius of curvature over a 5-mm-diameter area. We thus additionally determined the mean curvature over a 5-mm-diameter. The resulting SD of the paired differences is 40 µm in radius or 0.23 D in refractive power, assuming a refractive index difference of 0.3375. McNabb *et al.* reported a repeatability of 26 µm for their DSOCT method, calculated by the population mean of the SD of repeated measurements. Assuming that paired differences are pulled from normal distributions with the same standard deviation of 26 µm, the expected SD of the paired differences is $26\,\mu\text{m} \times \sqrt{2} = 37\,\mu\text{m}$, which is comparable to our repeatability of 40 µm.

5.4 Discussion

We presented a complete pipeline for OCT-based corneal topography, including novel methods for scanning, motion compensation and reconstruction. We validated the methods by phantom and *in vivo* measurements. Unlike others [22], we directly compared axial curvature maps instead of derived values such as mean curvatures or axes. The comparison yields separate measures for mean refractive power and aberrations, allowing a more differentiated assessment. The reported results show that our OCT-based topography is comparable with established topographers in terms of repeatability. The equivalence of the aberrations is also at a similar level compared to the reference topographies. For the equivalence of the mean power, we need to differentiate between the mean equivalence and the variations. The mean equivalence is comparable with the reference topographies, whereas the variations in the mean power difference are increased, especially for the central zone.

Nevertheless, we demonstrated that our motion compensation can handle typical eye movements and enhances the repeatability and equivalence of the topography. The results indicate that motion compensation is crucial to achieve a performance that is comparable with established topographers. Other than current methods, we compensate for motion in three dimensions in a single optimisation step. We want to emphasise, that no part of the scan is considered motion-free as done in common methods. Instead, we use a continuous motion model which enables motion compensation with higher temporal resolution and without discretisation artefacts. We therefore presented, to our knowledge, the first continuous motion compensation for OCT measurements of the cornea.

The presented regularisation scheme addresses the stability problems occurring in the curvature space of the Zernike reconstruction. Results show that the regularisation enhances the repeatability of the corneal topography without sacrificing the equivalence with reference topographers.

We want to highlight that the presented motion compensation and reconstruction methods can easily be applied to other scan systems. We further want to emphasise that although we use the motion compensation together with our optimised scan pattern, the method itself is generic and can be applied to other scan patterns with ease. However, there are some limitations that we want to discuss in the next section.

5.4.1 Limitations and further research

First of all, we optimised and validated the regularisation with measurements of healthy eyes. Thus, the applicability to highly irregular eyes has to be investigated in further studies.

Additionally, the presented scan pattern features a non-uniform scan point distribution, which is suboptimal regarding the stability of Zernike reconstruction [3]. A uniform distribution could be obtained by modulating the speed along the trajectory. However, this would lead to scanner control signals with larger bandwidth, which is why we did not do so in the first place.

Another point to mention is that the optimal chunk size for segmentation and motion compensation, together with the the order of the motion polynomials, are still under investigation. On the one hand, a smaller chunk size for segmentation could reduce the number of removed A-scans during segmentation and outlier detection. Further, the order of the motion polynomials could be reduced, which would potentially increase the stability of the motion compensation. On the other hand, a smaller chunk size potentially reduces the general stability of the Zernike reconstruction used for plausibility check. Increasing the order of the motion polynomials would increase the maximal frequency of the motion compensation but would in return potentially reduce the stability of the motion compensation.

The axial resolution of our system is also low compared to other systems used for corneal topography [6, 8], a limitation resulting from the large axial scan range. However, as mentioned above, our methods can be applied to other scan systems with ease. By using a system with a higher axial resolution, the regularisation of the reconstruction could be reduced while maintaining similar repeatability, enhancing the ability to represent irregularities.

Finally, we only compensate for linear motion of the cornea. The compensated motion includes the linear motion that is induced by the head movements as well as the linear corneal motion induced by rotation of the eye. The results show that the compensation of the linear motion is crucial for the resulting topography. However, there is a rotational part of the motion that is not handled by our motion compensation. The investigation of the impact of rotational motion and the inclusion of the rotational motion in our model is the topic of current and future research.

References

[1] Trevor Anderson et al. “3D spectral imaging system for anterior chamber metrology”. In: *Optical Coherence Tomography and Coherence Domain Optical Methods in Biomedicine XIX*. Vol. 9312. International Society for Optics and Photonics. 2015, 93120N.

[2] Patrycjusz Stremplewski et al. “In vivo volumetric imaging by crosstalk-free full-field OCT”. In: *Optica* 6.5 (2019), pp. 608–617.

[3] Joerg Wagner, David Goldblum, and Philippe C Cattin. “Golden angle based scanning for robust corneal topography with OCT”. In: *Biomedical Optics Express* 8.2 (2017), pp. 475–483.

[4] Maolong Tang et al. “Corneal power measurement with Fourier-domain optical coherence tomography”. In: *Journal of Cataract & Refractive Surgery* 36.12 (2010), pp. 2115–2122.

[5] Mingtao Zhao, Anthony N Kuo, and Joseph A Izatt. “3D refraction correction and extraction of clinical parameters from spectral domain optical coherence tomography of the cornea”. In: *Optics express* 18.9 (2010), pp. 8923–8936.

[6] Sergio Ortiz et al. “Corneal topography from spectral optical coherence tomography (sOCT)”. In: *Biomedical optics express* 2.12 (2011), pp. 3232–3247.

[7] Sergio Ortiz et al. “Quantitative OCT-based corneal topography in keratoconus with intracorneal ring segments”. In: *Biomedical optics express* 3.5 (2012), pp. 814–824.

[8] Ryan P McNabb et al. “Distributed scanning volumetric SDOCT for motion corrected corneal biometry”. In: *Biomedical Optics Express* 3.9 (2012), pp. 2050–2065.

[9] Ryan P McNabb, Anthony N Kuo, and Joseph A Izatt. “Quantitative single and multi-surface clinical corneal topography utilizing optical coherence tomography”. In: *Optics letters* 38.8 (2013), pp. 1212–1214.

[10] Robert J Zawadzki et al. "Three-dimensional ophthalmic optical coherence tomography with a refraction correction algorithm". In: *European Conference on Biomedical Optics*. Optical Society of America. 2003, 5140_20.

[11] Martin F Kraus et al. "Motion correction in optical coherence tomography volumes on a per A-scan basis using orthogonal scan patterns". In: *Biomedical optics express* 3.6 (2012), pp. 1182–1199.

[12] Yiwei Chen et al. "Three-dimensional eye motion correction by Lissajous scan optical coherence tomography". In: *Biomedical optics express* 8.3 (2017), pp. 1783–1802.

[13] ISO-15004-2:2007. *Ophthalmic instruments - fundamental requirements and test methods - part 2: light hazard protection.* Tech. rep. International Organization for Standardization, 2007.

[14] Sergio Ortiz et al. "Optical distortion correction in optical coherence tomography for quantitative ocular anterior segment by three-dimensional imaging". In: *Optics express* 18.3 (2010), pp. 2782–2796.

[15] Joerg Wagner, Simon Pezold, and Philippe C Cattin. "Model-Driven 3-D Regularisation for Robust Segmentation of the Refractive Corneal Surfaces in Spiral OCT Scans". In: *4th MICCAI Workshop on Ophthalmic Medical Image Analysis* (2017).

[16] ANSI-Z80.28-2017. *Methods for Reporting Optical Aberrations of Eyes.* Tech. rep. American National Standards Institute, 2017.

[17] ISO-19980:2012. *Ophthalmic instruments - Corneal topographers.* Tech. rep. International Organization for Standardization, 2012.

[18] Damien Gatinel et al. "Corneal elevation topography: best fit sphere, elevation distance, asphericity, toricity and clinical implications". In: *Cornea* 30.5 (2011), pp. 508–515.

[19] Boy Braaf et al. "Calculating angle lambda (λ) using zernike tilt measurements in specular reflection corneal topography". In: *Journal of Optometry* 2.4 (2009), pp. 207–214.

[20] Ecosse L Lamoureux et al. "The impact of corrected and uncorrected refractive error on visual functioning: the Singapore Malay Eye Study". In: *Investigative Ophthalmology & Visual Science* 50.6 (2009), pp. 2614–2620.

[21] Edward S Bennett and Barry A Weissman. *Clinical contact lens practice.* Lippincott Williams & Wilkins, 2005.

[22] Ryan P McNabb et al. "Optical coherence tomography accurately measures corneal power change from laser refractive surgery". In: *Ophthalmology* 122.4 (2015), pp. 677–686.

6 Equivalent Simulated Keratometry by Optical Coherence Tomograpy

So far, we presented several methods to enable corneal topography by OCT. As stated in the introduction, keratometry is another important measure for ophthalmologists. In this chapter, we discuss the requirements and propose a method for equivalent simulated keratometry by OCT. The method relies on the same methods for scanning, segmentation and motion correction that we used in Chapter 5. This analysis is yet unpublished.

6.1 Introduction

Keratometry provides information on the cornea's refractive power which is essential for cataract surgery, the replacement of the natural lens by an intraocular lens (IOL). Ophthalmologists rely on keratometry to determine the suitable IOL by using so-called IOL formulas.

Keratometry assesses the refractive power of the central zone of the cornea. The central zone of the cornea has a diameter of around 2 mm and is also called apical zone, corneal cap or central spherical zone [1, 2]. Keratometry provides so-called K-readings (or K-values) composed of the flat and steep meridional power (K1 and K2, where $\mathrm{K1} < \mathrm{K2}$) and their axis. Alternatively, the mean refractive power $\mathrm{Km} = (\mathrm{K1} + \mathrm{K2})/2$ together with the amount $\mathrm{Ast} = \mathrm{K2} - \mathrm{K1}$ and axis of astigmatism bears the same information. Astigmatism is a refractive error that results in blurred vision because the focal point varies with the angle. In regular astigmatism, the flat and steep meridian are perpendicular to each other by definition. Therefore, the axes of K1 and K2 are completely defined by the axis of the flat meridian.

Classical keratometers make use of the reflective nature of the anterior corneal surface to determine the corneal curvature and refractive power. Because of the reflective nature of the anterior corneal surface, the cornea acts like a convex mirror: An object in front of the cornea forms a virtual image (1^{st} Purkinje image) of the object with reduced size. This allows the determination of the curvature based on the known relationship between curvature, object size, virtual image size and distance to the cornea. The refractive power of the anterior corneal surface can be calculated based on the radius of curvature and the refractive index of the cornea. Often, the cornea is regarded as a single refractive surface with an effective refractive index. This refractive index also takes into account the expected refractive power of the posterior corneal surface. Usually, an effective refractive index of 1.3375 is used, but other values like 1.376 and 1.3315 are also used [3].

Automatic keratometers like the LENSTAR 900 (Haag-Streit AG, Köniz, Switzerland) determine the curvature by measuring the virtual image size and the distance to the cornea automatically. Typically, they use a ring of luminescent points placed in front of the cornea. The keratometer captures the virtual image of these so-called keratometry points by a camera and determines the axial distance from the camera to the cornea. Figure 6.1 illustrates the formation of the virtual image by the corneal surface. In the case of the LENSTAR 900,

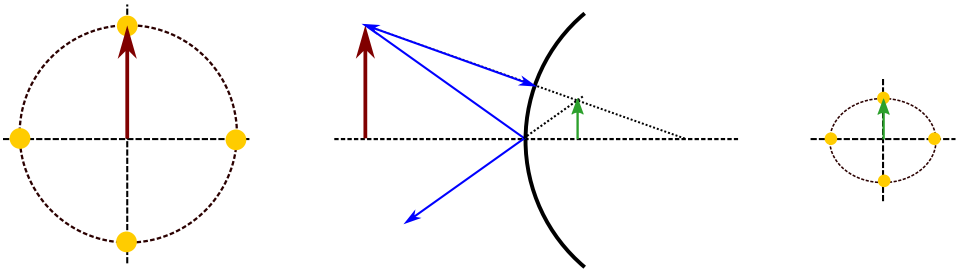

Figure 6.1. Illustration of automatic keratometry. The vectors illustrate the object (red) and its virtual image (green) for a chosen keratometry point (yellow). Left: Keratometry ring with four keratometry points. Middle: Formation of the virtual image for a chosen keratometry point. Right: virtual image formed by the reflection of the keratometry ring for an eye with astigmatism.

two concentric rings of keratometry points are used, and the axial distance to the cornea is determined by optical low coherence reflectometry (OLCR).

Using the same principle of OLCR, OCT is not limited to one-dimensional measurements but enables the acquisition of two-dimensional, cross-sectional images and volumes. This enables the spatial measurement of the cornea and the assessment of its shape. For keratometry by OCT, the curvature has to be determined based on this spatial measurement. A common way is to fit a model to the corneal shape and to determine the curvature based on this model. Both are common: fitting a two-dimensional model to measured meridians or fitting a three-dimensional model to the whole measurement. Tang *et al.* [4] scanned the cornea with a scan pattern consisting of eight evenly spaced meridional A-scans. They calculated the anterior and posterior curvature along each meridian by parabolic fitting over the central 3-mm-diameter area. The curvatures were averaged to determine the spherical power of the cornea. McNabb *et al.* [5] and Kuo *et al.* [6] both used scan patterns consisting of several meridional scans. After correcting for axial motion, they determined a single curvature value by applying the best fit sphere to the segmented surfaces of the cornea. This procedure removes any information about higher-order aberrations such as astigmatism or coma, only providing a value for the mean refractive power of the cornea. In a newer publication [7], they extended their method to account for astigmatism. They fitted the corneal surfaces by a 5-mm-diameter fifth-order Zernike polynomial and generated a curvature map. Based on the map, they calculated the power along the principal axes at the corneal vertex. None of these methods addresses the equivalency with established keratometers. Instead, Huang *et al.* [8] presented new formulas for the determination of IOL powers based on their OCT-based corneal power measurement.

The IOL-formulas and their parametrisation evolved over the years based on the keratometry and refractive outcome of patients. To enable the use of established IOL-formulas, simulated keratometry has to be interchangeable with established keratometers. We first investigate the effect of the corneal shape on the K-readings of a reference keratometer. We simulate the effect of the corneal shape on the reference keratometry and on the size of the area on the cornea that is evaluated. We then discuss the influence of the model selection and the K-value calculation on the equivalence with reference keratometry and propose a method for OCT-based keratometry.

The proposed method takes into account the aspherical shape of the cornea and the evaluation area of the reference keratometry, providing OCT-based keratometry that is interchangeable with reference keratometry. The methods are validated by comparing *in vivo* measurements to reference keratometry.

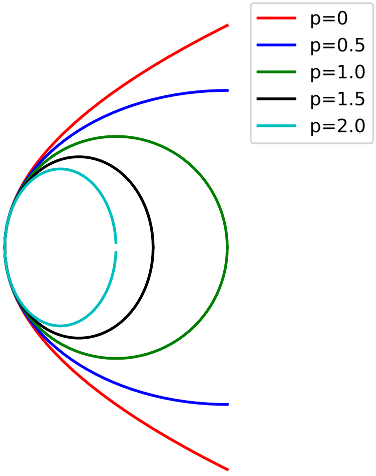

Figure 6.2. Influence of the shape measure p on the conic.

6.2 Methods

6.2.1 Shape of the Cornea

The description of the corneal power provided by keratometry is a simplification, giving only the information that is most relevant for the vision – the mean power and astigmatism of the apical zone. Keratometers assume an anterior corneal shape with circular meridians. This assumption might be valid for the apical zone of the cornea [9], but the typical cornea flattens out with increasing distance from the apex and the spherical model becomes less accurate [10, 9].

Whereas the apical zone of the cornea is assumed to have spherical meridians, the more extended corneal surface is commonly modelled as a biconic surface [10, 9, 11, 12]. The biconic surface has a conic profile along any arbitrary meridian. As the name implies, a biconic is defined by two principal conical meridians, each defined by a radius and p, a measure for the asphericity. The axes of the principal meridians are orthogonal to each other. Figure 6.2 shows the influence of the shape measure p on the conic shape.

This model represents most of the basic optical properties of the cornea [12]. Gatinel *et al.* [12] simplified the biconic model for their simulations by using a single asphericity value for all meridians. Navarro *et al.* [13] used a more extensive model, consisting of a biconic with added Zernike polynomial expansion. In their investigation of the corneal shape, only high order aberrations were identified by the Zernike polynomials. Thus, the Zernike polynomial expansion is only necessary if high order aberrations have to be mapped, which is not the case for keratometry.

As mentioned above, the profile along any arbitrary meridian of a biconic describes a conic section. The equation for a conic section in the r,z plane with its apex at the origin ($r = 0$ and $z = 0$) and tangent to the r axis is

$$r^2 - 2Rr + pz^2 = 0\,, \tag{6.1}$$

where R is the radius of curvature at the apex and p is the shape measure p describing the flattening of the cornea. This formula can be converted to

$$z(r) = \frac{\frac{1}{R}\, r^2}{1 + \sqrt{1 - \frac{1}{R^2}\, p\, r^2}}\,. \tag{6.2}$$

A shape measure p of 1 results in a circular curve with radius R, $p < 1$ in a prolate ellipse and $p > 1$ in a oblate ellipse. Apart from the shape measure p, there are other common parameters to describe the same asphericity of the cornea: the asphericity quotient Q, also called Q-value, the conic constant K, the shape factor E and the eccentricity e. These parameters are related to each other by $Q = K = -E$, $Q = p - 1$ and $Q = -e^2$ [14]. As shown in Section 2.5, the typical p varies between 0.2 and 1.1 with an accumulation around 0.65. For the biconic, the radius and asphericity vary with the angle around the z-axis ϕ_z:

$$R(\phi_z) = R_1 + (R_2 - R_1)\, sin^2(\phi_z - \phi_{z1}) \tag{6.3}$$

$$p(\phi_z) = p_1 + (p_2 - p_1)\, sin^2(\phi_z - \phi_{z1})\,, \tag{6.4}$$

where ϕ_{z1} is the angle of the flat axis, R_1 and p_1 are the radius and shape measure of the flat axis and R_2 and p_2 are the radius and shape measure of the steep axis.

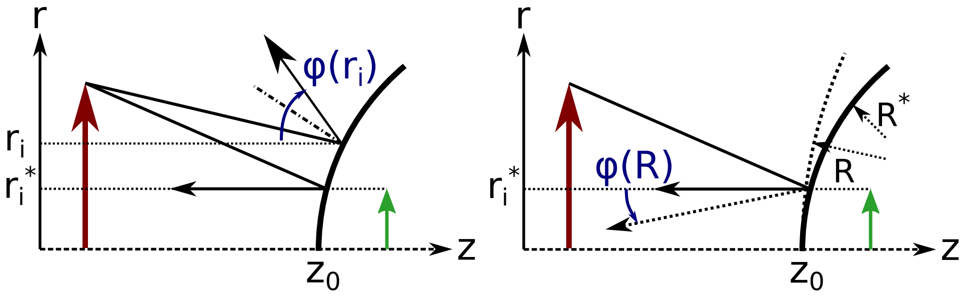

Figure 6.3. Left: Determination of the virtual image size (Eq. 6.5); right: Determination of the sphere radius (Eq. 6.6). The vectors illustrate the object (red) and its virtual image (green).

6.2.2 Simulation of the Reference Keratometry

Our reference is an established automatic keratometer, the LENSTAR 900. We simulate the keratometry of the LENSTAR 900 assuming a biconical shape of the cornea.

As already mentioned, the LENSTAR 900 uses two concentric rings of keratometry points. If the device is correctly aligned to the apex, both the centre of the keratometry rings and the corneal apex are at the centre of the camera image. For each keratometry point, the curvature along the meridian is given by the radial position of the reflected point in the camera image. Assuming telecentric optics, the resulting keratometry values only incorporate the zone spanned by the keratometry ring in the virtual image. Typically, this zone has a diameter of around 2 mm, corresponding to the apical zone of the cornea. The exact size depends on the size of the keratometry rings, their distance to the cornea and the shape of the cornea. Because the size of the rings is fixed by design and the distance is fixed by automatic alignment, the size of the zone only depends on the shape of the cornea.

The keratometry rings have radii of 19 mm and 23 mm, with 16 keratometry LEDs on each ring. The distance to the cornea is controlled by the device to be 70 mm.

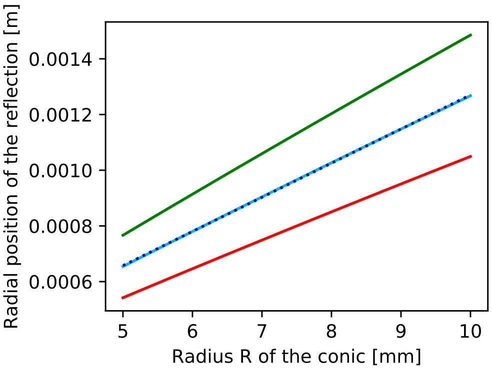

Figure 6.4. Influence of the apical radius on the radial position of the reflected keratomety point. The red (green) curve shows the radial positions of the inner (outer) keratometry point over different radii of a sphere. The blue curve shows the mean of the radial positions. The dotted curve shows the same curve different radii of an asphere with $p = 0.5$.

For our simulation, we assume a telecentric optic of the camera, meaning that the image magnification is independent of the distance. We simulate the keratometry for each keratometry point in two steps: First, the position of the keratometry point in the virtual image is determined for a given conic. This is done by finding the radial position $\mathbf{r_i^*}$ on the conic where the reflected ray is parallel to the axis (*cf.* Fig. 6.3 left), via

$$\mathbf{r_i^*} = \underset{\mathbf{r_i}}{\operatorname{argmin}}(|\varphi(\mathbf{r_i})|)\,. \tag{6.5}$$

Second, we determine the radius $\mathbf{R}^*$ of the circle that would lead to the same position of the keratometry point in the virtual image (*cf.* Fig. 6.3 right), corresponding to the curvature radius that would be determined by the keratometer:

$$\mathbf{R}^* = \underset{\mathbf{R}}{\operatorname{argmin}}(|\varphi(\mathbf{R})|)\,. \tag{6.6}$$

Because the LENSTAR 900 has two keratometry rings, the simulation is performed for two radial positions of the keratometry points. The resulting curvature radii are averaged to obtain a single curvature radius.

Figure 6.4 shows the radial positions of the keratometry points for different radii. Figure 6.5a shows the influence of the asphericity on the determined curvature. As can be seen, the influence of the asphericity is bigger for the outer keratometry ring.

Figure 6.5b illustrates that the curvature radius determined for a keratometry point corresponds to the axial curvature of the surface at the point of reflection. The axial curvature is defined as the distance from the surface to the keratometry axis in direction of the meridional surface normal. Therefore it is given by the slope in direction of the meridian and the distance to the keratometry axis. Thus, instead of simulating the keratometry by Equation 6.6, the axial curvature at the point of reflection can be determined.

Figure 6.6a shows the influence of a fixed evaluation radius on the difference between our method and the simulated reference keratometry. For each evaluation radius, the root mean square (RMS) difference for coni in the two-dimensional parameter space $R = 5 \ldots 10$mm, $p = 0.5 \ldots 1.0$ is calculated.

6.2.3 Simulated Keratometry by OCT

As described above, only a circular area around the apex of around 1 mm in radius is characterised by the LENSTAR 900. The exact size depends on the shape of the cornea. Instead of limiting our method to measurements of this area, we fit a biconic to a larger area, incorporating the information from the periphery, and evaluate the fitted surface in

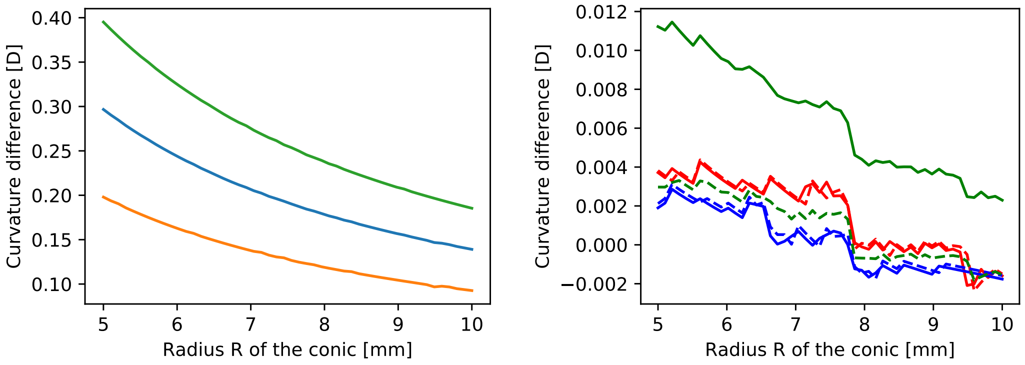

(a) (b)

Figure 6.5. (a) The difference of the simulated reference keratometry between a sphere (p=1) and an asphere with p=0.5. Middle: both rings, Top: Outer ring, Bottom: inner ring. (b) The difference between the simulated reference keratometry and the axial curvature for a sphere (dashed) and a conic ($p = 0.5$, solid). The red (blue) curves show the difference for the radial position of the outer (inner) ring. The green curves show the difference between the simulated keratometry and the axial curvature evaluated at the mean axial position of the rings. Because of the small differences in the y-axis of the figure and the scaling, the curves show fluctuations caused by numerical instabilities.

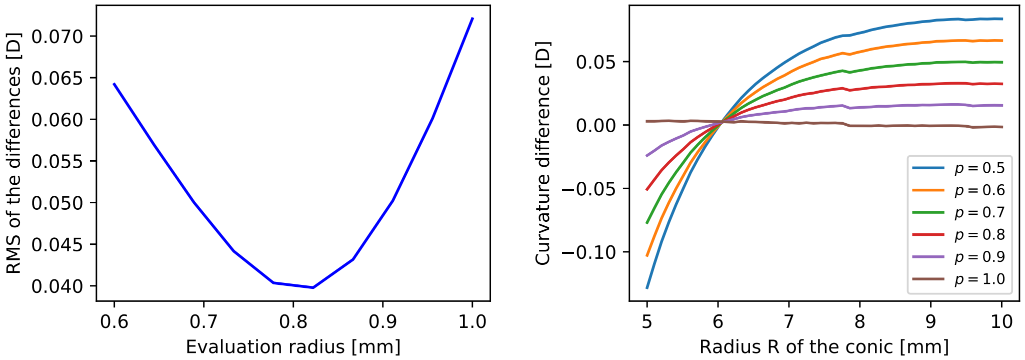

(a) (b)

Figure 6.6. (a) Evaluation radius dependent RMS difference between the axial curvature and the simulated reference keratometry over different radii (5mm to 10mm) and shape measures p (0.5 to 1.0). (b) Difference between the axial curvature and the simulated reference keratometry for a fixed evaluation radius of 0.8 mm.

the according area.

We scan a circular area with a radius of 4 mm using the loopy scan pattern described in Chapter 5. We segment the anterior corneal surface and perform a motion compensation, resulting in a motion corrected point cloud of the anterior corneal surface. Segmentation and motion compensation are also described in Chapter 5. We then fit a biconic surface to the motion corrected point cloud. To reduce the effect of eyelids, we exclude the upper part from the fit, resulting in a "rotated-D-shaped" fit area. By doing so, we keep the support of the fit similar even when the position of the eyelid changes between measurements. In order to increase the stability of the fit, we reduce the number of parameters of the biconic by only using one shape measure $p = p_x = p_y$.

Based on the relationship between biconic radius R and and the radial position r_{ref} determined in Section 6.2.2, we chose an evaluation radius of 0.8 mm. Figure 6.6b shows the simulated difference between the axial curvature with a fixed evaluation radius of 0.8 mm and the reference keratometry.

We determine the axial curvature at a distance of 0.8 mm from the apex for 360 degrees and perform a least-squares sine fit to the resulting axial curvatures. From this sine fit, we determine K_1, K_2 and the axis of the astigmatism Ast. As described in Section 6.2.2, the axial curvature at a certain position of the conic surface corresponds to the distance to the axis along the meridian normal.

For our simulated keratometry, we determined the resulting motion-compensated point cloud and performed a biconic fit as described above. Before determining the keratometry, we applied a constant correction to the biconic parameters to match the description of the cornea provided by the Pentacam. This matching is required to eliminate systematic differences that the delineation of the corneal surface by OCT bears.

6.3 Results

We evaluated the keratometry of 144 eyes of 74 patients by our simulated keratometry and two reference devices, the LENSTAR 900 and the Pentacam. Each eye was measured twice with each of the three modalities.

We converted the keratometry into the 3-dimensional dioptric space of power vectors [15]. We express two differences, the spherical power difference, corresponding to the difference in mean power Km, and the cylindrical power difference, incorporating the difference in amount and axis of astigmatism in one value.

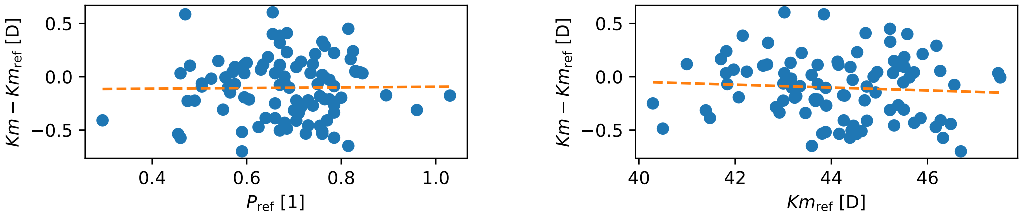

(a) (b)

Figure 6.7. Difference in mean power to the LENSTAR 900 over (a) the shape measure p of the Pentacam (orange: linear regression with correlation coefficient $r = 0.012$) and (b) the mean power of the LENSTAR 900 (orange: linear regression with $r = -0.071$).

6.3.1 In Vivo Equivalence

We compared the resulting OCT-based keratometry with the reference keratometry of the LENSTAR 900. Because the LENSTAR 900 does not provide a value for the asphericity, the asphericity provided by the pentacam is used to show the influence of the asphericity.

Figure 6.7a shows the difference in mean power over the asphericity of the eye. As can be seen, there is no correlation between the difference in keratometry and the asphericity. Figure 6.7b shows the difference in mean power over the reference mean power, again without correlation.

Figure 6.8 shows the difference in the cylinder power over the asphericity of the eye (Fig. 6.8a) and over its mean power (Fig. 6.8b). As can be seen from the scatter plots and the regressions, there is neither a correlation with the asphericity nor the mean power of the eye.

For comparison, we also determined the mean keratometry by performing a sphere fit on a 3mm-radius circle area. Figure 6.9 shows the difference in mean power. As can be seen, the differences correlate with both the asphericity and mean power of the eye.

6.3.2 In Vivo Repeatability

We calculated the repeatability of the keratometry for the mean power (Km) and the cylinder power (Cyl). The repeatability of the mean power (Km) was calculated by taking the standard deviation of the differences between the first and the second measurement.

Because the difference of the cylinder power is always positive – following a chi distribution – we defined the repeatability as the mean of the differences. Figure 6.10 shows the differences for the individual eyes. Table 6.1 shows the repeatability of our simulated keratometry as well as for the reference keratometer, the LENSTAR 900. We additionally performed Bartlett's test for equal variances of the differences in mean power, indicating statistical significance of the difference.

For the sphere fit on a 3mm-radius circle area, we determined a repeatability of the mean power (Km) of 0.19 D and a repeatability of the cylinder power (Cyl) of 0.08 D.

6.4 Discussion

The results do not show systematic deviations between our method for OCT-based simulated keratometry and the reference keratometry. In particular, the asphericity of the cornea does

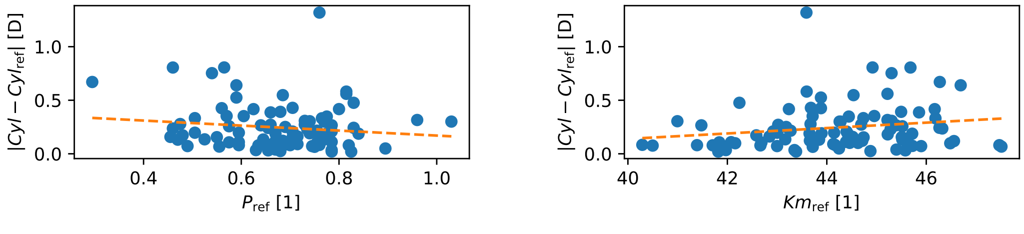

(a)

(b)

Figure 6.8. Difference in cylinder power to the LENSTAR 900 over (a) the shape measure p of the Pentacam (orange: linear regression with correlation coefficient $r = 0.13$) and (b) the mean power of the LENSTAR 900 (orange: linear regression with $r = 0.18$).

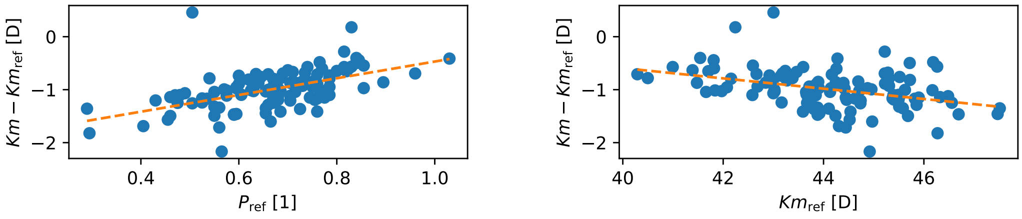

(a) (b)

Figure 6.9. Difference in mean power of a 3mm-radius sphere fit to the LENSTAR 900 over (a) the shape measure p of the Pentacam (orange: linear regression with correlation coefficient $r = 0.54$) and (b) the mean power of the LENSTAR 900 (orange: linear regression with $r = -0.381$).

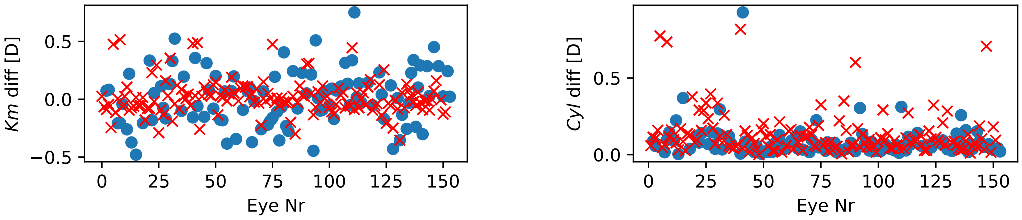

(a) (b)

Figure 6.10. The test–retest differences of the simulated keratometry (blue dots) and the LENSTAR 900 keratometry (red crosses) for the (a) mean power (Km) and (b) cylinder power (Cyl).

Table 6.1. Repeatability of our OCT-based keratometry (Sim K) and the reference keratometry of the Lenstar 900 (LS 900), and the p-value of the Bartlett's test for equal variances.

	Repeatability		
Feature	Sim K	LS 900	p-Value
Mean Power (Km) [D]	0.23	0.15	3.4e-07
Cylinder Power (Cyl) [D]	0.09	0.13	-

not induce a deviation in the keratometry.

Whereas the repeatability of the cylinder power of our method is better, the repeatability of the mean power of our method is inferior to the LENSTAR 900. Several factors influence the repeatability of the keratometry, including eye movements, the axial resolution of the system and the chosen scan pattern. We discuss the influence of the scan pattern on the repeatability in Section 7.1. Further, the improved repeatability of the keratometry by sphere fit on a 3mm-radius area indicate that there is a trade-off between repeatability and equivalency. In this trade-off we have chosen equivalency over repeatability.

References

[1] Joseph W Soper, Whitney G Sampson, and Louis J Girard. “Corneal topography, keratometry and contact lenses”. In: *Archives of Ophthalmology* 67.6 (1962), pp. 753–760.

[2] George O Waring. “Making sense of keratospeak II: proposed conventional terminology for corneal topography”. In: *Journal of Refractive Surgery* 5.6 (1989), pp. 362–367.

[3] Pier Giorgio Gobbi, Francesco Carones, and Rosario Brancato. “Keratometric index, videokeratography, and refractive surgery”. In: *Journal of Cataract & Refractive Surgery* 24.2 (1998), pp. 202–211.

[4] Maolong Tang et al. “Corneal power measurement with Fourier-domain optical coherence tomography”. In: *Journal of Cataract & Refractive Surgery* 36.12 (2010), pp. 2115–2122.

[5] Ryan P McNabb et al. “Distributed scanning volumetric SDOCT for motion corrected corneal biometry”. In: *Biomedical Optics Express* 3.9 (2012), pp. 2050–2065.

[6] Anthony N Kuo et al. “Corneal biometry from volumetric SDOCT and comparison with existing clinical modalities”. In: *Biomedical optics express* 3.6 (2012), pp. 1279–1290.

[7] Ryan P McNabb et al. “Optical coherence tomography accurately measures corneal power change from laser refractive surgery”. In: *Ophthalmology* 122.4 (2015), pp. 677–686.

[8] David Huang et al. “Optical coherence tomography–based corneal power measurement and intraocular lens power calculation following laser vision correction (an American Ophthalmological Society thesis)”. In: *Transactions of the American Ophthalmological Society* 111 (2013), pp. 34–45.

[9] Michel Guillon, Donald PM Lydon, and Christine Wilson. “Corneal topography: a clinical model”. In: *Ophthalmic and Physiological Optics* 6.1 (1986), pp. 47–56.

[10] Patricia M Kiely, George Smith, and Leo G Carney. “The mean shape of the human cornea”. In: *Optica Acta: International Journal of Optics* 29.8 (1982), pp. 1027–1040.

[11] Michiel Dubbelman, VADP Sicam, and GL Van der Heijde. “The shape of the anterior and posterior surface of the aging human cornea”. In: *Vision research* 46.6-7 (2006), pp. 993–1001.

[12] Damien Gatinel et al. “Corneal elevation topography: best fit sphere, elevation distance, asphericity, toricity and clinical implications”. In: *Cornea* 30.5 (2011), pp. 508–515.

[13] Rafael Navarro, Jos J Rozema, and Marie-José Tassignon. “Optical changes of the human cornea as a function of age”. In: *Optometry and Vision Science* 90.6 (2013), pp. 587–598.

[14] ISO-19980:2012. *Ophthalmic instruments - Corneal topographers*. Tech. rep. International Organization for Standardization, 2012.

[15] Larry N Thibos and Douglas Horner. “Power vector analysis of the optical outcome of refractive surgery”. In: *Journal of Cataract & Refractive Surgery* 27.1 (2001), pp. 80–85.

7 Discussion and Limitations

We presented methods for scanning, segmenting, motion compensating and reconstructing towards OCT-based corneal topography and keratometry. In the time after publication, the methods were applied to new measurements and developed further. In this section, we discuss the results and limitations of the presented methods, also in regard to the newest findings and latest improvements that were found and made after a first clinical trial with the device.

7.1 Scanning

We presented two scan patterns: a spiral scan pattern (Chapter 3) and a loopy scan pattern (Chapter 5). The spiral scan pattern is optimised for stable reconstruction and the loopy scan pattern is optimised for motion compensation. While the spiral scan pattern enables stable reconstruction from partial scans, we identified limitations regarding motion compensation with high temporal resolution. The loopy scan pattern improves motion compensation with a high temporal resolution by fast scanning and a high number of intersections. However, it lacks advantages of the spiral scan pattern, namely the close to uniform scan point distribution and the golden angle refining. For the future, we desire a scan pattern that combines the advantages of both scan patterns, having fast scanning, a high number of intersections, uniform scanning and golden-angle based refining.

Currently, we prefer the loopy scan pattern over the spiral scan pattern for corneal topography and keratometry. The choice to use the loopy scan pattern is based on a comparison of the scan patterns. We compared the performance of the two scan patterns regarding the repeatability of the simulated keratometry. For completeness, we also included a radial scan pattern into the comparison. Although the comparison is based on only 20 eyes and was done with early versions of the reconstruction and keratometry, we believe that the results in Table 7.1 are valid to judge the scan patterns in terms of their general suitability. The results show that the loopy scan pattern leads to better general repeatability compared to the spiral scan pattern. The possible causes for this behaviour are manifold and ask for further research.

However, there are some speculations as for the observed behaviour. One conjecture is

Table 7.1. *In vivo* scan-rescan repeatability of the OCT-based keratometry for different scan patterns. The scan-rescan repeatability is defined by the standard deviation of the scan-rescan differences.

	Scan Pattern		
Feature	Spiral	Loopy	Radial
Mean K (Km) [D]	0.23	0.16	0.14
Astigmatism (Ast) [D]	0.17	0.18	0.24

that the difference between the scan patterns is linked to the different primary scan directions. The spiral scan pattern has a primarily circumferential scan trajectory. Therefore, astigmatism is sampled quickly whereas radial curvature takes longer to determine. The radial scan pattern scans primarily along meridians. Therefore, the radial curvature is sampled quickly whereas astigmatism takes longer to determine. The loopy scan pattern features a primary scan direction that is somewhere in between.

7.2 Segmentation

The presented segmentation method enables robust segmentation of the corneal surfaces in scans that are acquired by two-dimensional scan patterns like the spiral scan pattern (Chapter 3) or the loopy scan pattern (Chapter 5).

Nevertheless, we identified some limitations and partially modified the segmentation method to increase its robustness.

Motion compensation during segmentation To increase the robustness against motion, we included motion compensation in the segmentation model for the fine segmentation. Without this measure, motion could lead to false fine segmentation because the segmentation feature is not in the region of interest (ROI) of the segmentation.

Robust segmentation to handle eyes of older patients Further, we modified the segmentation method to handle some eyes of older patients. While the presented segmentation scheme worked fine for young eyes, it failed for some older eyes because of a strong second interface behind the actual air-cornea interface. This led to sporadic false segmentations as shown in Figure 7.1. To overcome this problem, we introduced a preprocessing for more robust segmentation in order to favour signals that are closer to the measurement system. We changed the original two-step coarse-fine segmentation scheme to a three-step segmentation, including a robust coarse segmentation, a robust fine segmentation and a final fine segmentation with the original preprocessing. The final segmentation is still done with the original preprocessing because the robust preprocessing leads to systematic changes in the segmentation, which we want to avoid. The ROI for the final segmentation is created from the robust fine segmentation, using the segmentation itself instead of a Zernike model – allowing a more narrow ROI.

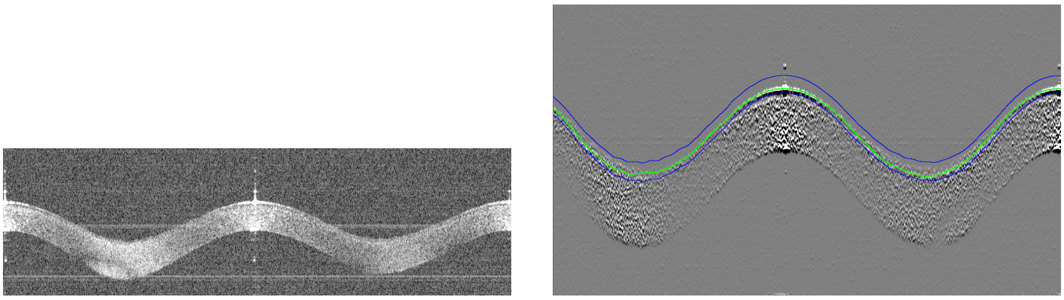
(a) (b)

Figure 7.1. OCT-image section of a cornea with a second interface (a) and the resulting false segmentation in green (b) on the oversampled gradient image.

More sophisticated eyelid detection An accurate eyelid detection prior to the segmentation is essential for the success of the segmentation and later reconstruction. It turned out, that the original eyelid detected failed in some cases. We, therefore, changed the eyelid detection from the described centre-of-mass based approach to a more sophisticated method featuring fast segmentation and a RANSAC Zernike fit.

Increased oversampling for phantom segmentation For the segmentation of phantoms, we increased the oversampling because we observed discretisation effects. In the most recent version of the phantom segmentation, we incorporated a refinement of the graph-based segmentation result by local Gaussian fits - eliminating the observed discretisation effects. The investigation of the effect of increased oversampling and refinement on the *in vivo* performance did not show any improvements. We assume that this is mainly due to the fact, that *in vivo* measurements underlie motion which reduces the effect of discretisation.

No use of the continuous piecewise segmentation scheme We did not use the piecewise segmentation that we presented in the original work (Chapter 4). Instead, we segmented each chunk separately, which reduced the complexity of the segmentation and reduced the dependencies between the chunks. The resulting discontinuities between the chunks turned out to be negligible for our purpose.

Limited applicability for lens segmentation In the future, the segmentation of the lens would bear potential to improve the IOL-selection (see Chapter 8). While the presented segmentation method works fine for the segmentation of the anterior and posterior corneal surfaces, there are limitations for its application on the lens surfaces. While we successfully applied the presented method to the anterior lens surface, the segmentation of the posterior lens surface often failed. The signal of the posterior lens surface can be fragile and tends to vanish, leading to failure of the segmentation.

Therefore, we propose to adopt the segmentation method for the segmentation of the lens. Because we can detect and compensate the motion, we have the possibility to generate motion free measurements. Instead of segmenting the lens directly in scans, a real three-dimensional segmentation on the motion-corrected measurement could provide some gain in robustness. Another approach might be the use of maximum intensity projection to generate B-scans with enhanced signal strength for segmentation.

7.3 Motion Compensation

We presented a method that enables motion compensation in three dimensions by incorporating a motion model. Results show that motion compensation minimises the effect of motion. The measurements of moving phantoms even indicate that the effect of motion on the topography is negligible after motion compensation. However, we believe that the explicit handling of saccades bears the potential to increase the performance of the motion compensation. In the presented method, saccades are only addressed indirectly by excluding chunks that worsen the overall reconstruction. The explicit detection and handling of saccades would maximise the amount of scan data that can be used for reconstruction – given that this is also done during segmentation.

We further observed that the relatively high order of the motion polynomials can lead to oscillations in the motion compensation. Although no negative impact on the measurement performance was observed so far, we recommend optimising the order of the motion polynomials and the size of the motion compensation chunks to reduce the amount of overshooting. Together with a saccade detection, a dynamic chunk size could be beneficial. We therefore

Table 7.2. Intra-examination and inter-examination repeatability of the OCT-based keratometry. The scan-rescan repeatability is defined by the standard deviation of the scan-rescan differences.

	Repeatability			
	inter-measurement			intra-measurement
Feature	4 frames	1st frame	3rd frame	1st vs 4rd frame
Mean K (Km) [D]	0.252	0.274	0.301	0.143
Astigmatism (Ast) [D]	0.129	0.159	0.166	0.108
Shape measure $p(p)$ [1]	0.101	0.11	0.115	0.071

suggest a more sophisticated motion compensation scheme including saccade detection and dynamical splitting of the measurement in chunks where the saccades are excluded.

7.4 Reconstruction

The regularised Zernike reconstruction presented in Chapter 5 is meaningful because Zernike polynomials are established and represent aberrations ordered by their relevance. We addressed one drawback, the instability in curvature space, by appropriate regularisation. However, we identified another major drawback of Zernike reconstruction, namely that local distortions, e.g. by eyelids, influence the entire reconstruction. A more local description of the cornea could be introduced to enable the mapping of local deviations – either to replace or to expand the Zernike reconstruction.

Because it turned out that the scanning system suffers from temperature effects that cannot be compensated with ease, each measurement has to be compensated by an additional measurement of a reference phantom with known dimensions. This not only increases the total time of the data acquisition but also adds the uncertainty of the phantom fit to the result. A more stable scanner or even a closed loop scanner could further increase the repeatability of the measurement.

7.5 Corneal Topography and Keratometry

Based on the methods for scanning, segmentation and Zernike reconstruction, we presented corneal topography and keratometry by OCT. We showed that the presented OCT-based corneal topography is comparable with established topographers.

However, the repeatability of the presented keratometry does not reach the level of the reference keratometer. To investigate the limiting factors for the repeatability, we assessed the intra-measurement repeatability and compared it to the inter-measurement repeatability. The intra-measurement repeatability was determined between the first and the fourth frame of the same measurement – by only segmenting and reconstructing the according frame of the measurement. The inter-measurement repeatability was determined between the same parts of repeated measurements of the same eye.

The comparison in Table 7.2 shows that the intra-measurement repeatability is better than the inter-measurement repeatability, even when using all four frames for the determination of the inter-measurement repeatability. Assuming that eye motion and segmentation are independent between the first and the third frame, this implies that they are not the limiting factor for the inter-measurement repeatability.

Further, the improvement of the repeatability with increased frame number is not as high as we would expect from statistics. Assuming the keratometry for each frame to be independent from each other with the same standard deviation of K_m, we calculate the expected standard deviation of K_m for four frames by the standard error of the mean σ_M defined by

$$\sigma_M = \frac{\sigma}{\sqrt{N}}\,, \tag{7.1}$$

where σ is the standard deviation of K_m for one frame and N is the number of frames. The expected standard deviation of the mean of four frames is therefore expected to be half of the standard deviation of one frame.

We calculate repeatability by the standard deviation of the scan-rescan differences. Assuming a normal distribution from which values are taken to calculate pair-wise differences, the variance of the difference distribution is two times the variance of the underlying distribution. This results in a repeatability that is $\sqrt{2}$ times the standard deviation of the underlying distribution. Thus, the repeatability for four frames is also expected to be around half the repeatability of one frame. As this is not the case, the assumption of independence between the frames is not valid. Therefore, there has to be a yet to be defined effect that depends on the measurement itself, degrading the repeatability of the keratometry.

We identified several parameters that are measurement dependent, including the alignment of the eye and the eye-opening. Analysis has not shown any correlation between the repeatability and the alignment or eye-opening. The effect of the eye-opening is already minimised by excluding the top section of the measurement from keratometry. The alignment of the eye has shown to be very repeatable, well below 100 µm which is even below the expected lateral movement during measurement. The investigation of the influence on the inter-measurement repeatability is still ongoing.

In the publications, we only presented anterior corneal topography. We further generated topography maps of the posterior corneal surface and also determined the posterior keratometry analogue to the anterior keratometry. The curvature of the posterior corneal surface can be used for more sophisticated IOL-selection. The results confirmed the applicability of the methods to the posterior corneal surface, showing good repeatability and equivalency compared to reference posterior corneal topography and keratometry (Pentacam).

8 Conclusion and Outlook

We developed and presented new methods to enable OCT-based corneal topography and keratometry – using an OCT system with a limited axial resolution, scan rate and scanner dynamics. This includes new methods for scanning, segmentation, motion-compensation and reconstruction. We introduced two continuous, two-dimensional scan patterns: a spiral scan pattern that enables numerically robust reconstruction from fractional scans and a loopy scan pattern that enables motion compensation with high temporal resolution. We also introduced a model-based segmentation method, enabling robust segmentation of scans that were acquired using two-dimensional scan patterns. We further developed a three-dimensional, model-based motion compensation with high temporal resolution and presented methods for robust reconstruction, topography and keratometry.

The resulting pipeline was verified by phantom measurements and *in vivo* measurements. The results indicate that the eye motion no longer limits the repeatability of the resulting topography and keratometry. The comparison between intra- and inter-examination repeatability indicates that other effects limit the repeatability, *e.g.* temperature effects or the repeatability of the scanning itself. The identification and understanding of these effects are essential to improve the performance further and ask for further research. We want to point out that the presented methods can be applied to systems with higher resolution and speed with ease.

Apart from the presented work, the three-dimensional measurement of the eye over its entire length bears the potential for future work. Based on the presented motion compensation it is possible to generate motion-free volumes, *e.g.* for visualisation and as a basis for further 3-D image processing. Because we are able to reconstruct both the anterior and posterior corneal surface, the calculation of so-called total corneal power maps should be straightforward. For this work, we limited our research to the corneal surfaces. In future work, we will expand our efforts to the quantitative measurement of the lens. The quantitative measurement of the lens would allow for the simulation of the refractive power by ray-tracing and for more precise IOL selection. However, the segmentation of the lens asks for an adaptation of segmentation methods because the lens has a meagre signal-to-noise ratio in the OCT scans. Further, the automatic detection of pathologies and the generation of other measures like anterior chamber angle have to be addressed.

Appendix

Patent US 10,201,271 B2

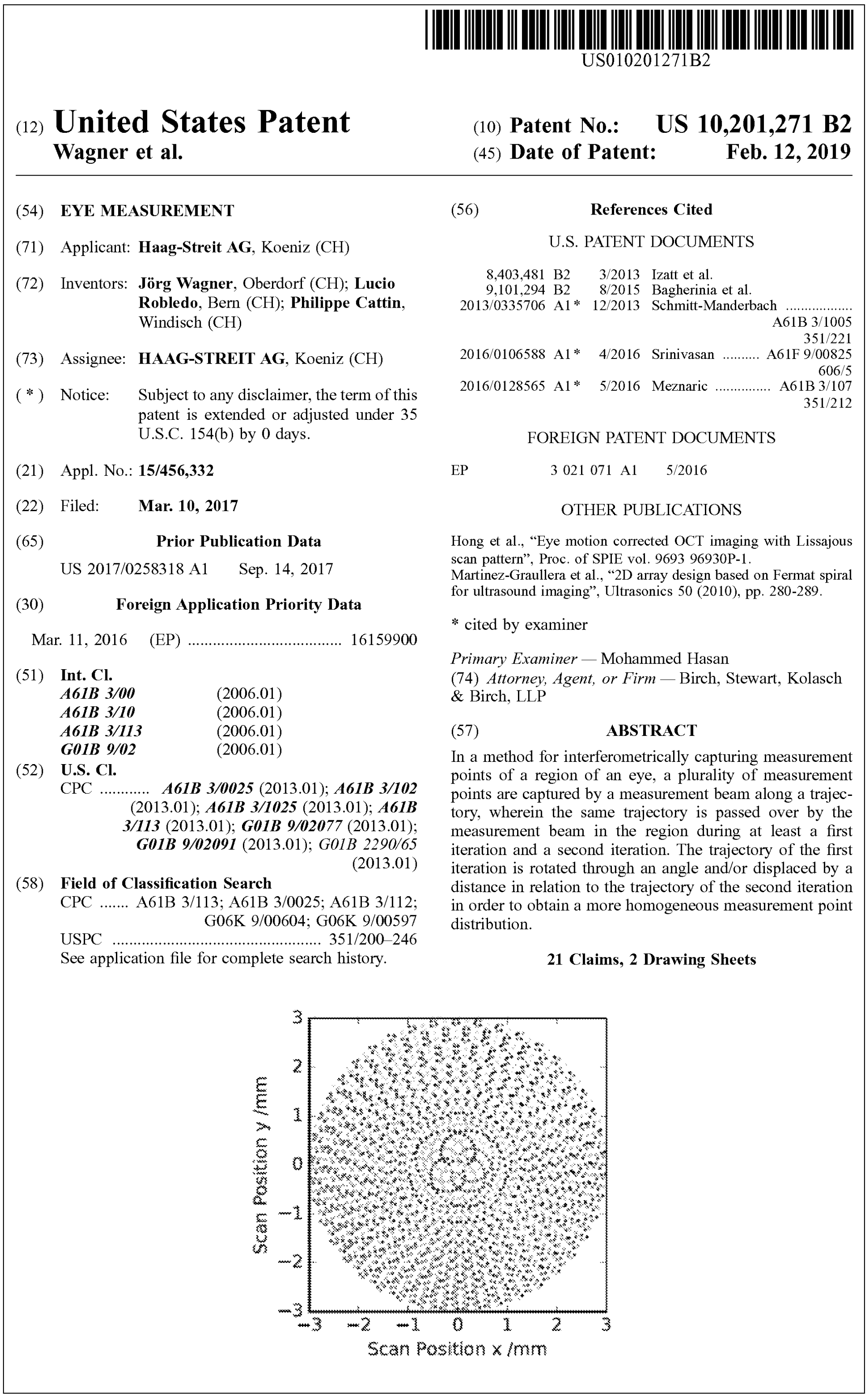

US010201271B2

(12) **United States Patent**
Wagner et al.

(10) **Patent No.: US 10,201,271 B2**
(45) **Date of Patent: Feb. 12, 2019**

(54) **EYE MEASUREMENT**

(71) Applicant: **Haag-Streit AG**, Koeniz (CH)

(72) Inventors: **Jörg Wagner**, Oberdorf (CH); **Lucio Robledo**, Bern (CH); **Philippe Cattin**, Windisch (CH)

(73) Assignee: **HAAG-STREIT AG**, Koeniz (CH)

(*) Notice: Subject to any disclaimer, the term of this patent is extended or adjusted under 35 U.S.C. 154(b) by 0 days.

(21) Appl. No.: **15/456,332**

(22) Filed: **Mar. 10, 2017**

(65) **Prior Publication Data**

US 2017/0258318 A1 Sep. 14, 2017

(30) **Foreign Application Priority Data**

Mar. 11, 2016 (EP) 16159900

(51) **Int. Cl.**

A61B 3/00	(2006.01)
A61B 3/10	(2006.01)
A61B 3/113	(2006.01)
G01B 9/02	(2006.01)

(52) **U.S. Cl.**
CPC ***A61B 3/0025*** (2013.01); ***A61B 3/102*** (2013.01); ***A61B 3/1025*** (2013.01); ***A61B 3/113*** (2013.01); ***G01B 9/02077*** (2013.01); ***G01B 9/02091*** (2013.01); *G01B 2290/65* (2013.01)

(58) **Field of Classification Search**
CPC A61B 3/113; A61B 3/0025; A61B 3/112; G06K 9/00604; G06K 9/00597
USPC 351/200–246
See application file for complete search history.

(56) **References Cited**

U.S. PATENT DOCUMENTS

8,403,481	B2	3/2013	Izatt et al.	
9,101,294	B2	8/2015	Bagherinia et al.	
2013/0335706	A1 *	12/2013	Schmitt-Manderbach	A61B 3/1005 351/221
2016/0106588	A1 *	4/2016	Srinivasan	A61F 9/00825 606/5
2016/0128565	A1 *	5/2016	Meznaric	A61B 3/107 351/212

FOREIGN PATENT DOCUMENTS

EP 3 021 071 A1 5/2016

OTHER PUBLICATIONS

Hong et al., "Eye motion corrected OCT imaging with Lissajous scan pattern", Proc. of SPIE vol. 9693 96930P-1.
Martinez-Graullera et al., "2D array design based on Fermat spiral for ultrasound imaging", Ultrasonics 50 (2010), pp. 280-289.

* cited by examiner

Primary Examiner — Mohammed Hasan
(74) *Attorney, Agent, or Firm* — Birch, Stewart, Kolasch & Birch, LLP

(57) **ABSTRACT**

In a method for interferometrically capturing measurement points of a region of an eye, a plurality of measurement points are captured by a measurement beam along a trajectory, wherein the same trajectory is passed over by the measurement beam in the region during at least a first iteration and a second iteration. The trajectory of the first iteration is rotated through an angle and/or displaced by a distance in relation to the trajectory of the second iteration in order to obtain a more homogeneous measurement point distribution.

21 Claims, 2 Drawing Sheets

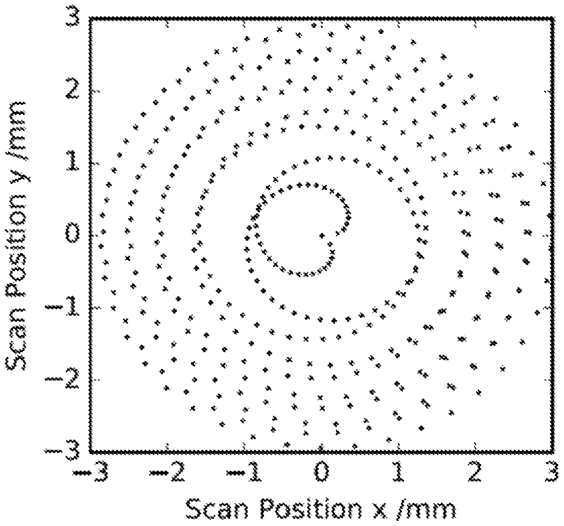
3
2
1
0
−1
−2
−3
Scan Position y /mm
−3
−2
−1
0
1
2
3
Scan Position x /mm

Fig. 1

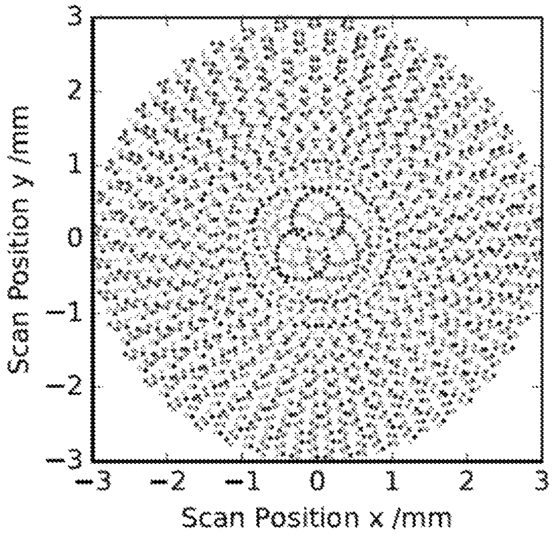
3
2
1
0
−1
−2
−3
Scan Position y /mm
−3
−2
−1
0
1
2
3
Scan Position x /mm

Fig. 2

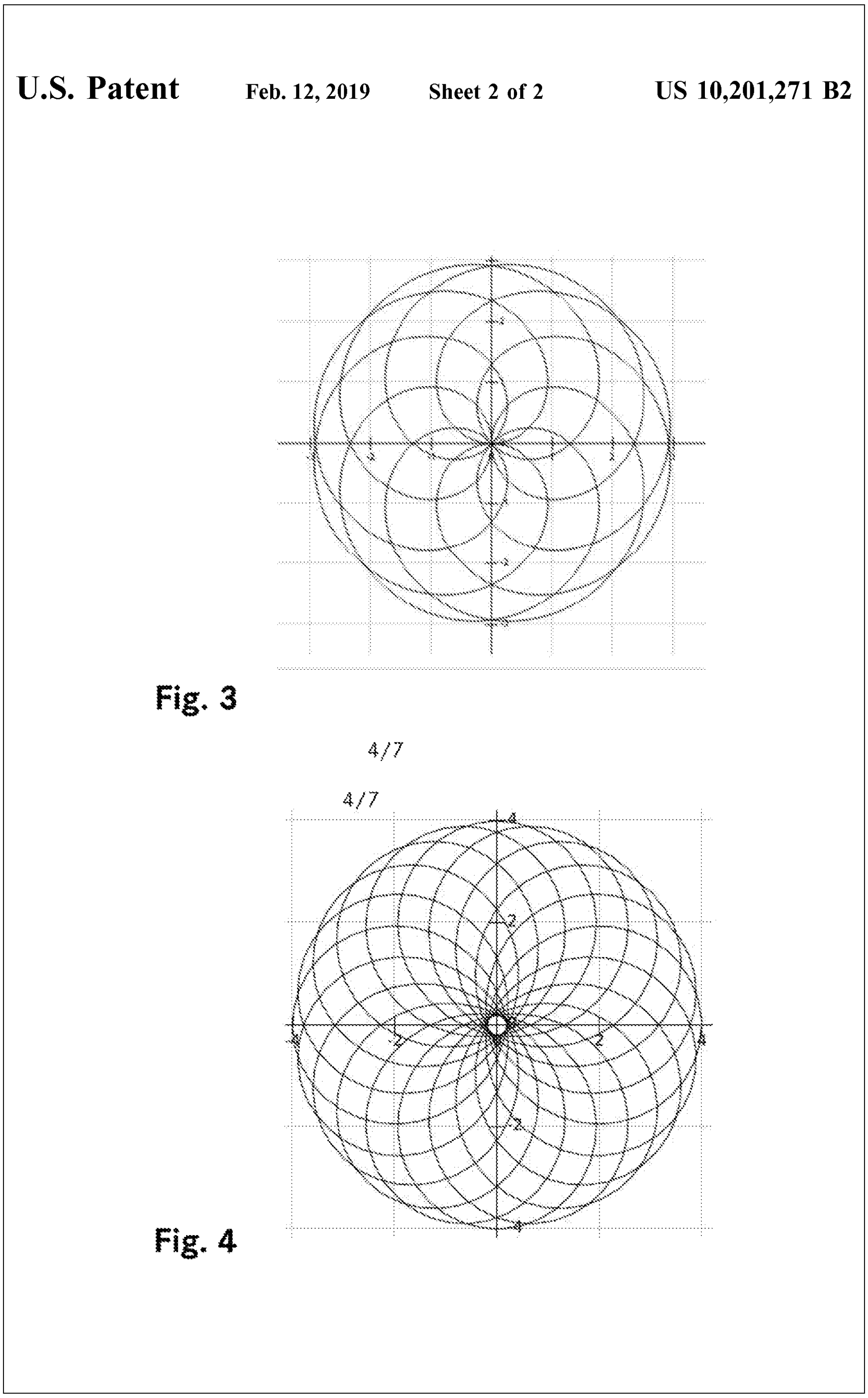

U.S. Patent Feb. 12, 2019 Sheet 2 of 2 US 10,201,271 B2

Fig. 3

4/7

4/7

Fig. 4

EYE MEASUREMENT

TECHNICAL FIELD

The invention relates to a method for interferometrically capturing measurement points of a region of an eye, wherein a plurality of measurement points are captured by a measurement beam along a trajectory, wherein the same trajectory is passed over by the measurement beam in the region during at least a first iteration and a second iteration. Further, the invention relates to an apparatus for carrying out the method.

BACKGROUND OF THE INVENTION

Prior Art

The present invention relates to the interferometric capture of measurement points on a region of an eye.

Corresponding methods and apparatuses are known in ophthalmology. Typically, an interferometer is used to carry out such examinations of the eye. By way of example, OCT (optical coherence tomography) scanners are used as interferometers; these scan the eye at discrete positions in the lateral direction and, in the process, capture stray-light profiles (axial profiles) of the eye along the optical beam. On account of the axial profiles, it is possible to define three-dimensional measurement points in the eye, which preferably represent one or more optical surfaces.

By way of example, Zeiss (U.S. Pat. No. 9,101,294 B2) discloses a method for processing data from an OCT device, wherein an increase in the precision of the calculation of ocular measurements is intended to be achieved by different approaches. The methods comprise novel scanning patterns, the use of techniques for determining the transversal eye movement and an improved algorithm for eye movement correction.

In particular, the method comprises capturing a first small set of data by means of OCT and using the data to model the cornea. The model is subsequently used to create a precise, movement-corrected model during a further measurement with a more dense number of measurement points.

Further, Duke (U.S. Pat. No. 8,403,481 B2) discloses a method for reducing movement artifacts in OCT measurements. In the method, data are ascertained using a scanning pattern, said data being distributed in such a way that at least certain spatially adjacent data points were not ascertained in sequence. To this end, use can be made of a scanning pattern in which spatially adjacent data points are ascertained in non-sequential fashion. By way of example, the sample may be scanned by a number of series of scanning lines, with some of the scanning lines lying between previously measured scanning lines.

Essential requirements of the measurement, particularly when measuring the eye, are, firstly, a short overall duration of the measurement and a high resolution, i.e. a large coverage of the area to be measured. The short overall duration is an essential criterion, in particular on account of the unavoidable movements of the eye during the measurement.

The known methods are disadvantageous in that the measurements take a relatively long time. On account of the relatively long measurement duration, there is an increased risk of the measurement results being influenced by eye movements of the patient, as a result of which only inaccurate measurement results are able to be obtained.

SUMMARY OF THE INVENTION

It is an object of the invention to develop a method for interferometrically capturing measurement points on a region of an eye, which facilitates a particularly precise measurement of the eye, said method belonging to the technical field set forth at the outset, wherein, in particular, eye movements may be corrected in a particularly ideal manner.

The solution to the object is defined by the features of claim **1**. In accordance with the invention, the trajectory of the first iteration is rotated through an angle and/or displaced by a distance in relation to the trajectory of the second iteration in order to obtain a more homogeneous measurement point distribution.

The object according to the invention is likewise achieved by an apparatus for carrying out such a method.

In principle, a distance measurement, in particular an axial distance measurement in the Z-direction (see below), particularly preferably an axial scattering profile (a so-called A-scan) along the beam direction forms the basis of the measurement method. The measurement points are preferably captured by means of spectral domain OCT (SD-OCT) or swept source OCT (SS-OCT), preferably with a temporally constant frequency. Methods using OCT have become established in ophthalmology as these may be used in scattering objects such as an eye and, in particular, have a relatively high penetration depth with, at the same time, a high axial resolution.

Different optical frequencies are used in SD-OCT. The light is dispersed and analyzed by means of a CCD or CMOS sensor. Using this, the full measurement depth may be achieved by a single measurement. By contrast, the optical frequency is periodically tuned in SS-OCT and the interference signal is measured resolved in time. These techniques are sufficiently well known to a person skilled in the art.

Distances may be captured by peak detection in the A-scan, edge detection in the A-scan or by a segmentation of sequentially captured A-scans.

In variants, use may also be made of other techniques for the point distance measurement or for the axial profile measurement (capturing of A-scans) (see interferometer), for example a time-of-flight measurement by means of a laser or the like.

Below, X, Y and Z-coordinates are used as a three-dimensional orthogonal system. The trajectory is preferably considered along an XY-plane and the measurement beam has the Z-direction in at least one measurement direction, in particular in the direction of a midpoint of the region. From this position, the measurement beam may either be displaced in parallel, i.e. maintaining the Z-direction, or else be swiveled through an angle in the X-direction and a second angle in the Y-direction. Furthermore, the change in position may also be achieved by a combination of these variants. Provided nothing else is mentioned, the preferred first variant is assumed below, without there being a restriction to one of the variants. To this end, provision may be made of telecentric optical units, in which a beam offset may be in parallel. The distance measurement relates to the Z-axis or the direction of the measurement beam, wherein changes in the refractive index along the measurement axis may lead to refractive effects, which could lead to changes in the direction and scaling of the axial scattering profile. Methods for geometric correction and conversion of the measured lengths are known to a person skilled in the art.

The trajectory is respectively understood to be a plane projection in an XY-plane, which intersects the eye to be measured or which has a small distance from the eye to be measured. In practice, the trajectory may deviate from this description depending on the eye to be measured. By way of example, if points are captured along a trajectory at regular intervals by means of the measurement beam, these points are only at a constant distance from one another in the measurement region if the measurement region is a plane parallel to the plane projection. However, if this trajectory is projected onto an eye, temporally successive measurement points near the center lie closer to one another than temporally successive measurement points in the edge region of the eye.

An axial length profile or A-scan should be understood to mean a profile of the eye along the z-axis or the beam direction. A B-scan is understood to mean an axial profile along a straight section through the eye, which is composed of individual A-scans. The axial length profiles may be combined to form a three-dimensional model of the eye or a section through the eye. However, the data may also be used differently, for example for simulating a beam path, a correction lens or the like.

Below, the region of the eye need not necessarily be understood to mean the surface of the cornea but, in particular, may also be understood to be a three-dimensional region. Thus, depth profiles of the eye may be created with the aid of OCT methods, which equally fall under the term "region" below.

The degree of coverage is the proportion of the area to be measured in which the distance from any point to the closest measurement point does not exceed a critical value. For measurements of the topography of the eye, a degree of coverage of 100% is usually required, wherein the area to be measured should have at least a diameter of 7.5 mm and the critical distance should be 0.5 mm. However, depending on the requirements, it is also possible to use lower degrees of coverage or smaller measurement areas, for example when realizing shorter measurement times. The areas and distances relate to the XY-plane in which the trajectory is defined.

The more homogeneous measurement point distribution is understood to mean an increased degree of coverage when compared with a second iteration without rotation or displacement of the trajectory. Hence, the more homogeneous measurement point distribution is obtained, in particular, if at least one measurement point of the second iteration does not come to rest on a measurement point of the first iteration.

Below, the trajectory is defined in relation to the XY-plane as a two-dimensional curve should nothing else be specified. However, it is clear to a person skilled in the art that the trajectory typically represents a three-dimensional spatial curve which is distorted in relation to the trajectory when applied as a projection onto a body. However, since this spatial curve depends both on the trajectory form and on the body form and therefore is able to vary over a large range, this is not discussed in any more detail. Moreover, the trajectory need not necessarily follow a function or definition in a mathematically exact manner. Preferably, the trajectory has a form which lies on the above-described trajectory, or on one of the above-described trajectories, for at least the individual measurement points. In this case, the functions or the forms are ultimately only defined by an interpolation of the measurement points. In practice, the measurement points may, however, also deviate slightly from the trajectory. Depending on the number of measurement points and size of the object, the mean deviation from the trajectory may e.g. be less than 5%, preferably less than 1%, of the diameter of the circumference of the area to be measured.

Below, an iteration is understood to mean the capture of measurement points on the trajectory, with the trajectory being passed over exactly once in the entirety thereof. Instead of the term "iteration", use is also made of the equivalent term "cycle".

The rotation and/or displacement of the trajectory should be understood to the effect that at least one point of the trajectory of the first iteration does not correspond to the trajectory of the second iteration. Preferably, at least one measurement point on the trajectory of the first iteration does not correspond to a measurement point on the trajectory of the second iteration. Particularly preferably, the trajectory of the first iteration only intersects the trajectory of the second iteration such that no two adjacent measurement points are captured by the trajectory of the first iteration and the trajectory of the second iteration. The rotation and/or displacement of the trajectory should be understood as a relative movement between the trajectory and the eye.

The rotation and/or displacement of the trajectory should further be interpreted to the effect that one of the following options is present:

only a rotation of the trajectory; or
only a displacement of the trajectory; or
a combination between a rotation and a displacement of the trajectory.

The rotation of the trajectory is understood to mean a rotation of the trajectory about the axis of rotation parallel to the Z-axis, with the axis of rotation preferably extending through a midpoint of the trajectory. Here, the midpoint of the trajectory can be defined in different ways. By way of example, the midpoint may be defined as start or endpoint of the trajectory in relation to an iteration. On the other hand, the midpoint of the trajectory may also be defined as midpoint of a circumference of the trajectory. Particularly preferably, the midpoint lies approximately on the apex, a vector of symmetry or an optical axis of the eye.

The displacement of the trajectory is understood to mean a lateral displacement of the trajectory in the XY-plane.

According to the invention, the trajectory of the first iteration is rotated through an angle and/or displaced by a distance in relation to the trajectory of the second iteration in order to obtain a more homogeneous measurement point distribution. The more homogeneous measurement point distribution is achieved by virtue of at least one measurement point of the second iteration not lying on a measurement point of the first iteration as a result of the rotation or displacement of the trajectory. Particularly preferably, the two trajectories of the first iteration and the second iteration do not have any common adjacent measurement points such that the trajectories only coincide in the form of points of intersection. Hence, a scattering of the measuring points is further increased as a result of the rotation or the displacement.

Since, according to the invention, exactly one trajectory may be used to obtain a more homogeneous measurement point distribution, a particularly simple method for capturing measurement points on an eye is developed, said method moreover also being particularly advantageous in terms of evaluating the measurement data.

Preferably, any straight line extending within the trajectory intersects the trajectory at at least two spaced apart points. Hence, a trajectory which, per se, already has a good measurement point distribution is obtained.

Alternatively, use could also be made of trajectories which are intersected merely at one point by such a straight line.

In the case of a particularly advantageous embodiment of the method, the trajectory is embodied in such a way that:

- the measurement point distances have a particularly ideal distribution in the radial direction, in particular in relation to the point of rotation of the trajectory, in the case of a rotation of the trajectory;
- the measurement points have a particularly ideal distribution, in particular in a direction crossing the displacement direction, in the case of a displacement of the trajectory.

In the case of a combined movement of the trajectory by way of rotation and displacement, the measurement point distribution of the trajectory may be selected in such a way that the respective contributions of the rotation and of the displacement are taken into account accordingly. By way of example, to the extent that the rotational proportion is large, a homogeneous measurement point distribution may be weighted more in the radial direction, and vice versa.

However, the measurement point distribution on the trajectory may also be largely ignored in variants.

Preferably, an initial point of the second trajectory corresponds to the endpoint of the first trajectory. This allows the measurement method to be carried out continuously, i.e. without jumps. Using this, a continuous measurement, for example with a temporally constant interval, may be carried out with the interferometer. By way of example, this may be achieved by virtue of the same point being selected as initial point and endpoint in each case. By way of example, it may lie at the center of the region.

In variants, it is also possible that the initial point of the second trajectory does not correspond to the endpoint of the first trajectory.

Preferably, the trajectory covers the region. The term “covering” is understood to mean that the region is a portion of the area bounded by the circumference around the trajectory. This already allows substantial measurement of the eye in this region, albeit with a relatively low measurement point density under certain circumstances, during the first iteration of the trajectory. This is advantageous, in particular, if certain conclusions should already be drawn after the first iteration, in particular, for example, if the eye should be localized relative to the measurement appliance.

In variants, the trajectory may also have such a design that it does not cover the region. In this case, the trajectory may e.g. be created in such a way that the region is covered after the second iteration in the case of a suitable rotation and/or displacement. However, the trajectory may also be designed in such a way that coverage is only achieved after more than two iterations, for example after more than 3, 5, 10 iterations.

Preferably, the trajectory is continuously rotated through an angle and/or displaced by a distance. The continuous movement of the trajectory, i.e. the continuous rotation and/or displacement, is advantageous in that the measurement method need not be interrupted during the movement of the trajectory. Hence, the measurement method may be carried out without interruption, facilitating a particularly quick and efficient measurement of an eye. Here, the speed of the measurement is of great interest since this allows movement artifacts of the eye during the measurement to be minimized. Further, it is possible to avoid the case where a discontinuity or a smaller movement radius, which may have a negative influence on the measurement speed, arises in the transition between the iterations. It is thus possible to largely avoid a reduced curve radius with a negative effect on the measurement speed as a result of the continuous or smooth movement of the trajectory during the measurement process.

In variants, the rotation and/or the displacement of the trajectory may also take place between the iterations in each case. In this case, it is particularly advantageous if the initial point of the second iteration and the endpoint of the first iteration correspond and, for example, lie at the center of the trajectory or the region.

In a preferred embodiment, the trajectory of the second iteration is rotated through an angle and/or displaced by a distance in relation to the trajectory of the first iteration only on account of a movement of the eye, as a result of which a more homogeneous measurement point distribution is obtained. A particularly simple measurement method is obtained thus as it is not the trajectory but the eye which is moved. Here, the movement of the eye is preferably the movement of the eye of the subject during the measurement, which typically is not preventable. Minimal movements of the eye are unavoidable, even though the subject e.g. rests his chin during the measurement and presses the forehead against a further support. In these movements, a distinction is made between axial movements (in the Z-axis) and lateral movement (in the XY-plane). The axial movement of the cornea typically lies in a region of 100-200 μm. As a rule, the axial movement tends to be slow and substantially caused by the pulse. The lateral movement of the cornea likewise typically lies in a region of 100-200 μm. The lateral movement consists in approximately equal parts of very small rotations of the eye (slow drift, fast microsaccades, etc.) and lateral head movements. The lateral head movements tend to be slower than the rotations, but have a similar amplitude. These specifications relate to natural movements which cannot be influenced by an ideal subject, i.e. the specifications above tend to lie in the lower range of movements to be expected. In practice, the movements may also be more pronounced. In a particularly preferred method, the trajectory is only rotated and/or displaced on account of the natural eye movement. However, the eye may also be actively moved in a further embodiment, e.g. by virtue of the holder of the head of the subject being moved or by virtue of a fixation light or the like for the eye of the subject being moved. Using this, the movement of the eye may also be influenced actively and a more homogeneous measurement point distribution may possibly be achieved.

In a particularly preferred variant, the movements are actively obtained by the measurement appliance, with the measurement beam being controlled in such a way that the trajectory of the second iteration is rotated through an angle and/or displaced by a distance in relation to the trajectory of the first iteration.

Preferably, the trajectory is rotated through an angle of m*360°/n after each iteration, where m, n≥2 and m≠n. Here, m and n are natural numbers and m is preferably greater than 0. Further, the quotient m/n should trivially be selected between 0 and 1. Preferably, the angle is selected in such a way and the trajectory is fitted in such a way that measurement points which were not captured in the preceding iteration or the preceding iterations are captured in each iteration. This obtains a particularly ideal measurement point density, as a result of which a particularly precise measurement of the eye is obtained in turn. Particularly preferably, the quotient m/n is greater than 0.01, further preferably greater than 0.1, particularly preferably greater than 0.2. As a result of this, the rotated trajectories already obtain a largely regular measurement point distribution after as few iterations as possible. In the case of a quotient of m/n=0.2, the largely regular measurement point distribution would be achieved after e.g. 5 iterations. In the case of a quotient of m/n=0.375, this is already achieved after approximately 3 iterations. In a further advantageous configuration, m/n is selected in such a way that k*m/n is only an integer for large k, where k is a natural number. This further allows a largely regular measurement point distribution to be able to be obtained after a small number of iterations with, however, the identity of the trajectory only being obtained after a large number of iterations. In the example with m/n=0.375, a largely regular measurement point distribution is already achieved after approximately 3 iterations, whereas the identity is only achieved after 8 iterations. Hence, in a preferred method, m and n are co-prime, i.e. GCD(m, n)=1, as a result of which the identity is obtained after n iterations, while a largely regular measurement point distribution is already obtained after

$$\left\lceil \frac{n}{m} \right\rceil$$

(n/m rounded up) iterations. By way of example, the value m/n may further be 4/9, 5/9, 7/15, 7/16, 49/128, etc.

In variants, it is also possible to dispense with the rotation of the trajectory. In this case, the trajectory may, for example, only be displaced.

Preferably, the trajectory after the second iteration in relation to the first iteration is rotated through an angle between

$$360*0.9*\left(\frac{3-\sqrt{5}}{2}\right)^{\circ} \text{ and } 360*1.1*\left(\frac{3-\sqrt{5}}{2}\right)^{\circ},$$

preferably between

$$360*0.95*\left(\frac{3-\sqrt{5}}{2}\right)^{\circ} \text{ and } 360*1.05*\left(\frac{3-\sqrt{5}}{2}\right)^{\circ},$$

particularly preferably between

$$360*0.99*\left(\frac{3-\sqrt{5}}{2}\right)^{\circ} \text{ and } 360*1.01*\left(\frac{3-\sqrt{5}}{2}\right)^{\circ},$$

in particular through an angle of approximately

$$360*\left(\frac{3-\sqrt{5}}{2}\right)^{\circ}.$$

Here, the magnitude of

$$360*[3-\sqrt{5}]/2$$

corresponds to the golden angle. What is achieved in the ideal case, i.e. if the golden angle is used, is that no iteration is congruent to a preceding iteration. In particular, this causes the measurement point distribution to be increased with each iteration. However, a further advantage of the golden angle is that the increase in the measurement point distribution is substantially uniform. Hence, the measurement method may be interrupted after any number of iterations, without an excessively asymmetric measurement point distribution being risked. As a result, it is also possible to remove sections or entire iterations which were identified as outliers. For the purposes of identifying outliers, the individual iterations are preferably used for modeling the region. In particular, this is possible if the degree of coverage is maintained in the process. By way of example, if a very small angle, such as e.g. 3.6°, were to be selected, an excessively asymmetrical measurement point distribution would be obtained after e.g. 10 iterations in the case of a two-loop trajectory.

However, other angles may also be provided in variants, e.g. 0.375*360° such that, for example, the identity is reached after 8 iterations or 0.4375*360° such that the identity is reached after 16 iterations, etc. (see above).

Preferably, at least a first model of the region is calculated on the basis of the measurement points of the first iteration and a second model of the region is calculated on the basis of the measurement points of the second iteration. Here, these are preferably geometric models. The calculation of the model may comprise the calculation both of the corneal surface and of further planes, such as the corneal rear surface, the lens, etc. The position of the eye may be ascertained particularly easily with the aid of these, preferably geometric models. Then, the position and, optionally, the alignment of the cornea may be determined from the models in each case. Preferably, modeling is carried out by means of Zernike polynomials.

In variants, calculating the model may be dispensed with.

In contrast to traditional photography, by means of which two-dimensional or three-dimensional snapshots may be obtained, the measurement by means of OCT is based on the sequential recording of one-dimensional A-scans. This increases the measurement duration, and so the recordings become susceptible to eye movements, eyelid movements and the like. Hence, there is a risk of the scans being erroneous or incomplete. Hence, the motivation to be able to eliminate movement artifacts is there in the case of OCT measurements.

Therefore, preferably, a spatial curve, which represents the movement of the eye, is calculated on the basis of the at least first model and the second model. The movement trajectory interpolated therefrom may then be applied to the measured points or to the models in order to obtain more accurate modeling. Here, it is particularly advantageous if the individual models, which are typically ascertained in each case on the basis of an iteration or of part of an iteration, have equal status for determining the movement.

In variants, it is also possible to dispense with a calculation of the spatial curve for representing the eye movement.

Preferably, symmetry vectors are determined for the first model and the second model, the spatial curve representing the movement of the eye being calculated on the basis of said symmetry vectors. The symmetry vector is understood to mean a vector, about the axis of which the eye is substantially symmetrical. Typically, this symmetry vector approximately lies in the region of an optical axis of the eye. The symmetry vector may be determined over one or more planes of the eye, such as e.g. corneal front side, corneal rear side, lens surfaces, etc.

In variants, it is possible to dispense with determining symmetry vectors. For the purposes of aligning the eye, it is also possible to identify an asymmetry of the eye which may serve as a reference for the position and alignment of the eye.

Preferably, the movement comprises translational and rotating movement components. Using this, the symmetry vector may capture, firstly, the alignment of the axis of symmetry of the eye and a rotation of the eye. Using this, the symmetry vector may capture, firstly, the alignment of the axis of symmetry of the eye and a rotation of the eye. Overall, this further improves the method for measuring a region of an eye since a movement reconstruction of the eye may be calculated particularly precisely on the basis of these data.

In variants, it is possible to dispense with e.g. the rotating movement portion.

Preferably, a mean model is calculated from the models. Using this method, it is possible to model the region of the eye particularly precisely, in particular since the respective models are based, preferably in a pairwise manner, on at least partly non-common measurement points. A plurality of iterations are measured within the scope of the method. A model, e.g. a model of the cornea, is calculated on the basis of each individual iteration. Further, a position which e.g. may be ascertained by means of a symmetry vector (see above) is determined for each model. A movement trajectory of the eye may be ascertained on the basis of the positions. Subsequently, the positions of the individual models are aligned on the basis of the movement trajectory. Finally, a mean model is calculated on the basis of the aligned models.

In variants, it is also possible to align the individual measurement points of the iterations, which are subsequently combined by calculation to form a model.

In a further preferred method, for the purposes of reducing movement artifacts, measurement points themselves instead of the models are corrected to corrected measurement points on account of the first model and of the second model.

Preferably, for the purposes of correcting the measurement points, the movement trajectory is interpolated on the basis of the positions and orientations of the models in such a way that each measurement point independently results in an interpolated position and alignment of the eye.

In variants, the interpolation may also be dispensed with.

Preferably, the corrected measurement points of the first iteration and of the second iteration are combined to form a cumulative model. The cumulative model thus comprises the measurement points, adjusted by the movement artifacts, of a plurality of iterations, as a result of which a particularly high measurement point density and hence a particularly high precision is obtained when measuring the region of the eye.

In variants, the calculation of the cumulative model on the basis of the individual movement-corrected measurement points may also be dispensed with. In this case, it is possible, for example as explained above, for the individual corrected models to be combined by calculation to form a mean model.

Preferably, the trajectory is passed over in m iterations, where m is selected in such a way that a mean measurement point distance is less than a predetermined expected lateral movement of the eye. In a particularly preferred embodiment, m is selected in such a way that the mean measurement point distance approximately corresponds to the predetermined expected lateral movement of the eye. From this number of iterations, the placement of the new measurement points between the already measured measurement points is random on account of the eye movement, as a result of which it may even be possible, under certain circumstances, to dispense with the displacement and/or rotation of the trajectory.

In variants, m may also be selected to be smaller. In this case, the measurement method could be carried out more quickly but with a lower measurement point density.

When measuring the cornea using OCT, the central region of the cornea is typically scanned at discrete positions. Topography maps of the region may be created on the basis of the measurement points. For the purposes of reconstructing the surface, use is often made of Zernike polynomials. While a 4th order Zernike polynomial is sufficient in the case of a normal cornea, the 7th or higher order may be required for an abnormal eye. Since the Zernike polynomials moreover lose their orthogonality in the discrete case, the employed scanning pattern has a direct influence on the numerical stability of the reconstruction and limits the order of the Zernike reconstruction.

Preferably, the trajectory has the form of a spiral, in particular a Fermat's spiral; a hypotrochoid; a grid, in particular parallel lines; or of radially arranged loops with a common point of intersection. These forms of the trajectory were found to be particularly advantageous in conjunction with the method according to the invention. The grid-shaped trajectories are particularly simple to scan since only straight lines need to be passed over. However, these are disadvantageous in that relatively small radii must be passed over, as a result of which the speed is typically reduced in these regions. This slows down the scanning process, as a result of which movement artifacts may increasingly occur once again. It was therefore found to be advantageous to use meridional trajectories, which are arranged about a common point, in particular the apex of the eye. Further, an advantage of this method lies in the simplified movement correction since all meridional lines pass through the apex of the eye. On the other hand, disadvantages consist of the fact that, as a rule, no ideal measurement point distribution is achievable, as a result of which the Zernike reconstruction is in turn impaired, and that small radii typically have to be passed over.

Therefore, the form of the trajectory is particularly preferably a Fermat's spiral or a hypotrochoid. These forms have particularly expedient measurement point distributions, wherein the measurement point density may be increased particularly ideally in the case of a suitable rotation of the trajectory and a more stable Zernike reconstruction may be obtained.

Particularly preferably, the trajectory is a Fermat's spiral with the form:

$$r=\pm\theta^{1/2}$$

where r is the radius and θ is the angle of the spiral points in polar coordinates. In a particularly preferred method, the trajectory is fitted in such a way that the radius goes linearly from zero to the radius of the scanning pattern and back again, as a result of which an iteration is defined. This obtains a spiral which goes to the outside, to the inside, etc.

However, other trajectories, in particular other spirals, etc., may be provided in variants.

In a further advantageous embodiment, the trajectory is rotated continuously through an angle in each iteration. If the golden angle is selected to this end, the region is covered by a continuously increased measurement point density, i.e. the mean distance between the measurement points is reduced with each iteration (see above).

However, a person skilled in the art knows of any other desired trajectories which may be used in the present method.

Further, it is also clear to a person skilled in the art that the trajectory is generally not restricted to exactly observing

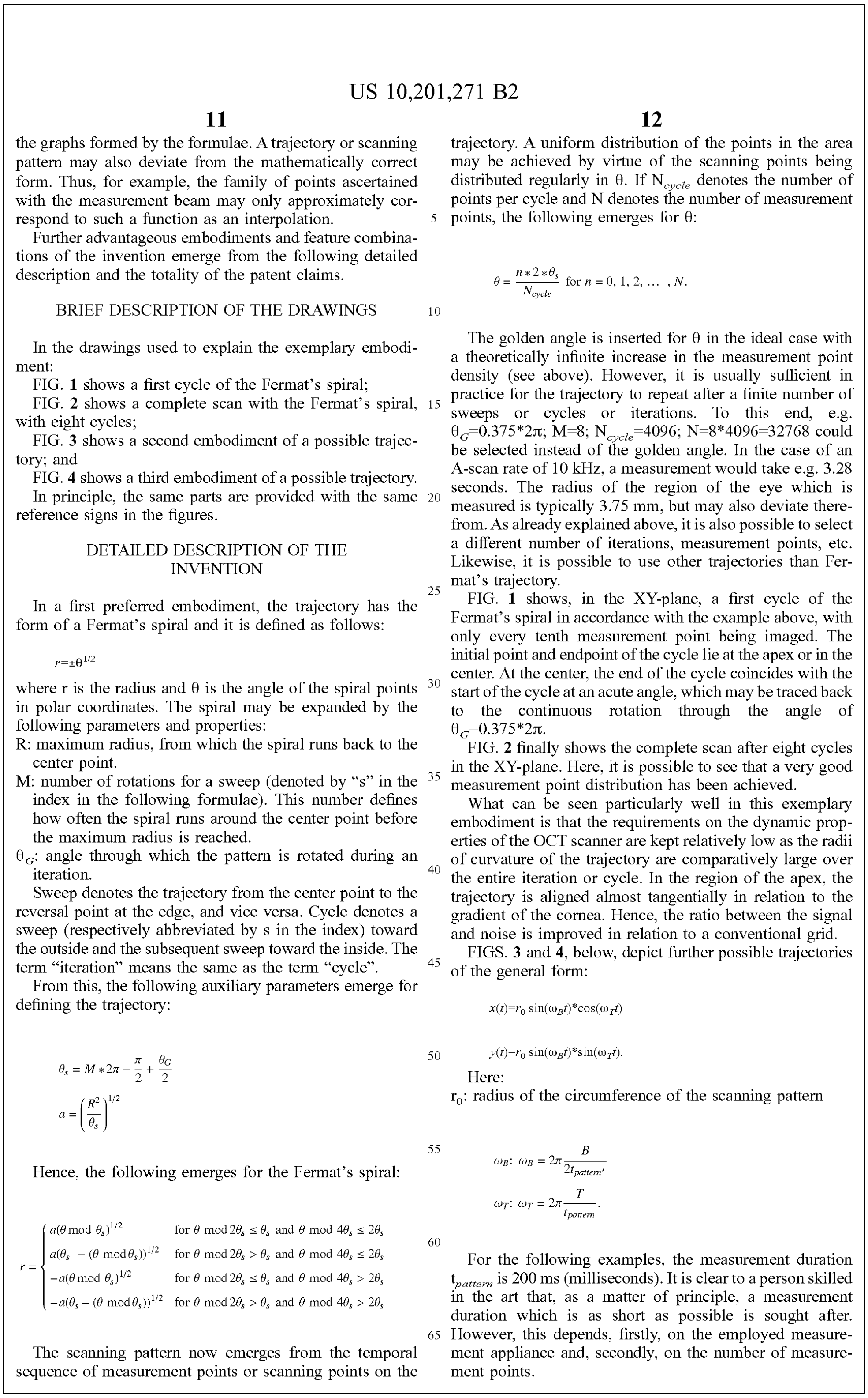

the graphs formed by the formulae. A trajectory or scanning pattern may also deviate from the mathematically correct form. Thus, for example, the family of points ascertained with the measurement beam may only approximately correspond to such a function as an interpolation.

Further advantageous embodiments and feature combinations of the invention emerge from the following detailed description and the totality of the patent claims.

BRIEF DESCRIPTION OF THE DRAWINGS

In the drawings used to explain the exemplary embodiment:

FIG. **1** shows a first cycle of the Fermat's spiral;

FIG. **2** shows a complete scan with the Fermat's spiral, with eight cycles;

FIG. **3** shows a second embodiment of a possible trajectory; and

FIG. **4** shows a third embodiment of a possible trajectory.

In principle, the same parts are provided with the same reference signs in the figures.

DETAILED DESCRIPTION OF THE INVENTION

In a first preferred embodiment, the trajectory has the form of a Fermat's spiral and it is defined as follows:

$$r=\pm\theta^{1/2}$$

where r is the radius and θ is the angle of the spiral points in polar coordinates. The spiral may be expanded by the following parameters and properties:

R: maximum radius, from which the spiral runs back to the center point.

M: number of rotations for a sweep (denoted by "s" in the index in the following formulae). This number defines how often the spiral runs around the center point before the maximum radius is reached.

θ_G: angle through which the pattern is rotated during an iteration.

Sweep denotes the trajectory from the center point to the reversal point at the edge, and vice versa. Cycle denotes a sweep (respectively abbreviated by s in the index) toward the outside and the subsequent sweep toward the inside. The term "iteration" means the same as the term "cycle".

From this, the following auxiliary parameters emerge for defining the trajectory:

$$\theta_s = M * 2\pi - \frac{\pi}{2} + \frac{\theta_G}{2}$$

$$a = \left(\frac{R^2}{\theta_s}\right)^{1/2}$$

Hence, the following emerges for the Fermat's spiral:

$$r = \begin{cases} a(\theta \bmod \theta_s)^{1/2} & \text{for } \theta \bmod 2\theta_s \le \theta_s \text{ and } \theta \bmod 4\theta_s \le 2\theta_s \\ a(\theta_s - (\theta \bmod \theta_s))^{1/2} & \text{for } \theta \bmod 2\theta_s > \theta_s \text{ and } \theta \bmod 4\theta_s \le 2\theta_s \\ -a(\theta \bmod \theta_s)^{1/2} & \text{for } \theta \bmod 2\theta_s \le \theta_s \text{ and } \theta \bmod 4\theta_s > 2\theta_s \\ -a(\theta_s - (\theta \bmod \theta_s))^{1/2} & \text{for } \theta \bmod 2\theta_s > \theta_s \text{ and } \theta \bmod 4\theta_s > 2\theta_s \end{cases}$$

The scanning pattern now emerges from the temporal sequence of measurement points or scanning points on the trajectory. A uniform distribution of the points in the area may be achieved by virtue of the scanning points being distributed regularly in θ. If N_{cycle} denotes the number of points per cycle and N denotes the number of measurement points, the following emerges for θ:

$$\theta = \frac{n * 2 * \theta_s}{N_{cycle}} \text{ for } n = 0, 1, 2, \ldots , N.$$

The golden angle is inserted for θ in the ideal case with a theoretically infinite increase in the measurement point density (see above). However, it is usually sufficient in practice for the trajectory to repeat after a finite number of sweeps or cycles or iterations. To this end, e.g. θ_G=0.375*2π; M=8; N_{cycle}=4096; N=8*4096=32768 could be selected instead of the golden angle. In the case of an A-scan rate of 10 kHz, a measurement would take e.g. 3.28 seconds. The radius of the region of the eye which is measured is typically 3.75 mm, but may also deviate therefrom. As already explained above, it is also possible to select a different number of iterations, measurement points, etc. Likewise, it is possible to use other trajectories than Fermat's trajectory.

FIG. **1** shows, in the XY-plane, a first cycle of the Fermat's spiral in accordance with the example above, with only every tenth measurement point being imaged. The initial point and endpoint of the cycle lie at the apex or in the center. At the center, the end of the cycle coincides with the start of the cycle at an acute angle, which may be traced back to the continuous rotation through the angle of θ_G=0.375*2π.

FIG. **2** finally shows the complete scan after eight cycles in the XY-plane. Here, it is possible to see that a very good measurement point distribution has been achieved.

What can be seen particularly well in this exemplary embodiment is that the requirements on the dynamic properties of the OCT scanner are kept relatively low as the radii of curvature of the trajectory are comparatively large over the entire iteration or cycle. In the region of the apex, the trajectory is aligned almost tangentially in relation to the gradient of the cornea. Hence, the ratio between the signal and noise is improved in relation to a conventional grid.

FIGS. **3** and **4**, below, depict further possible trajectories of the general form:

$$x(t)=r_0 \sin(\omega_B t)*\cos(\omega_T t)$$

$$y(t)=r_0 \sin(\omega_B t)*\sin(\omega_T t).$$

Here:

r_0: radius of the circumference of the scanning pattern

$$\omega_B\colon\ \omega_B = 2\pi\frac{B}{2t_{pattern'}}$$

$$\omega_T\colon\ \omega_T = 2\pi\frac{T}{t_{pattern}}.$$

For the following examples, the measurement duration $t_{pattern}$ is 200 ms (milliseconds). It is clear to a person skilled in the art that, as a matter of principle, a measurement duration which is as short as possible is sought after. However, this depends, firstly, on the employed measurement appliance and, secondly, on the number of measurement points.

In the present case, the number of measurement points equals 3200; the measurement frequency (i.e. the rate at which measurement points are captured) is f=16 kHz. Here, an equilibrium in which the measurement duration is sufficiently small and, at the same time, the number of measurement points and hence, in the case of a constant area to be measured, the resolution are sufficiently high, is sought after.

Furthermore, the measurement frequency is, however, only so large that a sufficient signal strength still emerges for each measurement point as said signal strength decreases with increasing measurement frequency.

FIG. **3** shows an embodiment of a possible trajectory in a particularly preferred form, with B=8 and T=7. From the graph of the function, it can readily be identified that the radius of curvature in each case increases from the edge region toward the center. Moreover, eight points of intersection always lie on a circle concentric with the center of the circumference in each case and the center point is passed through multiple times. Furthermore, it can be seen from the figure that both the edge region and the region near the center may be measured with a high resolution. The scanning pattern has 48 single points of intersection and one eight-fold point of intersection in the center. It is possible to detect and eliminate the eye movement, in particular using the points of intersection away from the center. The high number of points of intersection allows a detection of the eye movement with a correspondingly high frequency (measurement time/number of points of intersection=mean updating time). In the present case, the rotation after each cycle is θ_G=0.4375*2π, and so the trajectory is once again present in the original orientation after 16 cycles.

FIG. **4** finally shows, as a further example, a hypotrochoid trajectory as a possible embodiment. The hypotrochoid trajectory has the following general form:

$$x(t) = (a-b)\cos(s) + c * \cos\left(\left(\frac{a-b}{b}\right) * s\right);$$

$$y(t) = (a-b)\sin(s) + c * \sin\left(\left(\frac{a-b}{b}\right) * s\right).$$

For the purposes of ascertaining measurement values in ophthalmology, the values may be selected in such a way that, once again, a radius of approximately 4 mm is achieved. As an example, a=2, b=0.1 and c=2.1 have been selected in FIG. **4**. Using this parameterization, a free circle may be identified in the center of the circumference, said free circle having a radius of approximately 0.2 mm. Therefore, this free area satisfies the 0.5 mm criterion specified at the outset.

In the present case, the rotation after each cycle is θ_G=0.56*2π, and so the trajectory is once again present in the original orientation after 25 cycles.

In a further exemplary embodiment, use is made of a grid of parallel lines as a trajectory, with the grid being displaced by e.g. 10% of the line spacing in the XY-plane at right angles to a line direction after each iteration. In a further embodiment, there is in each case a displacement by half of the last line spacing, as a result of which it is possible to obtain a continuous refinement of the measurement point distribution. In a further embodiment, the grid is rotated through an angle at each iteration, as explained at the outset. Finally, the grid is both rotated and displaced after each iteration in a further embodiment.

While the trajectory is continuously rotated and/or displaced in each case during the iteration in the exemplary

embodiments above, the trajectory may also be rotated and/or displaced between the iterations in each case. However, a consequence of this is that, as a rule, the measurement beam must pass through a relatively large directional change between the iterations, as a result of which, once again, the measurement method is slowed down.

In each of the exemplary embodiments listed above, a model of the region of the eye is advantageously created for the purposes of correcting the movement artifacts after each iteration or after each sweep. A symmetry vector is determined on the basis of the model, by means of which it is also possible to determine the orientation of the eye in respect of a rotation about the symmetry vector and in the XY-plane. A movement trajectory of the eye is preferably obtained subsequently using the plurality of symmetry vectors. Finally, each model of the region of the eye ascertained in advance may be aligned by means of the movement trajectory of the eye. The aligned regions of the eye may once again be combined by calculation in an advantageous manner to form a mean model of the region of the eye. A person skilled in the art knows of any variants for the present correction of the movement artifacts. Thus, the movement trajectory may be used to correct the individual points, etc.

The measurement duration and the number of measurement points may also be smaller or larger, depending on the employed measurement appliance. Depending on the measurement arrangement, it may be advantageous if the measurement duration is shortened, with the smaller resolution being accepted. On the other hand, it is also possible to increase the number of measurement points to the detriment of the measurement duration.

In the present case, the radius of the area to be measured is between 3 and 4 mm. However, this likewise depends on the specific requirements and may, in principle, be selected as required, e.g. 10 mm, 3.5 mm, 1.5 mm and all regions lying therebetween and outside thereof.

In the present case, the axial system resolution of the measurement appliance lies at approximately 4.6 μm, but it may also be higher or lower.

It is clear to a person skilled in the art that the diameter, the number of measurement points and the measurement time may lie in different ranges.

Depending on the measurement system, the measurement frequency may range from a few kHz to several MHz. Measurement frequencies in the range from 10 to 200 kHz were found to be worth pursuing.

Finally, it is also clear to a person skilled in the art that the trajectory is not restricted to exactly observing the graphs formed by the specified mathematical formulae. A trajectory or scanning pattern may also deviate from the mathematically exact form. By way of example, the family of points ascertained with the measurement beam may merely approximately correspond to such a function as an interpolation.

In conclusion, it should be noted that, according to the invention, a method is developed for interferometrically capturing measurement points of a region of an eye, said method permitting a particularly precise capture of the topographies of the region. Further, this achieves a movement correction of the eye in an advantageous manner.

The invention claimed is:

1. A method for interferometrically capturing measurement points of a region of an eye, wherein a plurality of measurement points are captured by a measurement beam along a trajectory, wherein the same trajectory is passed over by the measurement beam in the region during at least a first iteration and a second iteration, wherein the trajectory of the

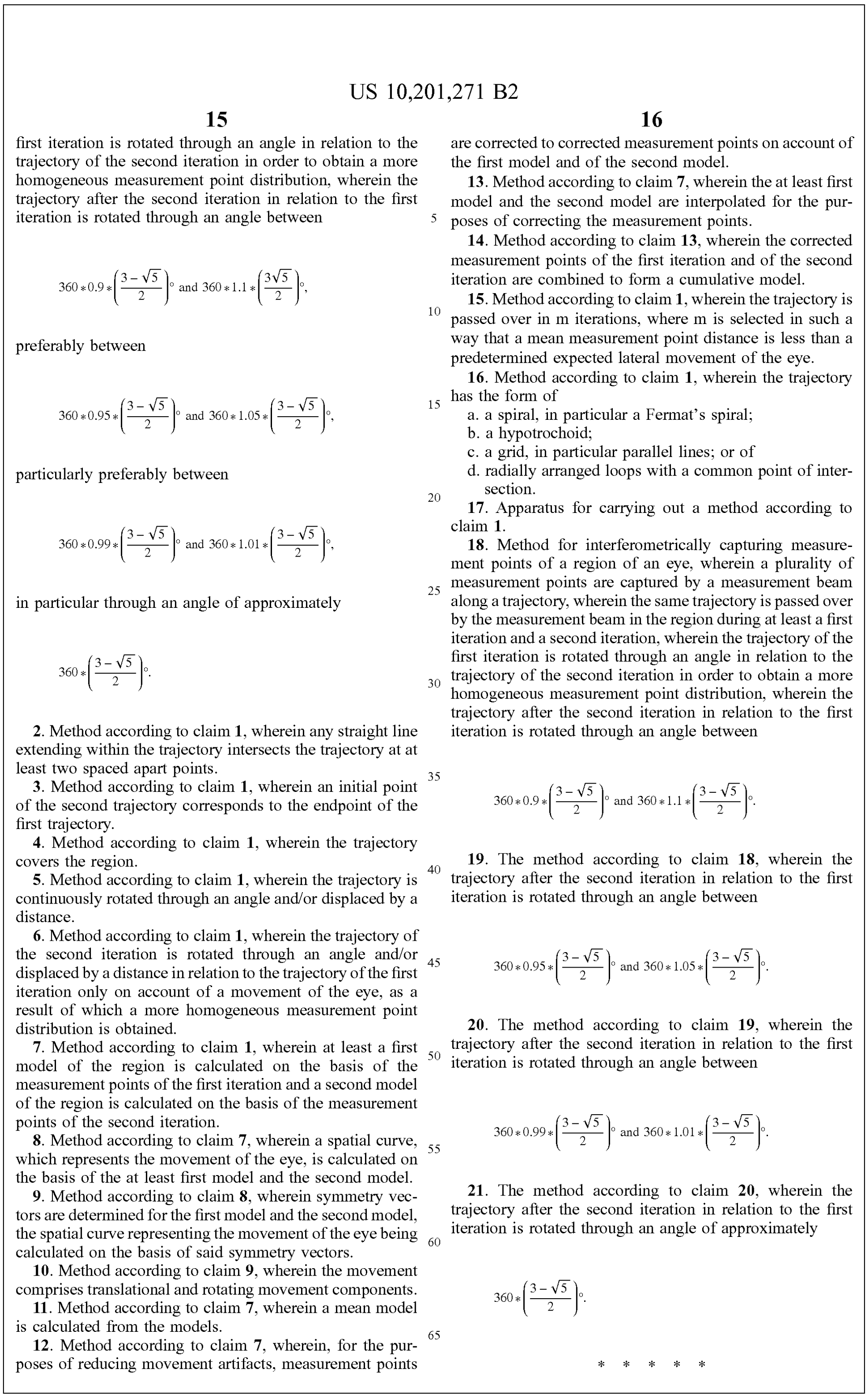

US 10,201,271 B2

15

first iteration is rotated through an angle in relation to the trajectory of the second iteration in order to obtain a more homogeneous measurement point distribution, wherein the trajectory after the second iteration in relation to the first iteration is rotated through an angle between

$$360*0.9*\left(\frac{3-\sqrt{5}}{2}\right)^{\circ} \text{ and } 360*1.1*\left(\frac{3\sqrt{5}}{2}\right)^{\circ},$$

preferably between

$$360*0.95*\left(\frac{3-\sqrt{5}}{2}\right)^{\circ} \text{ and } 360*1.05*\left(\frac{3-\sqrt{5}}{2}\right)^{\circ},$$

particularly preferably between

$$360*0.99*\left(\frac{3-\sqrt{5}}{2}\right)^{\circ} \text{ and } 360*1.01*\left(\frac{3-\sqrt{5}}{2}\right)^{\circ},$$

in particular through an angle of approximately

$$360*\left(\frac{3-\sqrt{5}}{2}\right)^{\circ}.$$

2. Method according to claim **1**, wherein any straight line extending within the trajectory intersects the trajectory at at least two spaced apart points.

3. Method according to claim **1**, wherein an initial point of the second trajectory corresponds to the endpoint of the first trajectory.

4. Method according to claim **1**, wherein the trajectory covers the region.

5. Method according to claim **1**, wherein the trajectory is continuously rotated through an angle and/or displaced by a distance.

6. Method according to claim **1**, wherein the trajectory of the second iteration is rotated through an angle and/or displaced by a distance in relation to the trajectory of the first iteration only on account of a movement of the eye, as a result of which a more homogeneous measurement point distribution is obtained.

7. Method according to claim **1**, wherein at least a first model of the region is calculated on the basis of the measurement points of the first iteration and a second model of the region is calculated on the basis of the measurement points of the second iteration.

8. Method according to claim **7**, wherein a spatial curve, which represents the movement of the eye, is calculated on the basis of the at least first model and the second model.

9. Method according to claim **8**, wherein symmetry vectors are determined for the first model and the second model, the spatial curve representing the movement of the eye being calculated on the basis of said symmetry vectors.

10. Method according to claim **9**, wherein the movement comprises translational and rotating movement components.

11. Method according to claim **7**, wherein a mean model is calculated from the models.

12. Method according to claim **7**, wherein, for the purposes of reducing movement artifacts, measurement points

16

are corrected to corrected measurement points on account of the first model and of the second model.

13. Method according to claim **7**, wherein the at least first model and the second model are interpolated for the purposes of correcting the measurement points.

14. Method according to claim **13**, wherein the corrected measurement points of the first iteration and of the second iteration are combined to form a cumulative model.

15. Method according to claim **1**, wherein the trajectory is passed over in m iterations, where m is selected in such a way that a mean measurement point distance is less than a predetermined expected lateral movement of the eye.

16. Method according to claim **1**, wherein the trajectory has the form of

a. a spiral, in particular a Fermat's spiral;

b. a hypotrochoid;

c. a grid, in particular parallel lines; or of

d. radially arranged loops with a common point of intersection.

17. Apparatus for carrying out a method according to claim **1**.

18. Method for interferometrically capturing measurement points of a region of an eye, wherein a plurality of measurement points are captured by a measurement beam along a trajectory, wherein the same trajectory is passed over by the measurement beam in the region during at least a first iteration and a second iteration, wherein the trajectory of the first iteration is rotated through an angle in relation to the trajectory of the second iteration in order to obtain a more homogeneous measurement point distribution, wherein the trajectory after the second iteration in relation to the first iteration is rotated through an angle between

$$360*0.9*\left(\frac{3-\sqrt{5}}{2}\right)^{\circ} \text{ and } 360*1.1*\left(\frac{3-\sqrt{5}}{2}\right)^{\circ}.$$

19. The method according to claim **18**, wherein the trajectory after the second iteration in relation to the first iteration is rotated through an angle between

$$360*0.95*\left(\frac{3-\sqrt{5}}{2}\right)^{\circ} \text{ and } 360*1.05*\left(\frac{3-\sqrt{5}}{2}\right)^{\circ}.$$

20. The method according to claim **19**, wherein the trajectory after the second iteration in relation to the first iteration is rotated through an angle between

$$360*0.99*\left(\frac{3-\sqrt{5}}{2}\right)^{\circ} \text{ and } 360*1.01*\left(\frac{3-\sqrt{5}}{2}\right)^{\circ}.$$

21. The method according to claim **20**, wherein the trajectory after the second iteration in relation to the first iteration is rotated through an angle of approximately

$$360*\left(\frac{3-\sqrt{5}}{2}\right)^{\circ}.$$

* * * * *

Patent Application EP 3 662 812 A1

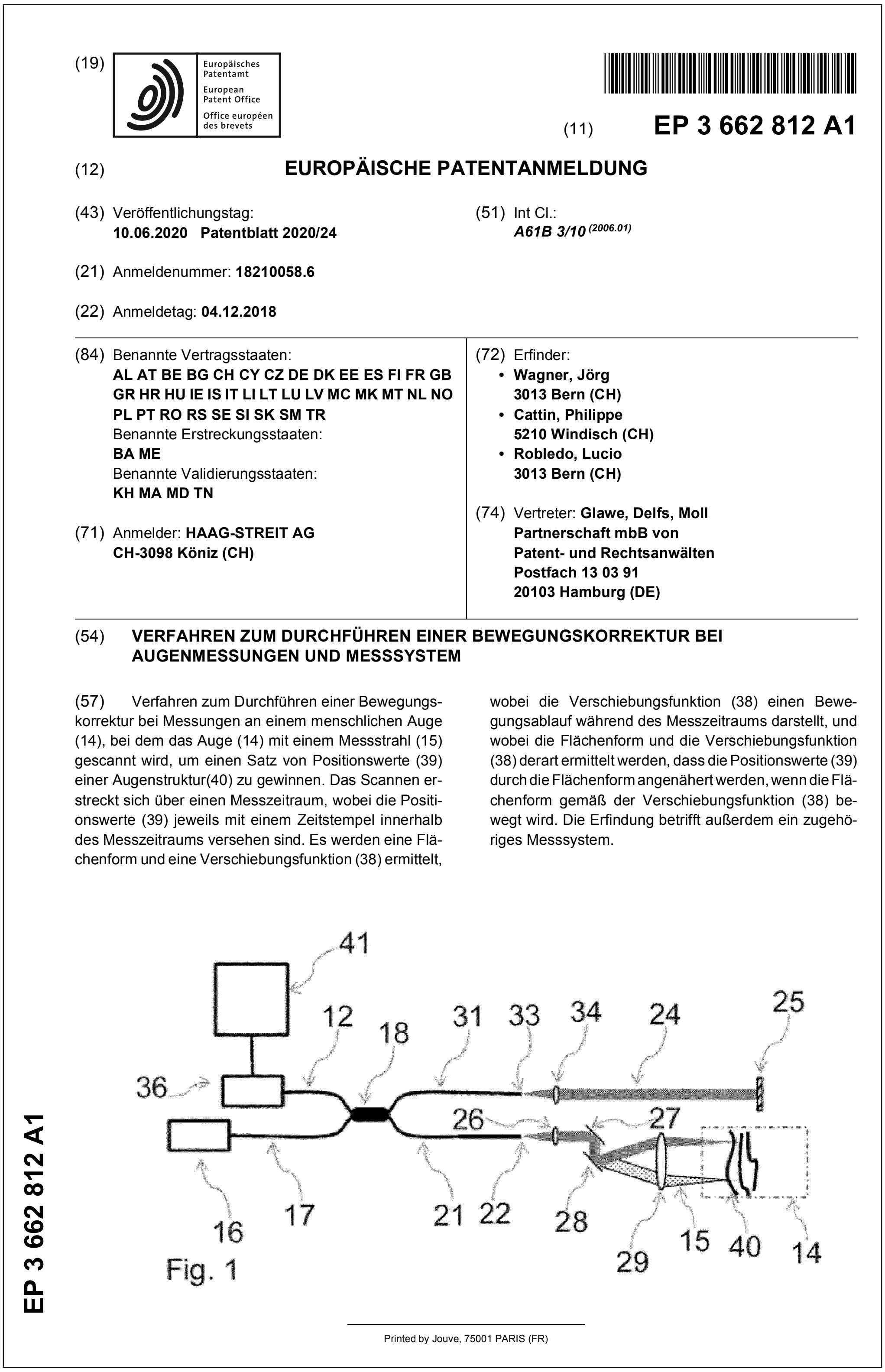

(19) Europäisches Patentamt
European Patent Office
Office européen des brevets

(11) EP 3 662 812 A1

(12) **EUROPÄISCHE PATENTANMELDUNG**

(43) Veröffentlichungstag:
10.06.2020 Patentblatt 2020/24

(51) Int Cl.:
A61B 3/10 $^{(2006.01)}$

(21) Anmeldenummer: **18210058.6**

(22) Anmeldetag: **04.12.2018**

(84) Benannte Vertragsstaaten:
AL AT BE BG CH CY CZ DE DK EE ES FI FR GB GR HR HU IE IS IT LI LT LU LV MC MK MT NL NO PL PT RO RS SE SI SK SM TR
Benannte Erstreckungsstaaten:
BA ME
Benannte Validierungsstaaten:
KH MA MD TN

(71) Anmelder: **HAAG-STREIT AG**
CH-3098 Köniz (CH)

(72) Erfinder:
- **Wagner, Jörg**
  3013 Bern (CH)
- **Cattin, Philippe**
  5210 Windisch (CH)
- **Robledo, Lucio**
  3013 Bern (CH)

(74) Vertreter: **Glawe, Delfs, Moll**
Partnerschaft mbB von
Patent- und Rechtsanwälten
Postfach 13 03 91
20103 Hamburg (DE)

(54) VERFAHREN ZUM DURCHFÜHREN EINER BEWEGUNGSKORREKTUR BEI AUGENMESSUNGEN UND MESSSYSTEM

(57) Verfahren zum Durchführen einer Bewegungskorrektur bei Messungen an einem menschlichen Auge (14), bei dem das Auge (14) mit einem Messstrahl (15) gescannt wird, um einen Satz von Positionswerte (39) einer Augenstruktur(40) zu gewinnen. Das Scannen erstreckt sich über einen Messzeitraum, wobei die Positionswerte (39) jeweils mit einem Zeitstempel innerhalb des Messzeitraums versehen sind. Es werden eine Flächenform und eine Verschiebungsfunktion (38) ermittelt, wobei die Verschiebungsfunktion (38) einen Bewegungsablauf während des Messzeitraums darstellt, und wobei die Flächenform und die Verschiebungsfunktion (38) derart ermittelt werden, dass die Positionswerte (39) durch die Flächenform angenähert werden, wenn die Flächenform gemäß der Verschiebungsfunktion (38) bewegt wird. Die Erfindung betrifft außerdem ein zugehöriges Messsystem.

Fig. 1

EP 3 662 812 A1

Printed by Jouve, 75001 PARIS (FR)

Beschreibung

[0001] Die Erfindung betrifft ein Verfahren zum Durchführen einer Bewegungskorrektur bei Augenmessungen. Die Erfindung betrifft außerdem ein zugehöriges Messsystem.

[0002] Bei Messungen am Auge kann das Messergebnis verfälscht werden, wenn sich das Auge während der Aufnahme der Messwerte bewegt. Je mehr Zeit die Messung in Anspruch nimmt, desto stärker wirken die Bewegungen des Auges sich aus. Eine längere Messdauer ergibt sich insbesondere beim Abtasten des Auges mit einem Messstrahl, wie es beispielsweise bei OCT-Messungen üblicherweise der Fall ist.

[0003] Eine mögliche Vorgehensweise ist es, zunächst eine schnelle Referenzmessung über den Messbereich aufzunehmen, bei der die Messdauer so kurz ist, dass die Messung nicht durch Bewegungen des Auges verfälscht wird. Die nachfolgenden längeren Messungen mit einer größeren Anzahl von Stützpunkten, können anhand der ersten Messung ausgerichtet werden, um die Bewegung aus den Daten zu eliminieren, US 7,365,856 B2, EP 2 797 493 A1. Nachteil bei dieser Vorgehensweise ist, dass durch eine Ungenauigkeit bei der Referenzmessung das gesamte Messergebnis verfälscht werden kann. Außerdem ist ein schnelles Scansystem vonnöten um die Referenzmessung genügend schnell ausführen zu können.

[0004] Alternativ können auch mehrere schnelle Messungen aufgenommen werden welche danach aufeinander ausgerichtet werden. Voraussetzung dafür ist, dass innerhalb einer Messung eine sinnvolle Geometrie der Auges (z.B. ein Meridian) genügend schnell aufgenommen wird so dass die Augenbewegung darin vernachlässigt werden kann. Auch dafür ist ein schnelles System mit schneller Datenerfassung und schnellem Scanner erforderlich.

[0005] Der Erfindung liegt die Aufgabe zugrunde, ein Verfahren und ein Messsystem zum Durchführen einer Bewegungskorrektur bei Augenmessungen vorzustellen, die eine verminderte Fehleranfälligkeit haben. Ausgehend vom genannten Stand der Technik wird die Aufgabe gelöst mit den Merkmalen der unabhängigen Ansprüche. Vorteilhafte Ausführungsformen sind in den Unteransprüchen angegeben.

[0006] Bei dem erfindungsgemäßen Verfahren wird das Auge mit einem Messstrahl gescannt, um einen Satz von Positionswerten einer Augenstruktur zu gewinnen. Das Scannen erstreckt sich über einen Messzeitraum, wobei die Positionswerte jeweils mit einem Zeitstempel innerhalb des Messzeitraums versehen sind. Es werden eine Flächenform und eine Verschiebungsfunktion ermittelt, wobei die Verschiebungsfunktion einen Bewegungsablauf während des Messzeitraums darstellt. Die Flächenform und die Verschiebungsfunktion werden derart ermittelt, dass die Positionswerte durch die Flächenform angenähert werden, wenn die Flächenform gemäß der Verschiebungsfunktion bewegt wird.

[0007] Die Erfindung geht von der Annahme aus, dass die Bewegung, die das Auge innerhalb des Messzeitraums durchgeführt hat, durch eine Verschiebungsfunktion beschrieben werden kann. In einem Idealfall ist die Messung frei von Messfehlern, es wird eine Flächenform gefunden, die der tatsächlichen Form der Augenstruktur entspricht, und es wird eine Verschiebungsfunktion gefunden, die dem tatsächlichen Bewegungsablauf des Auges entspricht. Verschiebt man diese Flächenform entsprechend dieser Verschiebungsfunktion, so liegen (bei geeigneter gegenseitiger Anpassung des räumlichen und zeitlichen Koordinatensystems) alle von der Augenstruktur aufgenommenen Positionswerte auf der Flächenform. Im Unterschied zum Stand der Technik ist eine Referenzmessung als Ausgangspunkt für die Bewegungskorrektur nicht erforderlich. Dies ist von besonderem Vorteil, wenn das Scansystem nicht über die nötige Geschwindigkeit verfügt um eine bewegungsarme Referenzmessung durchzuführen.

[0008] In der Praxis treten Messfehler auf, und es kommt zu Abweichungen sowohl zwischen der Flächenform und der tatsächlichen Form der Augenstruktur als auch zwischen der Verschiebungsfunktion und dem tatsächlichen Bewegungsablauf. Mit der Formulierung, dass die Positionswerte durch die Flächenform "angenähert" werden, wird diese Abweichung zwischen idealem und praktisch durchgeführtem Verfahren berücksichtigt. Bei Durchführung des Verfahrens in idealer Form würden die Positionswerte und die Flächenform identisch übereinstimmen. Annähern im Sinne der Erfindung bedeutet, die Flächenform und die Verschiebungsfunktion so zu ermitteln, dass die Positionswerte im Rahmen der Randbedingungen der praktisch durchgeführten Messung angenähert werden. Beispielsweise kann ein Gütekriterium für die Annäherung vorgegeben werden, und es kann die Flächenform und die Verschiebungsfunktion so ermittelt werden, dass die anhand des Gütekriteriums festgestellte Abweichung kleiner ist als ein vorgegebener Schwellwert. Wenn in der nachfolgenden Beschreibung von Positionswerten gesprochen wird, die auf der Flächenform liegen, so ist dies gleichbedeutend mit einer Annäherung in diesem Sinne.

[0009] Betrachtet man einen ersten Zeitpunkt und einen zweiten Zeitpunkt innerhalb des Messzeitraums, so ergibt sich aus der Verschiebungsfunktion ein Bewegungsablauf, der die Bewegung des Auges zwischen den beiden Zeitpunkten beschreibt. Eine Flächenform, die die tatsächliche Form der Augenstruktur richtig wiedergibt, und die gemäß der Verschiebungsfunktion verschoben wird, kann gemeinsam mit den bei der Messung gewonnenen Positionswerten so in einem Koordinatensystem dargestellt werden, dass für beide Zeitpunkte die Flächenform auf dem mit der Messung gewonnenen Positionswert liegt. Gemeinsame Darstellung der Flächenform und der Positionswerte in einem Koordinatensystem bedeutet, dass die räumlichen Koordinaten der Flächenform und der Positionswerte richtig zueinander ausgerichtet ist und dass der zeitliche Ablauf der Verschiebungsfunktion mit den Zeitstempeln der Positionswerte abgeglichen ist. Die Formulierung, dass die Flächenform und die Positionswerte entsprechend der Verschiebungsfunktion

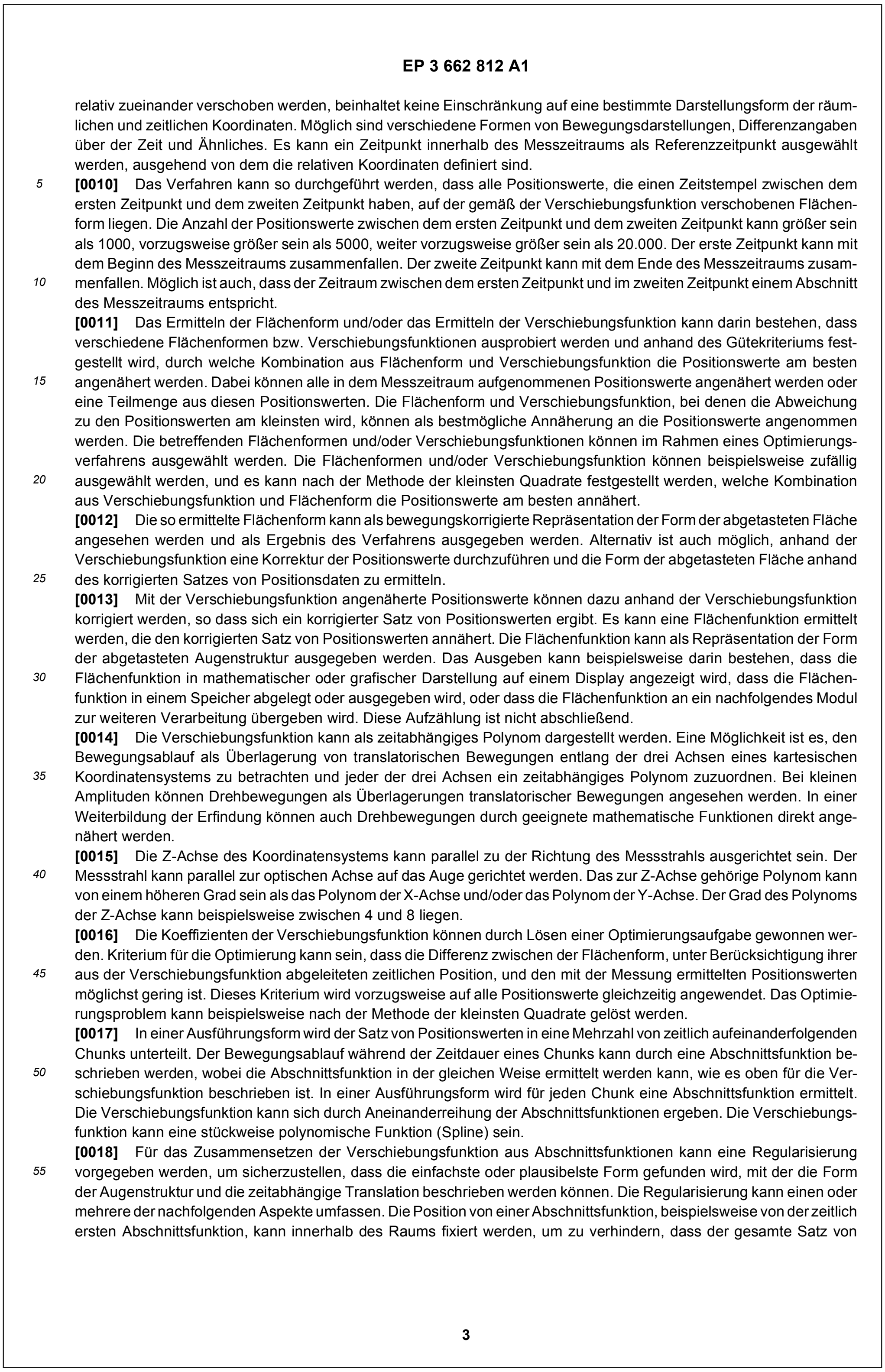

relativ zueinander verschoben werden, beinhaltet keine Einschränkung auf eine bestimmte Darstellungsform der räumlichen und zeitlichen Koordinaten. Möglich sind verschiedene Formen von Bewegungsdarstellungen, Differenzangaben über der Zeit und Ähnliches. Es kann ein Zeitpunkt innerhalb des Messzeitraums als Referenzzeitpunkt ausgewählt werden, ausgehend von dem die relativen Koordinaten definiert sind.

[0010] Das Verfahren kann so durchgeführt werden, dass alle Positionswerte, die einen Zeitstempel zwischen dem ersten Zeitpunkt und dem zweiten Zeitpunkt haben, auf der gemäß der Verschiebungsfunktion verschobenen Flächenform liegen. Die Anzahl der Positionswerte zwischen dem ersten Zeitpunkt und dem zweiten Zeitpunkt kann größer sein als 1000, vorzugsweise größer sein als 5000, weiter vorzugsweise größer sein als 20.000. Der erste Zeitpunkt kann mit dem Beginn des Messzeitraums zusammenfallen. Der zweite Zeitpunkt kann mit dem Ende des Messzeitraums zusammenfallen. Möglich ist auch, dass der Zeitraum zwischen dem ersten Zeitpunkt und im zweiten Zeitpunkt einem Abschnitt des Messzeitraums entspricht.

[0011] Das Ermitteln der Flächenform und/oder das Ermitteln der Verschiebungsfunktion kann darin bestehen, dass verschiedene Flächenformen bzw. Verschiebungsfunktionen ausprobiert werden und anhand des Gütekriteriums festgestellt wird, durch welche Kombination aus Flächenform und Verschiebungsfunktion die Positionswerte am besten angenähert werden. Dabei können alle in dem Messzeitraum aufgenommenen Positionswerte angenähert werden oder eine Teilmenge aus diesen Positionswerten. Die Flächenform und Verschiebungsfunktion, bei denen die Abweichung zu den Positionswerten am kleinsten wird, können als bestmögliche Annäherung an die Positionswerte angenommen werden. Die betreffenden Flächenformen und/oder Verschiebungsfunktionen können im Rahmen eines Optimierungsverfahrens ausgewählt werden. Die Flächenformen und/oder Verschiebungsfunktion können beispielsweise zufällig ausgewählt werden, und es kann nach der Methode der kleinsten Quadrate festgestellt werden, welche Kombination aus Verschiebungsfunktion und Flächenform die Positionswerte am besten annähert.

[0012] Die so ermittelte Flächenform kann als bewegungskorrigierte Repräsentation der Form der abgetasteten Fläche angesehen werden und als Ergebnis des Verfahrens ausgegeben werden. Alternativ ist auch möglich, anhand der Verschiebungsfunktion eine Korrektur der Positionswerte durchzuführen und die Form der abgetasteten Fläche anhand des korrigierten Satzes von Positionsdaten zu ermitteln.

[0013] Mit der Verschiebungsfunktion angenäherte Positionswerte können dazu anhand der Verschiebungsfunktion korrigiert werden, so dass sich ein korrigierter Satz von Positionswerten ergibt. Es kann eine Flächenfunktion ermittelt werden, die den korrigierten Satz von Positionswerten annähert. Die Flächenfunktion kann als Repräsentation der Form der abgetasteten Augenstruktur ausgegeben werden. Das Ausgeben kann beispielsweise darin bestehen, dass die Flächenfunktion in mathematischer oder grafischer Darstellung auf einem Display angezeigt wird, dass die Flächenfunktion in einem Speicher abgelegt oder ausgegeben wird, oder dass die Flächenfunktion an ein nachfolgendes Modul zur weiteren Verarbeitung übergeben wird. Diese Aufzählung ist nicht abschließend.

[0014] Die Verschiebungsfunktion kann als zeitabhängiges Polynom dargestellt werden. Eine Möglichkeit ist es, den Bewegungsablauf als Überlagerung von translatorischen Bewegungen entlang der drei Achsen eines kartesischen Koordinatensystems zu betrachten und jeder der drei Achsen ein zeitabhängiges Polynom zuzuordnen. Bei kleinen Amplituden können Drehbewegungen als Überlagerungen translatorischer Bewegungen angesehen werden. In einer Weiterbildung der Erfindung können auch Drehbewegungen durch geeignete mathematische Funktionen direkt angenähert werden.

[0015] Die Z-Achse des Koordinatensystems kann parallel zu der Richtung des Messstrahls ausgerichtet sein. Der Messstrahl kann parallel zur optischen Achse auf das Auge gerichtet werden. Das zur Z-Achse gehörige Polynom kann von einem höheren Grad sein als das Polynom der X-Achse und/oder das Polynom der Y-Achse. Der Grad des Polynoms der Z-Achse kann beispielsweise zwischen 4 und 8 liegen.

[0016] Die Koeffizienten der Verschiebungsfunktion können durch Lösen einer Optimierungsaufgabe gewonnen werden. Kriterium für die Optimierung kann sein, dass die Differenz zwischen der Flächenform, unter Berücksichtigung ihrer aus der Verschiebungsfunktion abgeleiteten zeitlichen Position, und den mit der Messung ermittelten Positionswerten möglichst gering ist. Dieses Kriterium wird vorzugsweise auf alle Positionswerte gleichzeitig angewendet. Das Optimierungsproblem kann beispielsweise nach der Methode der kleinsten Quadrate gelöst werden.

[0017] In einer Ausführungsform wird der Satz von Positionswerten in eine Mehrzahl von zeitlich aufeinanderfolgenden Chunks unterteilt. Der Bewegungsablauf während der Zeitdauer eines Chunks kann durch eine Abschnittsfunktion beschrieben werden, wobei die Abschnittsfunktion in der gleichen Weise ermittelt werden kann, wie es oben für die Verschiebungsfunktion beschrieben ist. In einer Ausführungsform wird für jeden Chunk eine Abschnittsfunktion ermittelt. Die Verschiebungsfunktion kann sich durch Aneinanderreihung der Abschnittsfunktionen ergeben. Die Verschiebungsfunktion kann eine stückweise polynomische Funktion (Spline) sein.

[0018] Für das Zusammensetzen der Verschiebungsfunktion aus Abschnittsfunktionen kann eine Regularisierung vorgegeben werden, um sicherzustellen, dass die einfachste oder plausibelste Form gefunden wird, mit der die Form der Augenstruktur und die zeitabhängige Translation beschrieben werden können. Die Regularisierung kann einen oder mehrere der nachfolgenden Aspekte umfassen. Die Position von einer Abschnittsfunktion, beispielsweise von der zeitlich ersten Abschnittsfunktion, kann innerhalb des Raums fixiert werden, um zu verhindern, dass der gesamte Satz von

Positionswerten innerhalb des Raums verschoben werden kann, ohne dass sich der Näherungsfehler ändert. Die Verschiebungsfunktion kann so regularisert werden, dass sich über alle Abschnittsfunktionen hinweg eine mittlere Verschiebung von null ergibt. Die Verschiebungsfunktion kann so regularisiert sein, dass der Übergang zwischen zwei zeitlich benachbarten Abschnittsfunktionen stetig ist. Die Verschiebungsfunktion kann so regularisiert sein, dass sich in der ersten Ableitung der Verschiebungsfunktion ein stetiger Übergang zwischen zwei zeitlich benachbarten Abschnittsfunktionen ergibt.

[0019] Die Flächenform, mit der die Positionswerte angenähert werden, kann ebenfalls durch eine mathematische Funktion dargestellt werden. Ein Beispiel für eine Augenstruktur, auf die sich die Positionswerte beziehen können, ist die Oberfläche der Cornea. Eine mögliche Anwendung des erfindungsgemäßen Verfahrens ist es, dass die Flächenform einer Topographie der Cornea entspricht. Die Cornea, wie auch andere Strukturen des Auges, bei denen das Verfahren angewendet werden kann, haben eine kreisrunde Form. Als mathematische Funktion zur Darstellung der Augenstruktur können deswegen Zernike-Polynome verwendet werden, bei denen es sich um innerhalb des Einheitskreises definierte Polynome handelt. Durch Skalierung kann die mit den Zernike-Polynomen abgedeckte Fläche an die Größe der untersuchten Augenstruktur angepasst werden.

[0020] Für die Durchführung der Bewegungskorrektur ist es nicht erforderlich, die Flächenform in der höchstmöglichen mathematischen Genauigkeit darzustellen. Ausreichen kann es, die Flächenform durch Zernike-Polynome niederer Ordnung abzubilden, beispielsweise bis zur vierten Ordnung, bis zur sechsten Ordnung oder bis zur achten Ordnung.

[0021] Zur Ermittlung der Flächenform kann ein Optimierungsproblem formuliert werden, bei dem die Flächenform und die Verschiebungsfunktion gemeinsam variiert werden. Wird die Flächenform durch Zernike-Polynome beschrieben, so können die Koeffizienten der Zernike-Polynome auf diese Weise ermittelt werden. Es kann einen einheitlichen Optimierungsvorgang geben, innerhalb dessen sowohl die Koeffizienten der Polynome der Verschiebungsfunktion als auch die Koeffizienten der Zernike-Polynome ermittelt werden. Es wird also mit einem Optimierungsschritt eine Annäherung sowohl im Hinblick auf die Flächenform als auch im Hinblick auf den Bewegungsablauf während des Messzeitraums durchgeführt.

[0022] Der Messstrahl, mit dem das Auge gescannt wird, kann ein OCT-Messstrahl sein. Bei OCT-Messungen wird kurzkohärentes OCT-Licht in einen Objektstrahlengang und einen Referenzstrahlengang aufgespalten. Der Objektstrahlengang wird als Messstrahl auf das Objekt geleitet. Von dem Objekt zurückgestreute Anteile des OCT-Lichts werden mit dem Licht des Referenzstrahlengangs zur Interferenz gebracht. Aus dem Interferenzmuster kann auf Streuzentren in dem Objekt geschlossen werden. Die OCT-Lichtquelle kann eine Swept-Source-Lichtquelle sein.

[0023] Mit dem Messstrahl kann eine Mehrzahl von A-Scans gewonnen werden. Als A-Scan wird eine Messung bezeichnet, die sich in Richtung des Messstrahls in die Tiefe des Objekts erstreckt. Aus einem solchen A-Scan kann eine Information über die axiale Position einer gesuchten Augenstruktur abgeleitet werden. Ist beispielsweise die gesuchte Augenstruktur die Oberfläche der Cornea, so kann diese Information aus dem A-Scan gewonnen werden. Eine solche aus einem A-Scan abgeleitete Information über die axiale Position einer Augenstruktur ergibt zusammen mit der Position des A-Scans einen Positionswert der Augenstruktur. Durch eine Mehrzahl von A-Scans kann der erfindungsgemäße Satz von Positionswerten der Augenstruktur gewonnen werden. Der Satz von Positionswerte bildet eine Punktwolke, bei der jeder Punkt auf einer Oberfläche der Augenstruktur liegt.

[0024] Vor dem Ermitteln der Verschiebungsfunktion und gegebenenfalls der mathematischen Funktion der Flächenform können unplausible Messwerte aus dem Satz von Positionswerten gestrichen werden. Bei der Messung am Auge ist es beispielsweise möglich, dass der Patient während der Messung blinzelt und der Messstrahl deswegen auf das Augenlid auftritt, statt auf die Oberfläche der Cornea. Die Chunks können so definiert sein, dass sie sich über eine bestimmte Zeit erstrecken, so dass im Ausgangspunkt in allen Chunks die gleiche Anzahl von Positionswerte enthalten ist. Nach dem Streichen von unplausiblen Messwerten kann die Zahl der Positionswerte sich zwischen den Chunks unterscheiden. Auch leere Chunks, in denen keine Positionswerte enthalten sind, können auf diese Weise entstehen. Leere Chunks werden beim Zusammensetzen der Verschiebungsfunktion aus Abschnittsfunktionen berücksichtigt, indem zwei Chunks, zwischen denen ein leerer Chunk angeordnet ist, nicht als benachbarte Chunks gelten.

[0025] Das Abtastmuster, mit dem der Messstrahl das Auge abtastet, kann so gewählt sein, dass in jedem Chunk Messdaten von der gesamten untersuchten Augenstruktur enthalten sind. Mit anderen Worten kann für jeden der Chunks gelten, dass innerhalb der mit dem Messstrahl überstrichenen Fläche jeder Kreis, der eine Fläche von mehr als 10 %, vorzugsweise von mehr als 5 %, weiter vorzugsweise von mehr als 2 % innerhalb der überstrichenen Fläche abdeckt, wenigstens einen Messwert enthält. Dies gilt für den Zustand, bevor unplausible Messwerte gestrichen wurden.

[0026] Das Scannen des Auges mit dem Messstrahl kann so durchgeführt werden, dass der Messstrahl in seitlicher Richtung abgelenkt wird, so dass er eine Kurve auf der Oberfläche des Auges beschreibt. Entlang der Kurve kann die gewünschte Sequenz von A-Scans aufgenommen werden.

[0027] Die Kurve kann so gestaltet sein, dass abrupte Richtungsänderungen, die eine hohe Belastung für die Scaneinrichtung darstellen, vermieden werden. Die Kurve kann beispielsweise die folgende Form haben.

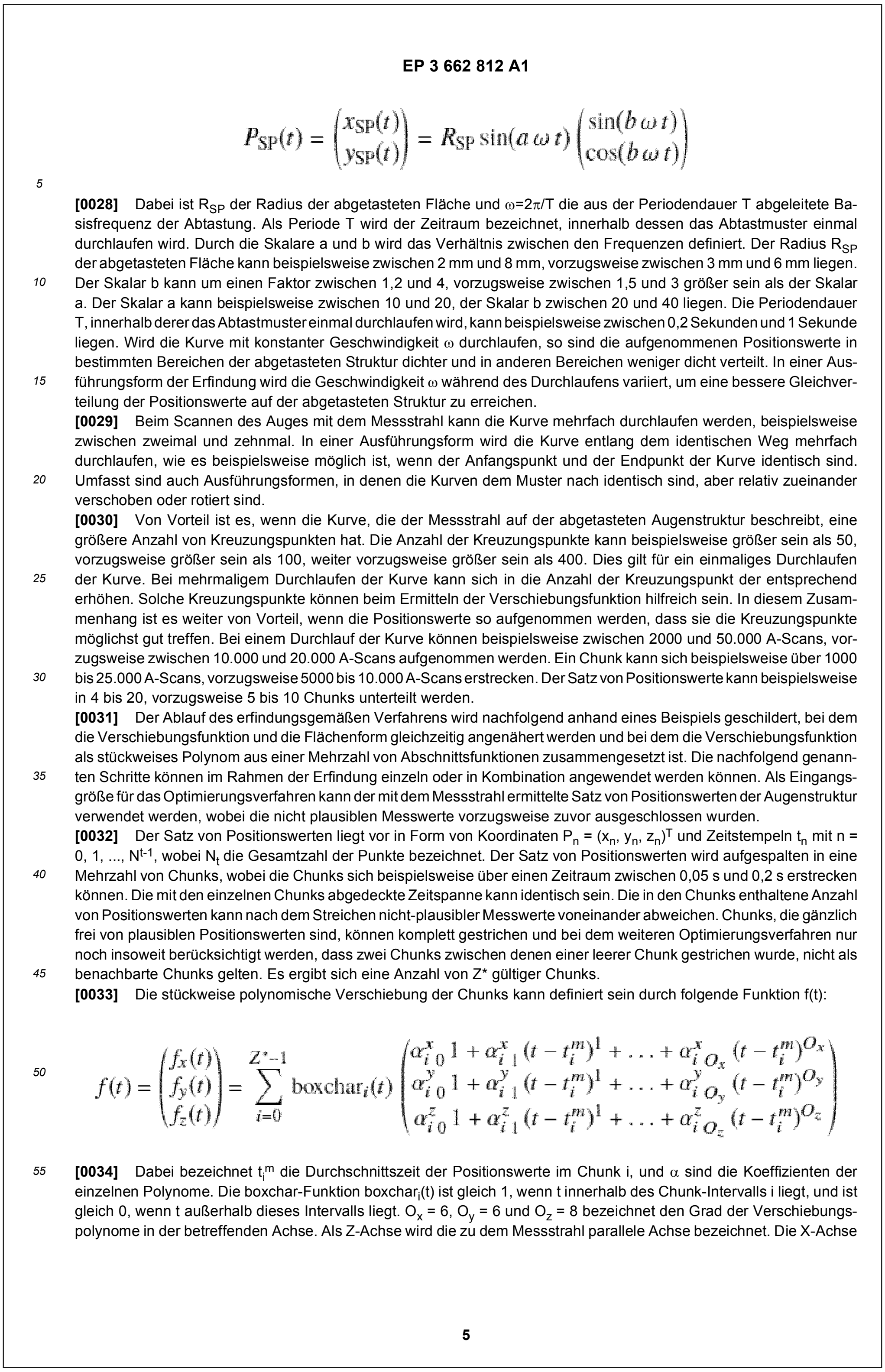

$$P_{\mathrm{SP}}(t) = \begin{pmatrix} x_{\mathrm{SP}}(t) \\ y_{\mathrm{SP}}(t) \end{pmatrix} = R_{\mathrm{SP}} \sin(a\,\omega\,t) \begin{pmatrix} \sin(b\,\omega\,t) \\ \cos(b\,\omega\,t) \end{pmatrix}$$

[0028] Dabei ist R_{SP} der Radius der abgetasteten Fläche und $\omega=2\pi/T$ die aus der Periodendauer T abgeleitete Basisfrequenz der Abtastung. Als Periode T wird der Zeitraum bezeichnet, innerhalb dessen das Abtastmuster einmal durchlaufen wird. Durch die Skalare a und b wird das Verhältnis zwischen den Frequenzen definiert. Der Radius R_{SP} der abgetasteten Fläche kann beispielsweise zwischen 2 mm und 8 mm, vorzugsweise zwischen 3 mm und 6 mm liegen. Der Skalar b kann um einen Faktor zwischen 1,2 und 4, vorzugsweise zwischen 1,5 und 3 größer sein als der Skalar a. Der Skalar a kann beispielsweise zwischen 10 und 20, der Skalar b zwischen 20 und 40 liegen. Die Periodendauer T, innerhalb derer das Abtastmuster einmal durchlaufen wird, kann beispielsweise zwischen 0,2 Sekunden und 1 Sekunde liegen. Wird die Kurve mit konstanter Geschwindigkeit ω durchlaufen, so sind die aufgenommenen Positionswerte in bestimmten Bereichen der abgetasteten Struktur dichter und in anderen Bereichen weniger dicht verteilt. In einer Ausführungsform der Erfindung wird die Geschwindigkeit ω während des Durchlaufens variiert, um eine bessere Gleichverteilung der Positionswerte auf der abgetasteten Struktur zu erreichen.

[0029] Beim Scannen des Auges mit dem Messstrahl kann die Kurve mehrfach durchlaufen werden, beispielsweise zwischen zweimal und zehnmal. In einer Ausführungsform wird die Kurve entlang dem identischen Weg mehrfach durchlaufen, wie es beispielsweise möglich ist, wenn der Anfangspunkt und der Endpunkt der Kurve identisch sind. Umfasst sind auch Ausführungsformen, in denen die Kurven dem Muster nach identisch sind, aber relativ zueinander verschoben oder rotiert sind.

[0030] Von Vorteil ist es, wenn die Kurve, die der Messstrahl auf der abgetasteten Augenstruktur beschreibt, eine größere Anzahl von Kreuzungspunkten hat. Die Anzahl der Kreuzungspunkte kann beispielsweise größer sein als 50, vorzugsweise größer sein als 100, weiter vorzugsweise größer sein als 400. Dies gilt für ein einmaliges Durchlaufen der Kurve. Bei mehrmaligem Durchlaufen der Kurve kann sich in die Anzahl der Kreuzungspunkt der entsprechend erhöhen. Solche Kreuzungspunkte können beim Ermitteln der Verschiebungsfunktion hilfreich sein. In diesem Zusammenhang ist es weiter von Vorteil, wenn die Positionswerte so aufgenommen werden, dass sie die Kreuzungspunkte möglichst gut treffen. Bei einem Durchlauf der Kurve können beispielsweise zwischen 2000 und 50.000 A-Scans, vorzugsweise zwischen 10.000 und 20.000 A-Scans aufgenommen werden. Ein Chunk kann sich beispielsweise über 1000 bis 25.000 A-Scans, vorzugsweise 5000 bis 10.000 A-Scans erstrecken. Der Satz von Positionswerte kann beispielsweise in 4 bis 20, vorzugsweise 5 bis 10 Chunks unterteilt werden.

[0031] Der Ablauf des erfindungsgemäßen Verfahrens wird nachfolgend anhand eines Beispiels geschildert, bei dem die Verschiebungsfunktion und die Flächenform gleichzeitig angenähert werden und bei dem die Verschiebungsfunktion als stückweises Polynom aus einer Mehrzahl von Abschnittsfunktionen zusammengesetzt ist. Die nachfolgend genannten Schritte können im Rahmen der Erfindung einzeln oder in Kombination angewendet werden können. Als Eingangsgröße für das Optimierungsverfahren kann der mit dem Messstrahl ermittelte Satz von Positionswerten der Augenstruktur verwendet werden, wobei die nicht plausiblen Messwerte vorzugsweise zuvor ausgeschlossen wurden.

[0032] Der Satz von Positionswerten liegt vor in Form von Koordinaten $P_n = (x_n, y_n, z_n)^T$ und Zeitstempeln t_n mit n = 0, 1, ..., N^{t-1}, wobei N_t die Gesamtzahl der Punkte bezeichnet. Der Satz von Positionswerten wird aufgespalten in eine Mehrzahl von Chunks, wobei die Chunks sich beispielsweise über einen Zeitraum zwischen 0,05 s und 0,2 s erstrecken können. Die mit den einzelnen Chunks abgedeckte Zeitspanne kann identisch sein. Die in den Chunks enthaltene Anzahl von Positionswerten kann nach dem Streichen nicht-plausibler Messwerte voneinander abweichen. Chunks, die gänzlich frei von plausiblen Positionswerten sind, können komplett gestrichen und bei dem weiteren Optimierungsverfahren nur noch insoweit berücksichtigt werden, dass zwei Chunks zwischen denen einer leerer Chunk gestrichen wurde, nicht als benachbarte Chunks gelten. Es ergibt sich eine Anzahl von Z* gültiger Chunks.

[0033] Die stückweise polynomische Verschiebung der Chunks kann definiert sein durch folgende Funktion f(t):

$$f(t) = \begin{pmatrix} f_x(t) \\ f_y(t) \\ f_z(t) \end{pmatrix} = \sum_{i=0}^{Z^*-1} \mathrm{boxchar}_i(t) \begin{pmatrix} \alpha^x_{i\,0}\,1 + \alpha^x_{i\,1}\,(t - t^m_i)^1 + \ldots + \alpha^x_{i\,O_x}\,(t - t^m_i)^{O_x} \\ \alpha^y_{i\,0}\,1 + \alpha^y_{i\,1}\,(t - t^m_i)^1 + \ldots + \alpha^y_{i\,O_y}\,(t - t^m_i)^{O_y} \\ \alpha^z_{i\,0}\,1 + \alpha^z_{i\,1}\,(t - t^m_i)^1 + \ldots + \alpha^z_{i\,O_z}\,(t - t^m_i)^{O_z} \end{pmatrix}$$

[0034] Dabei bezeichnet t_i^m die Durchschnittszeit der Positionswerte im Chunk i, und α sind die Koeffizienten der einzelnen Polynome. Die boxchar-Funktion $\mathrm{boxchar}_i(t)$ ist gleich 1, wenn t innerhalb des Chunk-Intervalls i liegt, und ist gleich 0, wenn t außerhalb dieses Intervalls liegt. $O_x = 6$, $O_y = 6$ und $O_z = 8$ bezeichnet den Grad der Verschiebungspolynome in der betreffenden Achse. Als Z-Achse wird die zu dem Messstrahl parallele Achse bezeichnet. Die X-Achse und Y-Achse sind orthogonal dazu.

[0035] Die Koeffizienten der Verschiebungspolynome werden bestimmt durch Lösen des folgenden Näherungsproblems der kleinsten mittleren Quadrate:

$$\underset{\beta,\,\mathbf{p}}{\text{minimize}} \quad \left\| \begin{pmatrix} \mathbf{Z} & \mathbf{M} \\ \mathbf{0} & \mathbf{C} \end{pmatrix} \begin{pmatrix} \boldsymbol{\beta} \\ \boldsymbol{\alpha} \end{pmatrix} - \begin{pmatrix} \mathbf{z} \\ \mathbf{0} \end{pmatrix} \right\|_2^2$$

[0036] Dabei ist β ein Reihenvektor mit den Zernike-Koeffizienten und α ein Reihenvektor mit den Koeffizienten der Verschiebungspolynome. Die Spalten der Matrix Z enthalten die Zernike-Polynome, die an den x,y-Koordinaten aufgenommen wurden, während z die z-Koordinaten der Positionswerte repräsentiert. Die Matrix M enthält die polynomischen Basisfunktionen für die Verschiebung in jedem Chunk und α die entsprechenden Koeffizienten:

$$\mathbf{M} = \begin{pmatrix} \mathbf{M}_0 & \mathbf{0} & \ddots & \mathbf{0} \\ \mathbf{0} & \mathbf{M}_1 & \ddots & \mathbf{0} \\ \ddots & \ddots & \ddots & \ddots \\ \mathbf{0} & \mathbf{0} & \ddots & \mathbf{M}_{Z^*-1} \end{pmatrix}$$

$$\boldsymbol{\alpha} = \begin{pmatrix} \boldsymbol{\alpha}_0 & \boldsymbol{\alpha}_1 & \ldots & \boldsymbol{\alpha}_{Z^*-1} \end{pmatrix}^T$$

[0037] M_i enthält die Verschiebungs-Basisfunktion in allen drei Achsen und α_i sind die Koeffizienten der Verschiebungs-Polynome in allen drei Achsen für den spezifischen Chunk_i.

$$\mathbf{M}_i = \begin{pmatrix} \mathbf{M}_i^x & \mathbf{M}_i^y & \mathbf{M}_i^z \end{pmatrix}$$

$$\boldsymbol{\alpha}_i = \begin{pmatrix} \boldsymbol{\alpha}_i^x & \boldsymbol{\alpha}_i^y & \boldsymbol{\alpha}_i^z \end{pmatrix}^T = \begin{pmatrix} \alpha_{i\,0}^x & \cdots & \alpha_{i\,O_x}^x & \alpha_{i\,0}^y & \cdots & \alpha_{i\,O_y}^y & \alpha_{i\,0}^z & \cdots & \alpha_{i\,O_z}^z \end{pmatrix}^T$$

[0038] Die Spalten von M_i^x, M_i^y, M_i^z repräsentieren die Verschiebungs-Basisfunktionen in den betreffenden Richtungen. Die Verschiebungs-Basisfunktionen für die x- und y-Richtung werden geschätzt auf Basis eines anfänglichen Zernike-Fits auf die Wolke von Positionswerte. Die Ordnung des Zernike-Fits kann beispielsweise zwischen 4 und 8, vorzugsweise bei 6 liegen. Jeder Eintrag wird ermittelt durch partielle Ableitung der Zernike-Oberfläche bei den x-,y-Koordinaten der betreffenden Punkte n und Ordnung m.

$$\mathbf{M}_{i\;n,m}^x = \frac{d}{dx} Z(x_n, y_n) \times (t_n - T_i)^m$$

$$\mathbf{M}_{i\;n,m}^y = \frac{d}{dy} Z(x_n, y_n) \times (t_n - T_i)^m$$

[0039] Für die Z-Richtung vereinfacht sich dies zu:

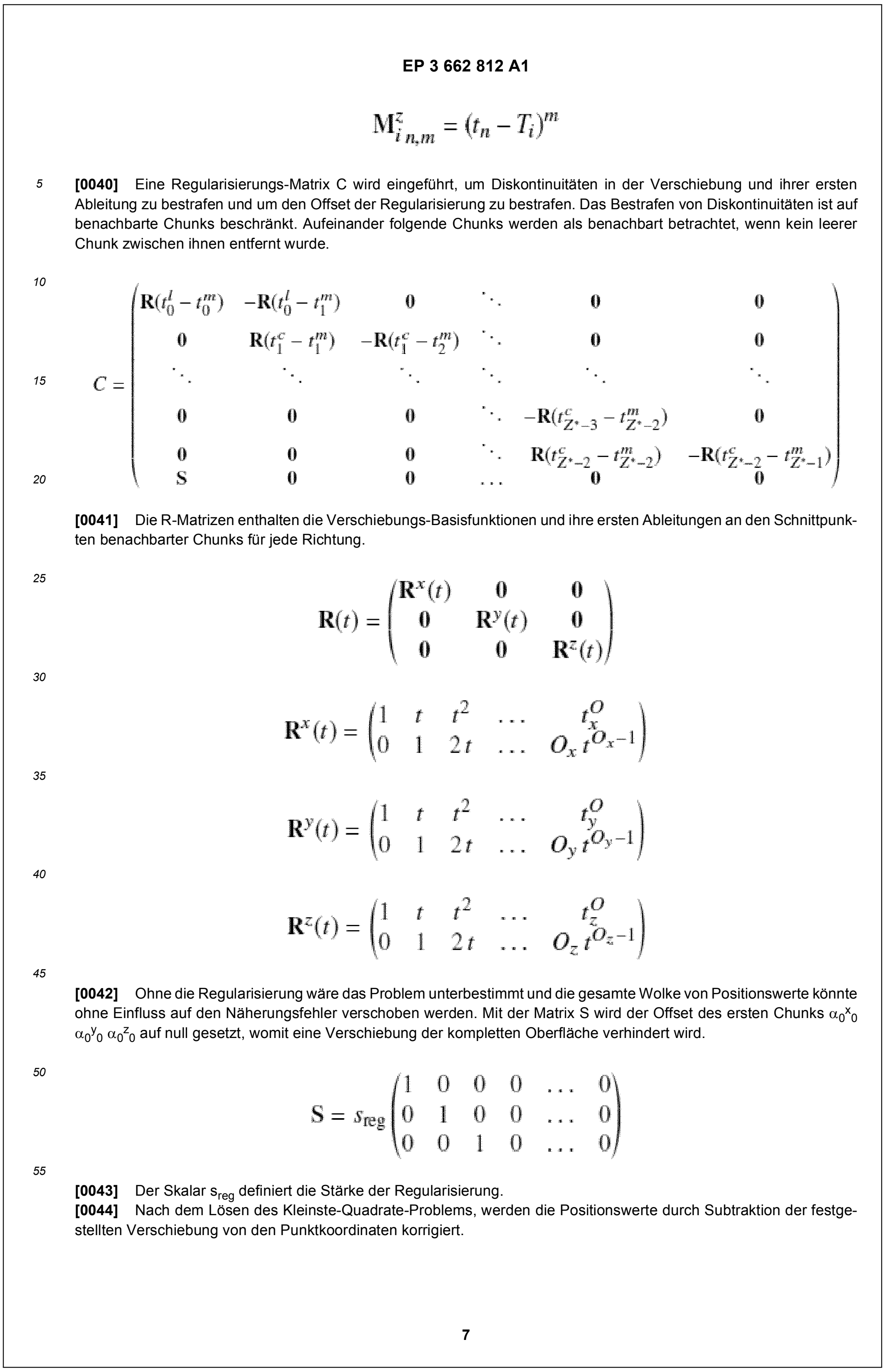

EP 3 662 812 A1

$$\mathbf{M}^{z}_{i\,n,m} = (t_n - T_i)^m$$

[0040] Eine Regularisierungs-Matrix C wird eingeführt, um Diskontinuitäten in der Verschiebung und ihrer ersten Ableitung zu bestrafen und um den Offset der Regularisierung zu bestrafen. Das Bestrafen von Diskontinuitäten ist auf benachbarte Chunks beschränkt. Aufeinander folgende Chunks werden als benachbart betrachtet, wenn kein leerer Chunk zwischen ihnen entfernt wurde.

$$C = \begin{pmatrix} \mathbf{R}(t_0^l - t_0^m) & -\mathbf{R}(t_0^l - t_1^m) & \mathbf{0} & \ddots & \mathbf{0} & \mathbf{0} \\ \mathbf{0} & \mathbf{R}(t_1^c - t_1^m) & -\mathbf{R}(t_1^c - t_2^m) & \ddots & \mathbf{0} & \mathbf{0} \\ \ddots & \ddots & \ddots & \ddots & \ddots & \ddots \\ \mathbf{0} & \mathbf{0} & \mathbf{0} & \ddots & -\mathbf{R}(t_{Z^*-3}^c - t_{Z^*-2}^m) & \mathbf{0} \\ \mathbf{0} & \mathbf{0} & \mathbf{0} & \ddots & \mathbf{R}(t_{Z^*-2}^c - t_{Z^*-2}^m) & -\mathbf{R}(t_{Z^*-2}^c - t_{Z^*-1}^m) \\ \mathbf{S} & \mathbf{0} & \mathbf{0} & \dots & \mathbf{0} & \mathbf{0} \end{pmatrix}$$

[0041] Die R-Matrizen enthalten die Verschiebungs-Basisfunktionen und ihre ersten Ableitungen an den Schnittpunkten benachbarter Chunks für jede Richtung.

$$\mathbf{R}(t) = \begin{pmatrix} \mathbf{R}^x(t) & \mathbf{0} & \mathbf{0} \\ \mathbf{0} & \mathbf{R}^y(t) & \mathbf{0} \\ \mathbf{0} & \mathbf{0} & \mathbf{R}^z(t) \end{pmatrix}$$

$$\mathbf{R}^x(t) = \begin{pmatrix} 1 & t & t^2 & \dots & t^{O}_{x} \\ 0 & 1 & 2t & \dots & O_x\, t^{O_x - 1} \end{pmatrix}$$

$$\mathbf{R}^y(t) = \begin{pmatrix} 1 & t & t^2 & \dots & t^{O}_{y} \\ 0 & 1 & 2t & \dots & O_y\, t^{O_y - 1} \end{pmatrix}$$

$$\mathbf{R}^z(t) = \begin{pmatrix} 1 & t & t^2 & \dots & t^{O}_{z} \\ 0 & 1 & 2t & \dots & O_z\, t^{O_z - 1} \end{pmatrix}$$

[0042] Ohne die Regularisierung wäre das Problem unterbestimmt und die gesamte Wolke von Positionswerte könnte ohne Einfluss auf den Näherungsfehler verschoben werden. Mit der Matrix S wird der Offset des ersten Chunks $\alpha_0{}^{x}{}_0$ $\alpha_0{}^{y}{}_0$ $\alpha_0{}^{z}{}_0$ auf null gesetzt, womit eine Verschiebung der kompletten Oberfläche verhindert wird.

$$\mathbf{S} = s_{\text{reg}} \begin{pmatrix} 1 & 0 & 0 & 0 & \dots & 0 \\ 0 & 1 & 0 & 0 & \dots & 0 \\ 0 & 0 & 1 & 0 & \dots & 0 \end{pmatrix}$$

[0043] Der Skalar s_{reg} definiert die Stärke der Regularisierung.

[0044] Nach dem Lösen des Kleinste-Quadrate-Problems, werden die Positionswerte durch Subtraktion der festgestellten Verschiebung von den Punktkoordinaten korrigiert.

7

$$P_n^* = P_n - f(t_n) \quad \text{for } n = 0, 1, \ldots N^T - 1$$

[0045] Nachdem die Verschiebungsfunktion ermittelt wurde, kann eine Qualitätsüberprüfung durchgeführt werden. Wurde das Optimierungsverfahren auf Basis von N Chunks durchgeführt, so können durch Ausschließen jeweils einzelner Chunks N verschiedene Subsets gebildet werden, die jeweils N-1 Chunks umfassen.

[0046] Für jedes der Subsets kann die Koeffizienten-Standardabweichung einer Zernike-Rekonstruktion bestimmt werden. Der Grad der Zernike-Rekonstruktion kann höher sein als der Grad der Zernike-Rekonstruktion beim Ermitteln der Verschiebungsfunktion, insbesondere kann der Grad um 1 erhöht sein. Beispielsweise kann eine Zernike-Rekonstruktion siebten Grades durchgeführt werden. Ist die kleinste Koeffizienten-Standardabweichung für eines der Subsets kleiner als die Koeffizienten-Standardabweichung über alle Chunks, so kann das betreffende Subset an die Stelle der vorherigen Gesamtheit der Daten treten. In Folge der Qualitätsüberprüfung kann also mit einem reduzierten Satz von Positionswerte fortgefahren werden, in dem die Positionswerte eines Chunks gestrichen sind. Die Qualitätsüberprüfung kann iterativ fortgesetzt, bis die Koeffizienten-Standardabweichung der (verbleibenden) Gesamtdaten kleiner ist als die Koeffizienten-Standardabweichung von jedem der Subsets.

[0047] Auf Basis der Positionswerte, die anhand der Verschiebungsfunktion korrigiert wurden, kann die Form der Augenstruktur (beispielsweise die Topographie der Cornea-Oberfläche) rekonstruiert werden. Dafür kann eine Zernike-Rekonstruktion auf die korrigierten Positionswerte angewendet werden. Der Grad der Zernike-Rekonstruktion kann höher sein als der Grad der Zernike-Polynome, mit dem die Flächenform beim Ermitteln der Verschiebungsfunktion dargestellt wird. Beispielsweise kann eine Zernike-Rekonstruktion mit Zernike-Polynome bis zum 10. Grad durchgeführt werden.

[0048] Daraus können dann weitere für den Nutzer wertvolle Informationen abgeleitet werden, wie beispielsweise Krümmungs-Karten der Cornea-Vorderseite und -Rückseite sowie eine Kartendarstellung der Hornhautdicke. Auch bewegungskorrigierte Schnittbilder können berechnet werden, oder andere Augenstrukturen, wie beispielsweise die Augenlinse, können bewegungsfrei vermessen werden.

[0049] Die Erfindung betrifft außerdem ein zugehöriges Messsystem. Das Messsystem umfasst einen Messstrahl und eine Scaneinrichtung, um den Messstrahl in seitlicher Richtung abzulenken. Mit einem Detektor wird aus einem von dem Messstrahl erzeugten Signal ein Satz von Positionswerten einer Augenstruktur bereitstellt, wobei die Positionswerte jeweils mit einem Zeitstempel innerhalb eines Messzeitraums versehen sind. Eine Auswerteeinheit ist dazu ausgelegt, eine Flächenform zu ermitteln und eine Verschiebungsfunktion zu ermitteln, wobei die Verschiebungsfunktion einen Bewegungsablauf während des Messzeitraums darstellt, und wobei die Flächenform und die Verschiebungsfunktion derart ermittelt werden, dass die Positionswerte durch die Flächenform angenähert werden, wenn die Flächenform gemäß der Verschiebungsfunktion bewegt wird.

[0050] Das Messsystem kann mit weiteren Merkmalen fortgebildet werden, die im Zusammenhang des erfindungsgemäßen Verfahrens beschrieben sind. Das Verfahren kann mit weiteren Merkmalen fortgebildet werden, die im Zusammenhang des erfindungsgemäßen Messsystems beschrieben sind.

[0051] Die Erfindung wird nachfolgend unter Bezugnahme auf die beigefügten Zeichnungen anhand vorteilhafter Ausführungsformen beispielhaft beschrieben. Es zeigen:

Fig. 1:	eine schematische Darstellung eines erfindungsgemäßen Messsystems;
Fig. 2:	eine erfindungsgemäße Abtastkurve;
Fig. 3:	die zu Fig. 2 gehörige Ablenkung der Scaneinrichtung in X-Richtung und Y-Richtung;
Fig. 4:	die tatsächliche Verschiebung eines Objekts in X-Richtung, Y-Richtung und Z-Richtung;
Fig. 5:	eine zu Fig. 4 gehörige Verschiebungsfunktion, die mit dem erfindungsgemäßen Verfahren ermittelt wurde;
Fig. 6:	eine grafische Darstellung eines Satzes von Positionswerte.

[0052] Mit einem in Fig. 1 gezeigten OCT-Messsystem wird ein Messobjekts 14 in Form eines menschlichen Auges abgetastet. Indem OCT-Licht 15 auf das Messobjekt 14 gerichtet wird, wird eine Bildinformation gewonnen, die sich entlang der Achse des OCT-Strahls in die Tiefe des Messobjekts 14 erstreckt (A-Scan). Indem der OCT-Strahl in einer dazu senkrechten Richtung über das Messobjekt 14 gescannt wird, kann aus einer Vielzahl von A-Scans ein dreidimensionales Bild des Messobjekts 14 zusammengesetzt werden. Während der Zeitspanne, die das Scannen des Auges in Anspruch nimmt, kann das Auge sich bewegen, was sich negativ auf die Qualität der Bildinformation auswirken kann.

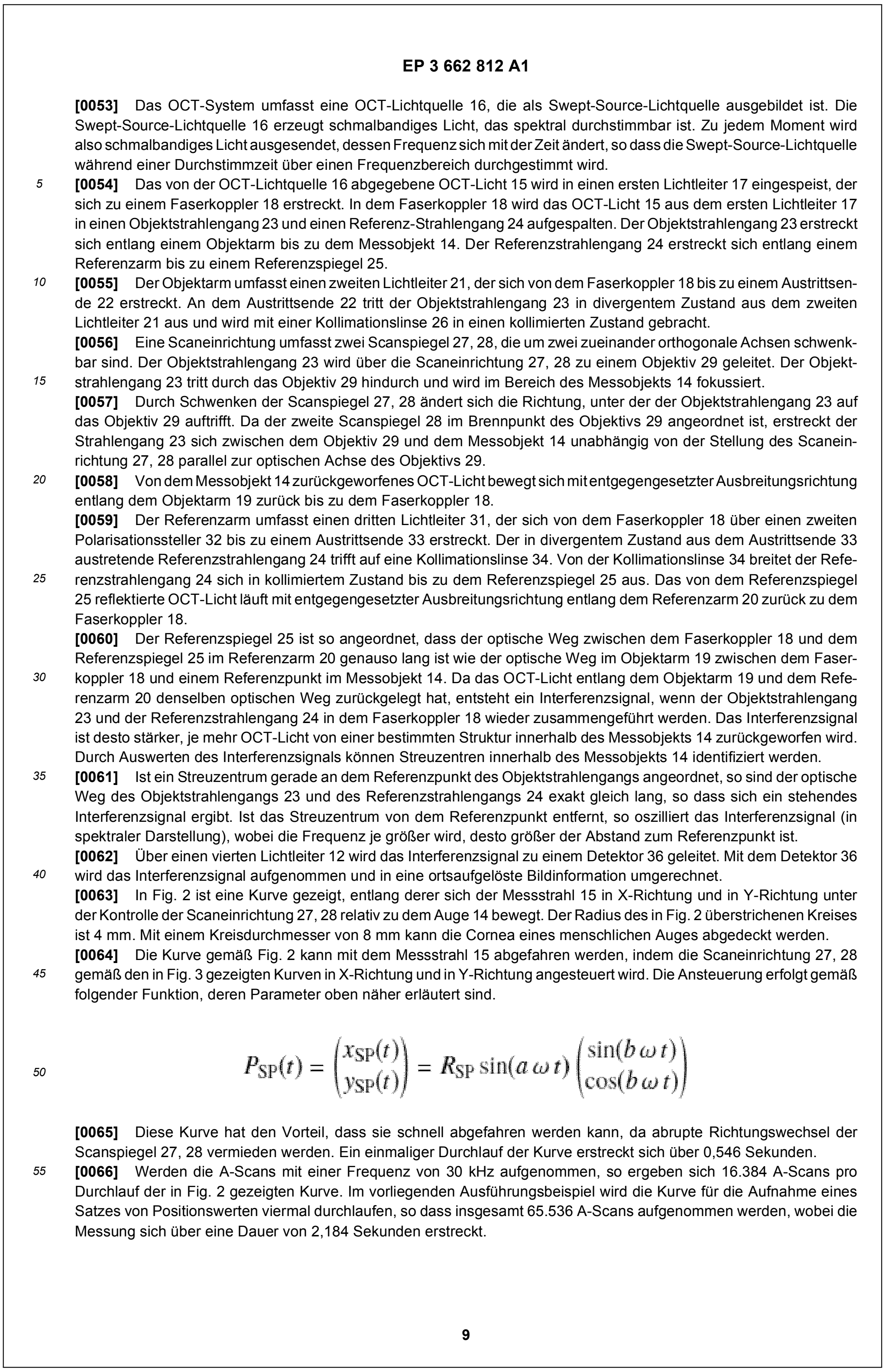

[0053] Das OCT-System umfasst eine OCT-Lichtquelle 16, die als Swept-Source-Lichtquelle ausgebildet ist. Die Swept-Source-Lichtquelle 16 erzeugt schmalbandiges Licht, das spektral durchstimmbar ist. Zu jedem Moment wird also schmalbandiges Licht ausgesendet, dessen Frequenz sich mit der Zeit ändert, so dass die Swept-Source-Lichtquelle während einer Durchstimmzeit über einen Frequenzbereich durchgestimmt wird.

[0054] Das von der OCT-Lichtquelle 16 abgegebene OCT-Licht 15 wird in einen ersten Lichtleiter 17 eingespeist, der sich zu einem Faserkoppler 18 erstreckt. In dem Faserkoppler 18 wird das OCT-Licht 15 aus dem ersten Lichtleiter 17 in einen Objektstrahlengang 23 und einen Referenz-Strahlengang 24 aufgespalten. Der Objektstrahlengang 23 erstreckt sich entlang einem Objektarm bis zu dem Messobjekt 14. Der Referenzstrahlengang 24 erstreckt sich entlang einem Referenzarm bis zu einem Referenzspiegel 25.

[0055] Der Objektarm umfasst einen zweiten Lichtleiter 21, der sich von dem Faserkoppler 18 bis zu einem Austrittsende 22 erstreckt. An dem Austrittsende 22 tritt der Objektstrahlengang 23 in divergentem Zustand aus dem zweiten Lichtleiter 21 aus und wird mit einer Kollimationslinse 26 in einen kollimierten Zustand gebracht.

[0056] Eine Scaneinrichtung umfasst zwei Scanspiegel 27, 28, die um zwei zueinander orthogonale Achsen schwenkbar sind. Der Objektstrahlengang 23 wird über die Scaneinrichtung 27, 28 zu einem Objektiv 29 geleitet. Der Objektstrahlengang 23 tritt durch das Objektiv 29 hindurch und wird im Bereich des Messobjekts 14 fokussiert.

[0057] Durch Schwenken der Scanspiegel 27, 28 ändert sich die Richtung, unter der der Objektstrahlengang 23 auf das Objektiv 29 auftrifft. Da der zweite Scanspiegel 28 im Brennpunkt des Objektivs 29 angeordnet ist, erstreckt der Strahlengang 23 sich zwischen dem Objektiv 29 und dem Messobjekt 14 unabhängig von der Stellung des Scaneinrichtung 27, 28 parallel zur optischen Achse des Objektivs 29.

[0058] Von dem Messobjekt 14 zurückgeworfenes OCT-Licht bewegt sich mit entgegengesetzter Ausbreitungsrichtung entlang dem Objektarm 19 zurück bis zu dem Faserkoppler 18.

[0059] Der Referenzarm umfasst einen dritten Lichtleiter 31, der sich von dem Faserkoppler 18 über einen zweiten Polarisationssteller 32 bis zu einem Austrittsende 33 erstreckt. Der in divergentem Zustand aus dem Austrittsende 33 austretende Referenzstrahlengang 24 trifft auf eine Kollimationslinse 34. Von der Kollimationslinse 34 breitet der Referenzstrahlengang 24 sich in kollimiertem Zustand bis zu dem Referenzspiegel 25 aus. Das von dem Referenzspiegel 25 reflektierte OCT-Licht läuft mit entgegengesetzter Ausbreitungsrichtung entlang dem Referenzarm 20 zurück zu dem Faserkoppler 18.

[0060] Der Referenzspiegel 25 ist so angeordnet, dass der optische Weg zwischen dem Faserkoppler 18 und dem Referenzspiegel 25 im Referenzarm 20 genauso lang ist wie der optische Weg im Objektarm 19 zwischen dem Faserkoppler 18 und einem Referenzpunkt im Messobjekt 14. Da das OCT-Licht entlang dem Objektarm 19 und dem Referenzarm 20 denselben optischen Weg zurückgelegt hat, entsteht ein Interferenzsignal, wenn der Objektstrahlengang 23 und der Referenzstrahlengang 24 in dem Faserkoppler 18 wieder zusammengeführt werden. Das Interferenzsignal ist desto stärker, je mehr OCT-Licht von einer bestimmten Struktur innerhalb des Messobjekts 14 zurückgeworfen wird. Durch Auswerten des Interferenzsignals können Streuzentren innerhalb des Messobjekts 14 identifiziert werden.

[0061] Ist ein Streuzentrum gerade an dem Referenzpunkt des Objektstrahlengangs angeordnet, so sind der optische Weg des Objektstrahlengangs 23 und des Referenzstrahlengangs 24 exakt gleich lang, so dass sich ein stehendes Interferenzsignal ergibt. Ist das Streuzentrum von dem Referenzpunkt entfernt, so oszilliert das Interferenzsignal (in spektraler Darstellung), wobei die Frequenz je größer wird, desto größer der Abstand zum Referenzpunkt ist.

[0062] Über einen vierten Lichtleiter 12 wird das Interferenzsignal zu einem Detektor 36 geleitet. Mit dem Detektor 36 wird das Interferenzsignal aufgenommen und in eine ortsaufgelöste Bildinformation umgerechnet.

[0063] In Fig. 2 ist eine Kurve gezeigt, entlang derer sich der Messstrahl 15 in X-Richtung und in Y-Richtung unter der Kontrolle der Scaneinrichtung 27, 28 relativ zu dem Auge 14 bewegt. Der Radius des in Fig. 2 überstrichenen Kreises ist 4 mm. Mit einem Kreisdurchmesser von 8 mm kann die Cornea eines menschlichen Auges abgedeckt werden.

[0064] Die Kurve gemäß Fig. 2 kann mit dem Messstrahl 15 abgefahren werden, indem die Scaneinrichtung 27, 28 gemäß den in Fig. 3 gezeigten Kurven in X-Richtung und in Y-Richtung angesteuert wird. Die Ansteuerung erfolgt gemäß folgender Funktion, deren Parameter oben näher erläutert sind.

$$P_{\mathrm{SP}}(t) = \begin{pmatrix} x_{\mathrm{SP}}(t) \\ y_{\mathrm{SP}}(t) \end{pmatrix} = R_{\mathrm{SP}} \sin(a\,\omega\,t) \begin{pmatrix} \sin(b\,\omega\,t) \\ \cos(b\,\omega\,t) \end{pmatrix}$$

[0065] Diese Kurve hat den Vorteil, dass sie schnell abgefahren werden kann, da abrupte Richtungswechsel der Scanspiegel 27, 28 vermieden werden. Ein einmaliger Durchlauf der Kurve erstreckt sich über 0,546 Sekunden.

[0066] Werden die A-Scans mit einer Frequenz von 30 kHz aufgenommen, so ergeben sich 16.384 A-Scans pro Durchlauf der in Fig. 2 gezeigten Kurve. Im vorliegenden Ausführungsbeispiel wird die Kurve für die Aufnahme eines Satzes von Positionswerten viermal durchlaufen, so dass insgesamt 65.536 A-Scans aufgenommen werden, wobei die Messung sich über eine Dauer von 2,184 Sekunden erstreckt.

[0067] In Fig. 6 ist die während einer Messung mit dem Detektor 36 ermittelte Bildinformation grafisch dargestellt, indem einige der 65.536 A-Scans so nebeneinander angeordnet sind, dass sich ein durchgehendes Schnittbild ergibt. Die Messung wird in 16 zeitlich aufeinanderfolgende Chunks 35 aufgeteilt, von denen einer in Fig. 6 vollständig und zwei benachbarte ausschnittsweise dargestellt sind.

[0068] In der Messung gibt es große Abschnitte 36 mit plausiblen Messwerten und kleinere Abschnitte 37 mit nicht plausiblen Messwerten, bei denen das Auge durch das Augenlid bedeckt ist. Die Messwerte der nicht plausiblen Abschnitte 37 werden aus den Chunks 35 gelöscht. Es verbleibt eine reduzierte Anzahl von A-Scans, in denen jeweils eine Ortsinformation über die Position der Cornea-Oberfläche in Z-Richtung entnommen werden kann. Zusammen mit der Position des Messstrahls 15 in X-Richtung und Y-Richtung ergibt sich ein Satz von Positionswerte der Cornea-Oberfläche.

[0069] Mit dem erfindungsgemäßen Verfahren werden aus den Positionswerten eine Flächenform und eine Verschiebungsfunktion 38 in Form eines stückweisen Polynoms ermittelt. Die einzelnen Verfahrensschritte zur Ermittlung der Verschiebungsfunktion 38 und der Flächenform sind oben näher erläutert. Mit der Verschiebungsfunktion 38 wird die Beziehung zwischen den Positionswerten der verschiedenen Chunks 35 als translatorische Verschiebung beschrieben.

[0070] In Fig. 5 ist ein Beispiel einer solchen Verschiebungsfunktion 38 in X-Richtung, Y-Richtung und in Z-Richtung dargestellt. In den drei übereinander angeordneten Graphen ist jeweils die Translation in Mikrometern über der Zeit in Sekunden aufgetragen. Die Verschiebungskurve 38 stammt von einem Versuch, bei dem die tatsächliche Bewegung des Messobjekts 14 den in Fig. 4 gezeigten Verlauf hatte. Es zeigt sich, dass die Verschiebungen 38 den tatsächlichen Verlauf der Bewegung gut wiedergeben.

[0071] Aus der Verschiebungsfunktion 38 kann abgelesen werden, in welcher Weise das Auge während der Aufnahme der Positionswerte translatorisch gegeneinander verschoben wurde. Die Positionswerte können gemäß der Verschiebungsfunktion relativ zueinander verschoben werden, so dass die mit der Verschiebungsfunktion 38 ermittelte Translation ausgeglichen wird. Es ergibt sich ein bewegungskorrigierter Satz von Positionswerte, der die Oberfläche der Cornea beschreibt.

[0072] Aus diesem Satz von Positionswerte kann die Topographie der Cornea mit einer Zernike-Rekonstruktion höherer Ordnung (zum Beispiel 10. Ordnung) rekonstruiert werden. Es können bewegungskorrigierte Schnittbilder berechnet werden, oder andere Augenstrukturen, wie beispielsweise die Augenlinse, bewegungsfrei vermessen werden.

Patentansprüche

1. Verfahren zum Durchführen einer Bewegungskorrektur bei Messungen an einem menschlichen Auge (14), mit folgenden Schritten:

   a. Scannen des Auges (14) mit einem Messstrahl (15), um einen Satz von Positionswerten (39) der Augenstruktur(40) zu gewinnen, wobei das Scannen sich über einen Messzeitraum erstreckt und wobei die Positionswerte (39) jeweils mit einem Zeitstempel innerhalb des Messzeitraums versehen sind;
   b. Ermitteln einer Flächenform und Ermitteln einer Verschiebungsfunktion (38), wobei die Verschiebungsfunktion (38) einen Bewegungsablauf während des Messzeitraums darstellt, und wobei die Flächenform und die Verschiebungsfunktion (38) derart ermittelt werden, dass die Positionswerte (39) durch die Flächenform angenähert werden, wenn die Flächenform gemäß der Verschiebungsfunktion (38) bewegt wird.

2. Verfahren nach Anspruch 1, **dadurch gekennzeichnet, dass** die Positionswerte (39) anhand der Verschiebungsfunktion (38) korrigiert werden.

3. Verfahren nach Anspruch 1 oder 2, **dadurch gekennzeichnet, dass** eine bewegungskorrigierte Topographie der Cornea ermittelt wird.

4. Verfahren nach einem der Ansprüche 1 bis 3, **dadurch gekennzeichnet, dass** die Form der Augenstruktur (40) durch eine Summe von Zernike-Polynomen dargestellt wird.

5. Verfahren nach Anspruch 4, **dadurch gekennzeichnet, dass** die Koeffizienten der Verschiebungsfunktion (39) und die Koeffizienten der Zernike-Polynome durch Lösen einer einheitlichen Optimierungsaufgabe ermittelt werden.

6. Verfahren nach einem der Ansprüche 1 bis 5, **dadurch gekennzeichnet, dass** die Verschiebungsfunktion (39) eine Aneinanderreihung von Abschnittsfunktionen, wobei jede Abschnittsfunktion ein zeitabhängiges Polynom ist.

7. Verfahren nach Anspruch 6, **dadurch gekennzeichnet, dass** in jedem Chunk (35) Positionswerte (39) von der gesamten untersuchten Augenstruktur (40) enthalten sind.

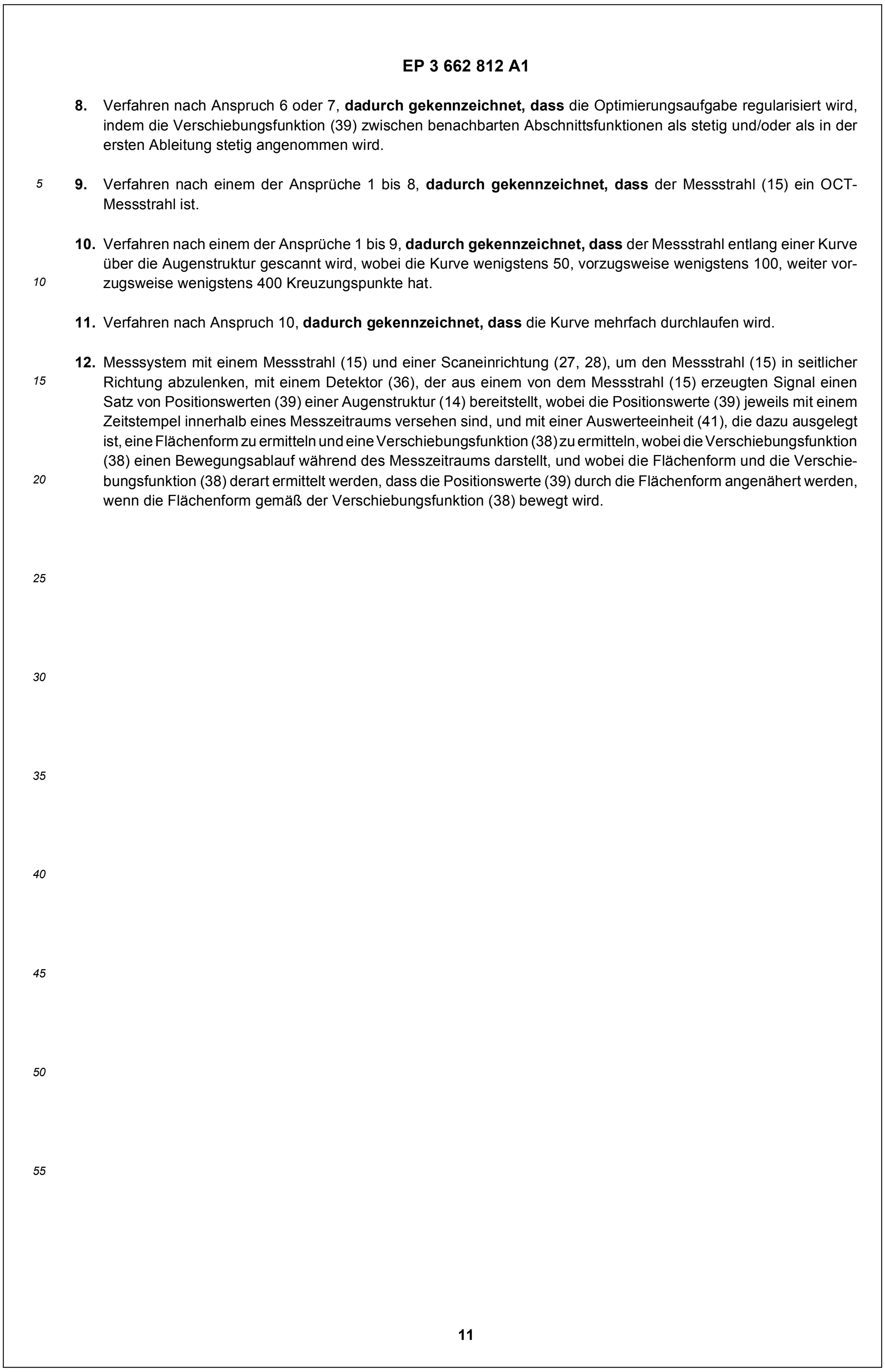

8. Verfahren nach Anspruch 6 oder 7, **dadurch gekennzeichnet, dass** die Optimierungsaufgabe regularisiert wird, indem die Verschiebungsfunktion (39) zwischen benachbarten Abschnittsfunktionen als stetig und/oder als in der ersten Ableitung stetig angenommen wird.

9. Verfahren nach einem der Ansprüche 1 bis 8, **dadurch gekennzeichnet, dass** der Messstrahl (15) ein OCT-Messstrahl ist.

10. Verfahren nach einem der Ansprüche 1 bis 9, **dadurch gekennzeichnet, dass** der Messstrahl entlang einer Kurve über die Augenstruktur gescannt wird, wobei die Kurve wenigstens 50, vorzugsweise wenigstens 100, weiter vorzugsweise wenigstens 400 Kreuzungspunkte hat.

11. Verfahren nach Anspruch 10, **dadurch gekennzeichnet, dass** die Kurve mehrfach durchlaufen wird.

12. Messsystem mit einem Messstrahl (15) und einer Scaneinrichtung (27, 28), um den Messstrahl (15) in seitlicher Richtung abzulenken, mit einem Detektor (36), der aus einem von dem Messstrahl (15) erzeugten Signal einen Satz von Positionswerten (39) einer Augenstruktur (14) bereitstellt, wobei die Positionswerte (39) jeweils mit einem Zeitstempel innerhalb eines Messzeitraums versehen sind, und mit einer Auswerteeinheit (41), die dazu ausgelegt ist, eine Flächenform zu ermitteln und eine Verschiebungsfunktion (38) zu ermitteln, wobei die Verschiebungsfunktion (38) einen Bewegungsablauf während des Messzeitraums darstellt, und wobei die Flächenform und die Verschiebungsfunktion (38) derart ermittelt werden, dass die Positionswerte (39) durch die Flächenform angenähert werden, wenn die Flächenform gemäß der Verschiebungsfunktion (38) bewegt wird.

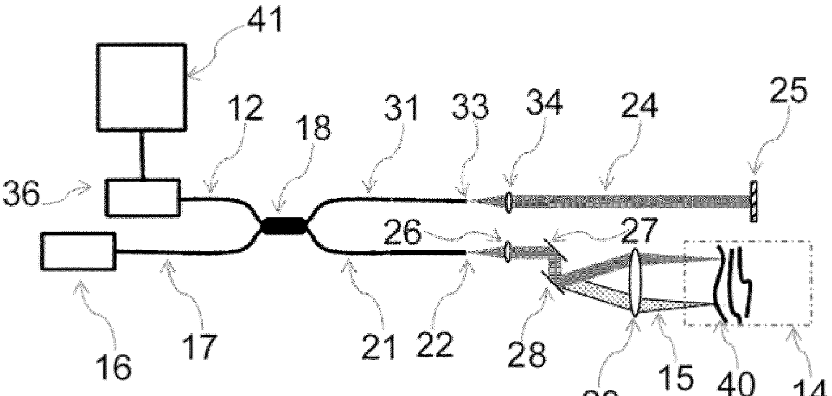

Fig. 1

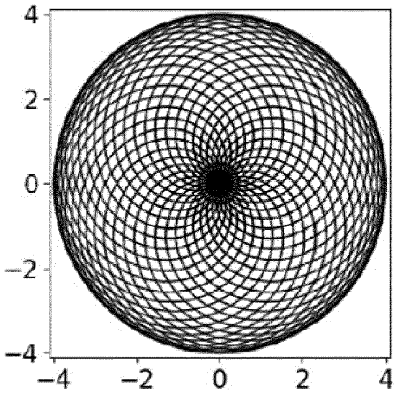

Fig. 2

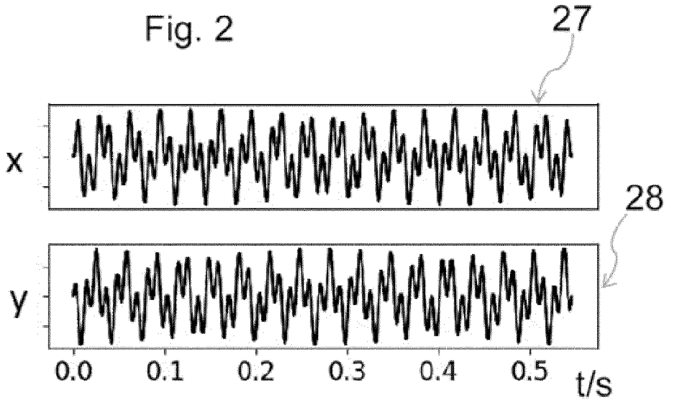

Fig. 3

EP 3 662 812 A1

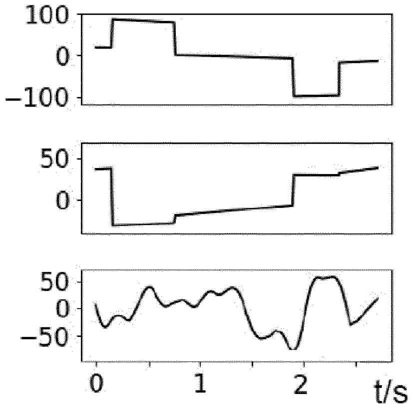

Fig. 4

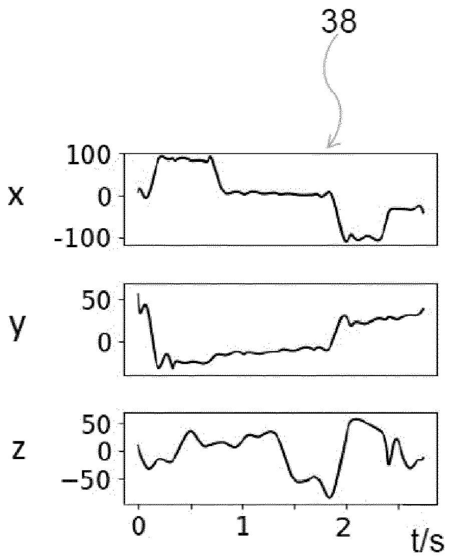

Fig. 5

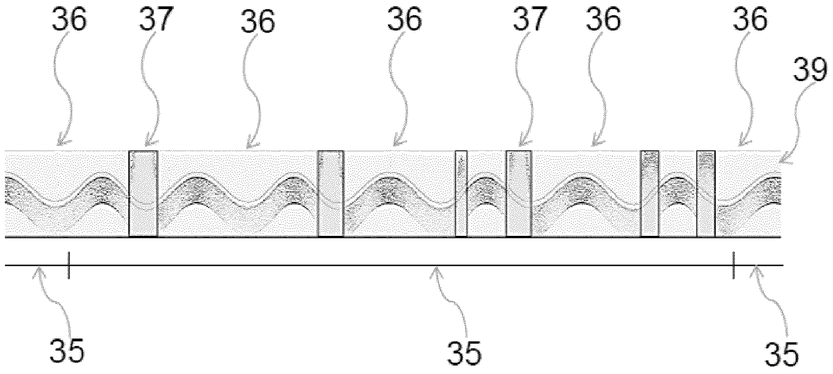

Fig. 6

13

Europäisches Patentamt
European Patent Office
Office européen des brevets

EUROPÄISCHER RECHERCHENBERICHT

Nummer der Anmeldung
EP 18 21 0058

EINSCHLÄGIGE DOKUMENTE

Kategorie	Kennzeichnung des Dokuments mit Angabe, soweit erforderlich, der maßgeblichen Teile	Betrifft Anspruch	KLASSIFIKATION DER ANMELDUNG (IPC)
X	HANSFORD C. HENDARGO ET AL: "Automated non-rigid registration and mosaicing for robust imaging of distinct retinal capillary beds using speckle variance optical coherence tomography", BIOMEDICAL OPTICS EXPRESS, Bd. 4, Nr. 6, 7. Mai 2013 (2013-05-07), Seite 803, XP055295793, United States ISSN: 2156-7085, DOI: 10.1364/BOE.4.000803 * Zusammenfassung; Abbildungen 1,2,7 * * Abschnitt 3.5; Seite 812 - Seite 813 * * Abschnitt 2; Seite 807 - Seite 808 * -----	1-12	INV. A61B3/102 G06T3/00
A	US 2018/192866 A1 (ABOU SHOUSHA MOHAMED [US] ET AL) 12. Juli 2018 (2018-07-12) * Zusammenfassung * * Absätze [0085] - [0088] * -----	1-12	
A	WO 2013/107649 A1 (ZEISS CARL MEDITEC AG [DE]) 25. Juli 2013 (2013-07-25) * das ganze Dokument * -----	1-12	RECHERCHIERTE SACHGEBIETE (IPC) A61B G06T
A,D	US 7 365 856 B2 (ZEISS CARL MEDITEC INC [US]) 29. April 2008 (2008-04-29) * das ganze Dokument * -----	1-12	

Der vorliegende Recherchenbericht wurde für alle Patentansprüche erstellt

3

Recherchenort	Abschlußdatum der Recherche	Prüfer
München	5. Juni 2019	Daniel, Christian

EPO FORM 1503 03.82 (P04C03)

KATEGORIE DER GENANNTEN DOKUMENTE

X : von besonderer Bedeutung allein betrachtet
Y : von besonderer Bedeutung in Verbindung mit einer anderen Veröffentlichung derselben Kategorie
A : technologischer Hintergrund
O : nichtschriftliche Offenbarung
P : Zwischenliteratur

T : der Erfindung zugrunde liegende Theorien oder Grundsätze
E : älteres Patentdokument, das jedoch erst am oder nach dem Anmeldedatum veröffentlicht worden ist
D : in der Anmeldung angeführtes Dokument
L : aus anderen Gründen angeführtes Dokument

& : Mitglied der gleichen Patentfamilie, übereinstimmendes Dokument

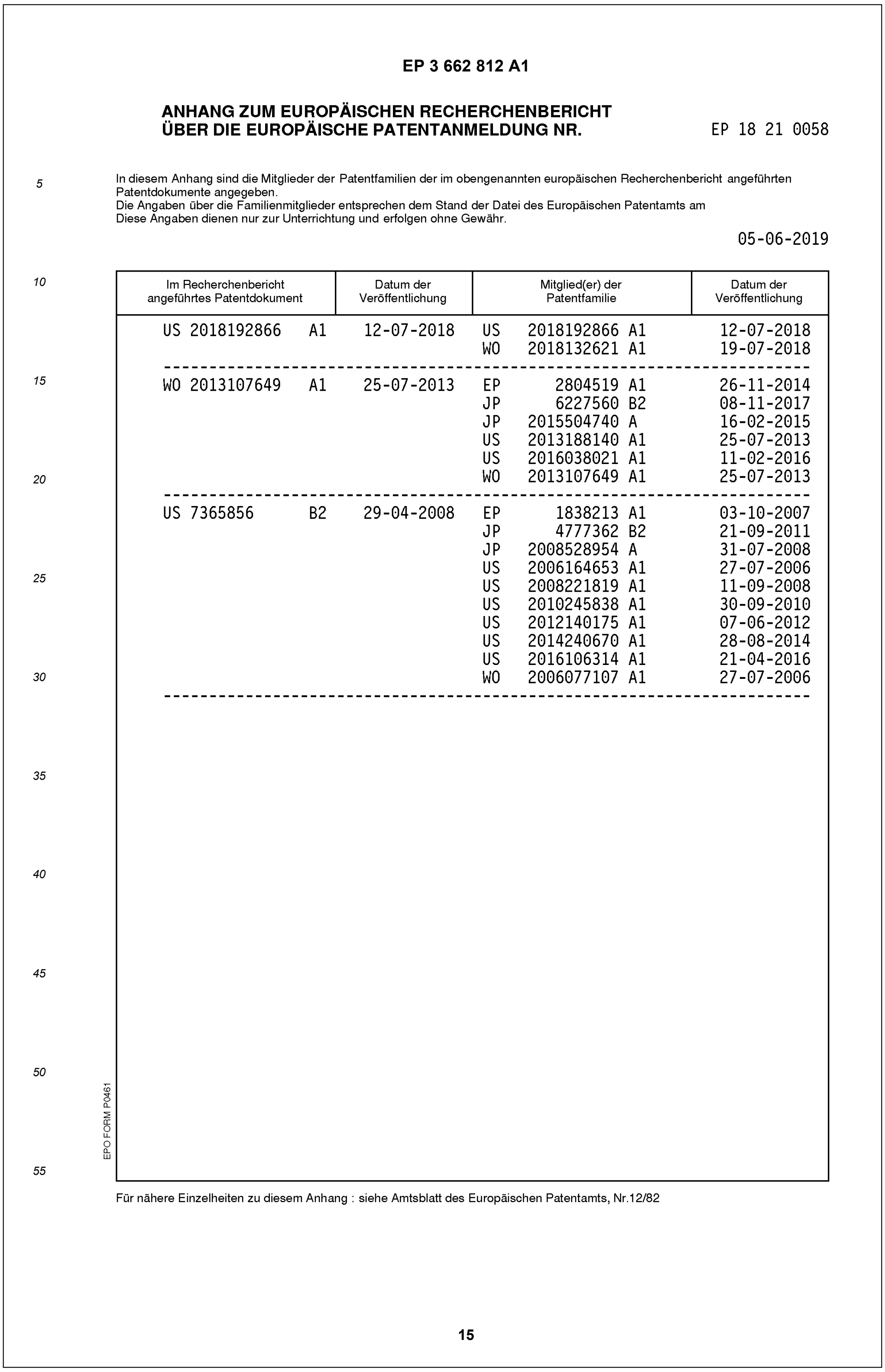

EP 3 662 812 A1

ANHANG ZUM EUROPÄISCHEN RECHERCHENBERICHT
ÜBER DIE EUROPÄISCHE PATENTANMELDUNG NR. EP 18 21 0058

In diesem Anhang sind die Mitglieder der Patentfamilien der im obengenannten europäischen Recherchenbericht angeführten Patentdokumente angegeben.
Die Angaben über die Familienmitglieder entsprechen dem Stand der Datei des Europäischen Patentamts am
Diese Angaben dienen nur zur Unterrichtung und erfolgen ohne Gewähr.

05-06-2019

Im Recherchenbericht angeführtes Patentdokument	Datum der Veröffentlichung	Mitglied(er) der Patentfamilie	Datum der Veröffentlichung
US 2018192866 A1	12-07-2018	US 2018192866 A1	12-07-2018
		WO 2018132621 A1	19-07-2018
WO 2013107649 A1	25-07-2013	EP 2804519 A1	26-11-2014
		JP 6227560 B2	08-11-2017
		JP 2015504740 A	16-02-2015
		US 2013188140 A1	25-07-2013
		US 2016038021 A1	11-02-2016
		WO 2013107649 A1	25-07-2013
US 7365856 B2	29-04-2008	EP 1838213 A1	03-10-2007
		JP 4777362 B2	21-09-2011
		JP 2008528954 A	31-07-2008
		US 2006164653 A1	27-07-2006
		US 2008221819 A1	11-09-2008
		US 2010245838 A1	30-09-2010
		US 2012140175 A1	07-06-2012
		US 2014240670 A1	28-08-2014
		US 2016106314 A1	21-04-2016
		WO 2006077107 A1	27-07-2006

EPO FORM P0461

Für nähere Einzelheiten zu diesem Anhang : siehe Amtsblatt des Europäischen Patentamts, Nr.12/82

15

IN DER BESCHREIBUNG AUFGEFÜHRTE DOKUMENTE

In der Beschreibung aufgeführte Patentdokumente

- US 7365856 B2 **[0003]**
- EP 2797493 A1 **[0003]**